Evolution of the Greenland Ice Sheet with the Global Climate as modelled with CESM2-CISM2

Muntjewerf, L.

Citation (APA)
Muntjewerf, L. (2021). *Evolution of the Greenland Ice Sheet with the Global Climate as modelled with CESM2-CISM2*. [Dissertation (TU Delft), Delft University of Technology]. https://doi.org/10.4233/uuid:34d6b261-5a55-45f6-8103-1d900cc98dc9

Important note
To cite this publication, please use the final published version (if applicable).
Please check the document version above.

Evolution of the Greenland Ice Sheet with the Global Climate as modelled with CESM2-CISM2

Laura Muntjewerf

Evolution of the Greenland Ice Sheet with the Global Climate as modelled with CESM2-CISM2

Evolutie van de Groenlandse ijskap met het mondiale klimaat zoals gemodelleerd door CESM2-CISM2

(met een samenvatting in het Nederlands)

PROEFSCHRIFT

ter verkrijging van de graad van doctor aan de Technische Universiteit Delft,
op gezag van de Rector Magnificus, prof.dr.ir. T.H.J.J. van der Hagen;
voorzitter van het College voor Promoties,

in het openbaar te verdedigen op
maandag 15 november 2021 om 12.30 uur

door

Laura MUNTJEWERF

Master of Science in Climate Studies
Wageningen University & Research, Nederland
geboren te Heemskerk, Nederland.

Dit proefschrift is goedgekeurd door de promotoren.

Samenstelling promotiecommissie:

Rector Magnificus,	voorzitter
Prof.dr.-Ing.habil. R. Klees	Delft University of Technology, promotor
Dr. M. Vizcaino	Delft University of Technology, copromotor

Onafhankelijke leden:

Prof.dr.ir. B.J.H van de Wiel	Delft University of Technology
Prof.dr. M.R. van den Broeke	Utrecht University (NL)
Prof.dr. J. Gregory	University of Reading (UK)
Dr. L. Gregoire	University of Leeds (UK)
Dr. H. Goelzer	Norce Research (NO)
Prof.dr. A.P. Siebesma	Delft University of Technology (reserve)

Opgemaakt door de auteur met het LaTeX Documentation System.

Een elektronische versie van dit proefschrift is beschikbaar via:
`https://repository.tudelft.nl`

Contents

Summary

Human-induced climate change is one of the challenges of our time. The increasing global mean temperature, shifts in precipitation patterns, and the rising sea level threaten ecosystems and natural resources, and pose a great risk on society at large. Policymakers need information about the expected impacts, as accurate as possible, in order to make adequate climate change mitigation and adaptation policies.

The Greenland Ice Sheet (GrIS) appears to be sensitive to the changing climate. At present, the GrIS is losing mass at an accelerated pace. This is the focus of this thesis. The key terms of the GrIS mass balance are (1) the Surface Mass Balance (SMB) and (2) the ice discharge at glacier fronts. At the surface, the ice sheet gains mass through precipitation and loses mass through meltwater runoff and through sublimation. Ice discharge is a loss term regulated by ice flow. When the mass balance is negative, the ice sheet loses mass contributing to sea level rise.

The GrIS, however, is not an isolated environment. It is an integral part of the Earth system. Interactions and feedback mechanisms between the ice sheet and various parts of the Earth's system affect the ice sheet's mass loss. The future behavior of the GrIS is a major source of uncertainty in the projections of 21st century sea level rise. The basis for this lies, among other things, in an incomplete understanding of the interactions between the ice sheets and other components the Earth system.

The aim of this dissertation is to gain advanced understanding on the interactions and feedbacks between the Greenland Ice Sheet ice flow, the SMB, and the Earth system on the multidecadal and multicentennial time scale. This understanding is obtained by addressing the following research questions:

1. What model developments are necessary to integrate the main interactions and feedback mechanisms between the Greenland Ice Sheet and the Earth system in a model that simulates Earth system dynamics?

2. Which processes are captured through the new ice sheet/climate model coupling?

3. What estimates for 21st century Greenland Ice Sheet mass loss does the coupled model provide for the SSP5-8.5 scenario?

4. How does the Greenland Ice Sheet respond as an integral part of the Earth system to elevated atmospheric CO_2 on a multicentennial timescale?

The modelling tools used in this thesis are the Community Earth System Model version 2 (CESM2) and the Community Ice Sheet Model version 2 (CISM2). CESM2 is

a state-of-the-art Earth System Model which consists of atmosphere, land, ocean, sea ice, and ice sheet models and allows for realistic simulations of the Earth's climate. CISM2 is a three-dimensional thermo-mechanically coupled ice sheet model that uses a higher-order approximation of the Stokes equations to calculate ice velocities and internal temperatures of the dynamically evolving Greenland Ice Sheet.

To improve the representation of processes that take place between the ice sheet and the other components of the Earth system in CESM2, CISM2 is integrated into CESM2. The integration consists of bi-directional coupling of the ice sheet model to the land and atmosphere models, and one-directional coupling to the ocean model. The SMB is calculated in the land model using a physics-based energy balance scheme. The SMB is then downscaled to the ice-sheet model using an 'elevation class'-method. Ice sheet meltwater and solid ice discharge are passed to the ocean model. The geometry of the ice sheet is passed to the atmosphere model. The advance and retreat of ice sheet margins are communicated to the land model. As such, CESM2–CISM2 includes an advanced representation of surface snow and ice processes, and the model can be used to study the response of ice sheets to Earth system changes, and vice versa.

To estimate 21st century Greenland Ice Sheet mass loss, CESM2–CISM2 is forced with atmospheric greenhouse gas concentrations for the period 1850–2014. Next, the model is forced for the rest of the 21st century following the SSP5-8.5 scenario. The results show that by 2050, the total Greenland Ice Sheet mass loss is equivalent to 23 mm of global mean sea level rise. All drainage basins of the Greenland Ice Sheet lose mass during the second half of the 21st century because of increased surface melting and runoff. The relative contribution of the northern basins to the total mass loss increases also at this time. By 2100, the simulation shows a 5.4 K global mean temperature increase and a strong North Atlantic Meridional Overturning Circulation (NAMOC) weakening compared to the pre-industrial mean climate. The projected Greenland Ice Sheet contribution to sea level rise at the end of the century is 109 mm.

The multicentury Greenland Ice Sheet response to elevated CO_2 levels is explored by forcing the CESM2–CISM2 with an idealized scenario. In this simulation, it is found that the Greenland Ice Sheet responds nonlinearly to climate warming. The response starts slow, with an SMB decline fueled by increased longwave radiation from the elevated CO_2 in the atmosphere. Melt and overall mass loss start accelerating after more than 100 years of increasing CO_2. At this time, the ablation areas have expanded enough to trigger widespread impact of the ice-albedo feedback, and the net shortwave radiation at the surface increases. The summer sensible heat flux amplifies the melt due to a larger temperature gradient between the surface and the ambient air. Additionally, the latent heat flux contributes via deposition to the melt energy in the ablation zones. As a whole, the accelerated GrIS mass loss is caused by rapidly increasing surface mass loss. This is compensated by a reduction in ice discharge, as the GrIS margins thin and retreat. The southwest drainage basin provides the largest basin contribution to the Greenland Ice Sheet mass loss. The relative contribution of the northern basins to the total Greenland Ice Sheet mass loss increases throughout the simulation.

This dissertation as a whole incorporates several steps towards a better understanding of interactions and feedback mechanisms between the Greenland ice sheet and the Earth system under elevated greenhouse gas levels on the multidecadal and multicentennial time scales. It includes the model description and demonstration of the coupled Earth system model CESM2 with interactive Greenland ice sheet dynamics simulated by CISM2. Further, it features the first production simulations that are made with the coupled model and their analysis, like a 21$^{\text{st}}$ century SSP5-8.5 scenario projection of Greenland Ice Sheet mass loss.

Samenvatting

De door de mens veroorzaakte klimaatverandering is één van de uitdagingen van onze tijd. Naast een bedreiging voor ecosystemen en natuurlijke hulpbronnen vormen de stijgende temperatuur, verschuivingen in neerslagpatronen en de stijgende zeespiegel een groot risico voor de samenleving als geheel. Beleidsmakers hebben behoefte aan zo nauwkeurig mogelijke informatie over de verwachte effecten om adequaat beleid voor klimaatmitigatie en -adaptatie te maken.

De Groenlandse ijskap (GrIS) blijkt gevoelig te zijn voor het veranderende klimaat. De GrIS verliest massa in versneld tempo. Zij levert daarmee een belangrijke bijdrage aan de zeespiegelstijging. Dit is de focus van dit proefschrift. De belangrijkste termen van de massabalans van de GrIS zijn (1) de oppervlaktemassabalans en (2) de afkalving van brokken ijs aan het front van gletsjers. Aan het oppervlak verkrijgt de ijskap massa door neerslag, en verliest ze massa via afvloeiing van smeltwater en via sublimatie. Afkalving is een verliesterm die wordt gereguleerd door ijsstroming. Wanneer de massabalans negatief is, verliest de ijskap massa. Dit draagt bij aan zeespiegelstijging.

De GrIS staat echter niet op zichzelf, maar is een integraal onderdeel van het aardsysteem. Interacties en wisselwerkingen tussen de ijskap en verschillende onderdelen van het aardsysteem beïnvloeden het massaverlies van de ijskap. Het toekomstige gedrag van de GrIS is een grote bron van onzekerheid in de projecties van zeespiegelstijging voor de 21$^\text{e}$ eeuw. De grondslag hiervan ligt onder andere in een onvolledig begrip van de wisselwerkingen tussen de ijskappen en het aardsysteem.

Het doel van dit proefschrift is om nieuwe inzichten te verwerven in de wisselwerking tussen ijsstroming, de oppervlaktemassabalans van de ijskap en het mondiale aardsysteem op de tijdschaal van tientallen tot honderden jaren. Deze inzichten worden verkregen door het beantwoorden van de volgende onderzoeksvragen:

1. Welke modelontwikkelingen zijn nodig om de belangrijkste interacties en terugkoppelingsmechanismen tussen de Groenlandse ijskap en het aardsysteem te integreren in een model dat de dynamiek van het aardsysteem simuleert?

2. Welke processen worden vastgelegd door het nieuw gekoppelde ijskap-klimaatmodel?

3. Welke schattingen voor 21$^\text{e}$-eeuwse massaverlies van de Groenlandse ijskap levert het gekoppelde model voor het SSP5-8.5-scenario?

4. Hoe reageert de Groenlandse ijskap als integraal onderdeel van het aardsys-

teem op verhoogde atmosferische CO_2 op een tijdschaal van honderden jaren?

De gebruikte gereedschappen zijn het Community Earth System Model versie 2 (CESM2) en het Community Ice Sheet Model versie 2 (CISM2). CESM2 is een state-of-the-art aardsysteemmodel dat bestaat uit atmosfeer-, land-, oceaan-, zeeijs- en ijskapmodellen. Met dit model zijn realistische simulaties van het klimaat op aarde mogelijk. CISM2 is een driedimensionaal thermo-mechanisch gekoppeld ijskapmodel dat een hogere-orde benadering van de Stokes-vergelijkingen gebruikt om ijsstroming en interne temperaturen van dynamisch evoluerende ijskappen te berekenen.

Om de weergave in CESM2 te verbeteren van processen die plaatsvinden tussen de ijskap en het aardsysteem, is CISM2 geïntegreerd in CESM2. De integratie bestaat uit een tweerichtingskoppeling van het ijskapmodel met de land- en atmosfeermodellen en een eenrichtingskoppeling met het oceaanmodel. De oppervlaktemassabalans wordt berekend in het landmodel met behulp van een op fysica gebaseerd energiebalansschema. Daarna wordt de oppervlaktemassabalans met behulp van een 'elevation class'-methode teruggeschaald naar het ijskapmodel. Smeltwater van de ijskap en afkalvende stukken ijs worden doorgegeven aan het oceaanmodel. De geometrie van de ijskap wordt doorgegeven aan het atmosfeermodel. Het vooruitschuiven en het terugtrekken van ijskapranden wordt doorgegeven aan het landmodel. Als zodanig bevat CESM2-CISM2 een geavanceerde weergave van sneeuw- en ijsprocessen en kan het worden gebruikt om de reactie van ijskappen op veranderingen in het aardsysteem, en vice versa, te bestuderen.

Om het massaverlies van de GrIS in de 21^e eeuw in te schatten, wordt het CESM2-CISM2 model gevoed met historische atmosferische broeikasgasconcentraties voor de periode 1850-2014. Vervolgens krijgt het model broeikasgasconcentraties voor de rest van de 21^e eeuw volgens het SSP5-8.5-scenario. De resultaten laten zien dat de GrIS tot aan 2050 een totale massa verliest die gelijk is aan 23 mm stijging van de wereldwijde gemiddelde zeespiegel. Tijdens de tweede helft van de 21^e eeuw is er massaverlies in alle afwateringsbekkens van de GrIS vanwege een toename in de hoeveelheid smeltwater. Ook neemt dan de relatieve bijdrage toe van de noordelijke bekkens aan het totale massaverlies. Tegen 2100 toont de simulatie een wereldwijde gemiddelde temperatuurstijging van 5.4 K en een sterke verzwakking van de Noord-Atlantische tak van de oceaancirculatie (NAMOC) in vergelijking met het pre-industriële klimaat. De totale verwachte GrIS-bijdrage aan de zeespiegelstijging aan het einde van de eeuw is 109 mm.

De reactie van de GrIS op verhoogde CO_2-niveaus op de tijdschaal van honderden jaren wordt onderzocht door het CESM2-CISM2 model een geïdealiseerd scenario te geven. In deze simulatie blijkt dat de GrIS niet-lineair reageert op klimaatopwarming. De respons begint langzaam, met een toename van oppervlaktesmelt door toegenomen langgolvige thermische straling vanwege de verhoogde CO_2 in de atmosfeer. Afvloeiing van smeltwater en algeheel massaverlies beginnen te versnellen na meer dan 100 jaar CO_2-verhoging. Het gebied met een negatieve oppervlaktebalans, waar donker glaciaal ijs blootligt, is dan voldoende uitgebreid om een wijdverbreide impact van de ijs-albedo-feedback teweeg te brengen, waardoor de netto kortegolfstraling aan het oppervlak toeneemt. De zomerse voelbare warmtestroom

versterkt de GrIS-smelt vanwege een grotere temperatuurgradiënt tussen het ijs en de omgevingslucht. Bovendien draagt de latente warmtestroom via depositie bij aan de smeltenergie in de smeltende zones. Als geheel wordt de versnelling in GrIS-massaverlies veroorzaakt door een snel toenemend massaverlies aan het oppervlak. Dit wordt gecompenseerd door een vermindering in afkalving; de GrIS marges worden dunner en trekken terug landinwaarts. De zuidwestelijke afwateringsbekken levert de grootste bijdrage aan het GrIS-massaverlies, maar de relatieve bijdrage van de noordelijke bekkens aan het totale GrIS-massaverlies neemt toe in de loop van de simulatie.

Als geheel bevat dit proefschrift verschillende stappen die leiden tot een beter begrip van interacties en feedbackmechanismen tussen de GrIS en het aardsysteem onder verhoogde broeikasgasniveaus op de tijdschaal van tientallen tot honderden jaren. Het omvat de modelbeschrijving en demonstratie van het gekoppelde aardsysteemmodel CESM2 met interactieve GrIS-dynamica gesimuleerd door CISM2. Verder bevat het de eerste productiesimulaties die zijn gemaakt met het gekoppelde model en hun analyse, zoals een 21e-eeuwse SSP5-8.5-scenarioprojectie van GrIS-massaverlies.

List of abbreviations

AA	Arctic Amplification
AIS	Antarctic Ice Sheet
AMO	Atlantic Multidecadal Oscillation
ANN	Annual
AOGCM	Atmosphere-Ocean General Circulation Model
AOGCM-ISM	Atmosphere-Ocean General Circulation Model - Ice Sheet Model
AR5	Fifth Assessment Report
BMB	Basal Mass Balance
CAM6	Community Atmosphere Model version 6
CESM2	Community Earth System Model version 2
CICE5	Los Alamos National Laboratory sea ice model version 5
CISM2	Community Ice Sheet Model version 2
CLM5	Community Land Model version 5
CLUBB	Cloud Layers Unified by Binormals
CMIP6	Coupled Model Intercomparison Project phase 6
DEM	Digital Elevation Model
DJF	December - January - February
EC	Elevation Class
ELA	Equilibrium Line Altitude
ELRA	Elastic Lithosphere Relaxing Asthenosphere
E_M	melt energy
EMIC	ESM of Intermediate Complexity
ESM	Earth System Model
GBI	Greenland Blocking Index
GCM	General Circulation Model
GHF	ground heat flux
GICs	glaciers and ice caps
GRACE	Gravity Recovery and Climate Experiment
GrIS	Greenland Ice Sheet
ID	Ice Discharge
IPCC	Intergovernmental Panel on Climate Change
ISM	Ice Sheet Model
ISMIP6	Ice Sheet Model Intercomparison Project for CMIP6
JJA	June - July - August
LGM	Last Glacial Maximum
LHF	latent heat flux

LIWG	Land Ice Working Group
LW$_{net}$	net longwave radiation
LWCF	Longwave Cloud Forcing
LWP	liquid water path
MB	Mass Balance
MG2	two-moment cloud microphysics scheme
MOM6	Modular Ocean Model version 6
MOSART	Model for Scale Adaptive River Transport
NAMOC	North Atlantic Meridional Overturning Circulation
NAO	North Atlantic Oscillation
NCAR	National Center for Atmospheric Research
PDD	positive degree-day
PHIS	surface geopotential
PI	pre-industrial
PFT	Plant Functional Type
POP2	Parallel Ocean Program version 2
RCP	Representative Concentration Pathway
SEB	Surface Energy Balance
SHF	sensible heat flux
SGH	standard deviation of large subgrid-scale topography
SGH30	standard deviation of small subgrid-scale topography
SIA	Shallow Ice Approximation
SLE	sea level equivalent
SLR	sea level rise
SMB	Surface Mass Balance
SNICAR	Snow, Ice, and Aerosol Radiation model
SSA	Shallow Shelf approximation
SSP	Shared Socio-economic Pathway
SW$_{net}$	net shortwave radiation
SWCF	Shortwave Cloud Forcing (SWCF)
TCRF	Total Cloud Radiative Forcing
TOA	top of the atmosphere
USGS	United States Geological Survey
WE	water equivalent

Chapter 1

Introduction

De zachte krachten zullen zeker winnen

Henriëtte Roland Holst *Verzonken grenzen*

1.1   Contemporary climate change and sea level rise commitment

Anthropogenic climate change is one of the challenges of our age. Not only threatening ecosystems and the quality of natural resources, global warming and sea level rise may trigger human climate migration, due to increased flood risk of storm surges and increased costs of protective infrastructure (Curtis and Schneider, 2011; Hauer et al., 2016). It is potentially disruptive to many of our current social and economic structures, given that much of the world's population and economic capital resides in coastal areas (Neumann et al., 2015; Nicholls et al., 2011).

Global sea level rise is a combination of ocean volumetric change (thermal expansion) and ocean mass change (more water)(Gregory et al., 2019). Additionally, land subsidence contributes to the sea level budget. Sea level responds with a time lag to an increase in the global mean temperature, as it takes time for the deeper ocean waters to warm, and it takes time for glacial ice to melt. A metric that includes both near-term and long-term effects is the so-called *sea level commitment*: how much sea level change is anticipated up to and after the atmospheric state has reached an equilibrium. The Intergovernmental Panel on Climate Change (IPCC) special report on the impacts of global warming of 1.5°C above pre-industrial (a.k.a., year 1850) states that human-induced global warming has reached approximately +1°C above pre-industrial in 2017 (Masson-Delmotte et al., 2018). This commits the Earth to a sea level rise of 2.3 meter that will take place in the next 2,000 years, according to a study by Levermann et al. (2013). The same IPCC special report estimates that in 2040 the global temperature increase will reach +1.5°C above pre-industrial levels if emissions continue at the current rate. This will have a subsequent impact on the sea level rise. Clark et al. (2016) estimate the global mean sea level to have risen with 0.9 m by the year 2300 and 2 m by the year 3000 in the case that the targets of the Paris Agreement (i.e., to keep the global average temperature rise well below +2°C in the 21st century) are met, and argue that sea level commitment is a useful way to judge climate policy targets.

1.2   The Greenland Ice Sheet

The Greenland Ice Sheet (GrIS) is the focus of this dissertation. The GrIS appears to be very sensitive to the changing climate. Observations from the satellite mission Gravity Recovery and Climate Experiment (GRACE) over the period 2002-2020 show that the GrIS lost on average 0.72 mm of sea level equivalent (SLE) per year (see Figure 1.1). About half or more of the present-day mass loss rate is attributed to surface mass losses (e.g., meltwater runoff), and the other main part to dynamical losses (e.g., ice discharge, calving) (Van den Broeke et al., 2016; Shepherd et al., 2019; Choi et al., 2021).

The GrIS is the largest freshwater reservoir in the Northern Hemisphere, storing around 7.4 m potential global mean sea level rise (SLR) (Bamber et al., 2013;

Morlighem et al., 2017). Located east of the Canadian Archipelago, the GrIS surrounded by the Arctic Ocean and the North Atlantic Ocean. The ice thickness is more than 3000 m at its thickest point. Present-day annual mean skin temperatures range between -30.5 to -3.5°C, with daily winter temperatures in the high interior that can reach -70°C (Ettema et al., 2010).

The GrIS gains mass from precipitation. The natural variability in the precipitation patterns of the GrIS is strongly influenced by synoptic scale processes (Fyke et al., 2018). Cyclone activity in the North Atlantic has a strong impact on its seasonality. Tropical cyclones that deflect off the East coast of North America typically follow a mean trajectory across the North Atlantic towards Europe. In the winter, the trajectory of some cyclones bends off to the north such that they hit land on the south and southeast of Greenland. In combination with the steep orographic gradients in this region, this results in a band of high-precipitation along the southeast coast that is characteristic of the GrIS winter precipitation pattern. In the summer, more precipitation falls on the west flank of the GrIS and further in the interior. GrIS precipitation variability has furthermore been linked to the phase of the North Atlantic Oscillation (NAO)(Bromwich et al., 1999; Wong et al., 2015) that is an index of the pressure difference between the Iceland low and the Azores high, with the phase of the Atlantic Multidecadal Oscillation (AMO) (Mernild et al., 2015; Lewis et al., 2017) and with the Greenland Blocking Index (GBI) (Hanna et al., 2016; Auger et al., 2017).
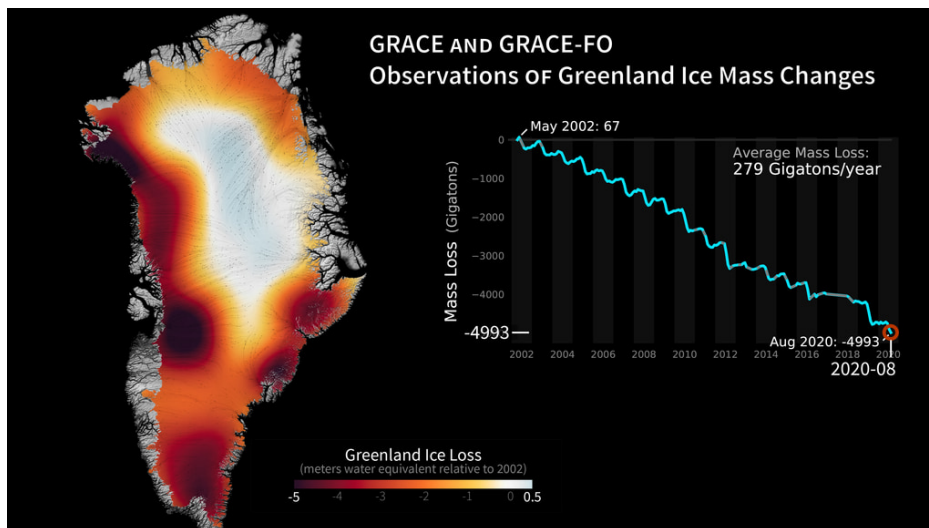
Figure 1.1: Greenland Ice Sheet mass Loss as measured by the GRACE satellites (2002-2017) and GRACE Follow-On (since 2018 -). Orange and red shades indicate areas that lost ice mass, while light blue shades indicate areas that gained ice mass (meter water equivalent). White indicates areas where there has been very little or no change in ice mass since 2002. Grey lines are average flow lines created from satellite radar interferometry. Figure credits: F.W. Landerer and M.Jentoft-Nilsen, NASA/JPL Caltech, published March 2021; https://svs.gsfc.nasa.gov/31156.

1.3   Ice sheet behaviour on geological time scales

An ice sheet is a continental-size mass of glacial ice that originated from compacted snow (Cuffey and Paterson, 2010). Glacial ice flows under the force of gravity. The ice deforms like a viscous fluid, with the ice viscosity nonlinearly dependent on temperature. The base of a continental ice sheet can be either frozen at the bedrock, or thawed due to frictional or geothermal heat release. The basal meltwater that is produced in the latter case promotes sliding locally (ice streams). At calving fronts, frozen mass is lost through iceberg calving (ice discharge). In the Surface Mass Balance (SMB), the ice sheet gains mass from precipitation, and loses mass via runoff and sublimation. The equilibrium line altitude separates the ice sheet surface into the accumulation zone (SMB > 0) and the ablation zone (SMB < 0). The Mass Balance (MB) of an ice sheet is the sum of the SMB and the Basal Mass Balance (BMB), minus Ice Discharge (ID):

$$MB = SMB + BMB - ID \tag{1.1}$$

When the mass balance is negative, the ice sheet loses mass which contributes to sea level rise.

The Earth has seen many cycles of ice sheet advance and retreat, and sea level has fallen and risen accordingly. The periodicity of ice ages has been linked to what is known as the Milankovic cycles, that describe the cyclical behaviour of changes in the solar forcing due to the Earth's orbital changes and changes in the Earth's axis tilt. For the last 800 kyr, ice ages have alternated with interglacial periods with a periodicity of 100 kyr. Drilling ice cores from the present-day ice sheets and analyzing the air that has been preserved in bubbles provides accurate information on the atmospheric CO_2 concentration and temperature (from deuterium) (e.g., Augustin et al. (2004); Dahl-Jensen et al. (2013), see top panel of Figure 1.2). Deep ocean temperatures can be inferred from the ratio of oxygen isotopes ($\delta^{18}O$ ratio) in ocean sediment records (Zachos et al., 2001), and used to estimate the global mean surface temperature change (see middle panel of Figure 1.2). The evolution of the sea level can be reconstructed by combining different paleo-records with ice sheet models (e.g., Bintanja et al. (2005), see bottom panel of Figure 1.2). On glacial timescales, a linear relation can be seen between global mean temperature and the global mean sea level of about 20 meter sea level change for each 1 K temperature change.

The current interglacial, the Holocene, started about 11,600 years ago. In the previous ice age, the Last Glacial Maximum (LGM) 26-18 kyr ago, an area about three times as large as today was covered by land ice. This included large parts of North America, Great Britain, Fenno-Scandinavia, Siberia and Patagonia (Abe-Ouchi et al., 2015; Braconnot et al., 2007). The global mean temperature was about 5 K lower in the LGM, and the global mean sea level about 120 m lower. The Industrial Revolution halfway in the 19$^{\text{st}}$ century has marked the time from which human activities started to have a significant impact on the planet. The increasing use of fossil fuels to accommodate society's needs results in a present-day rate of carbon emis-
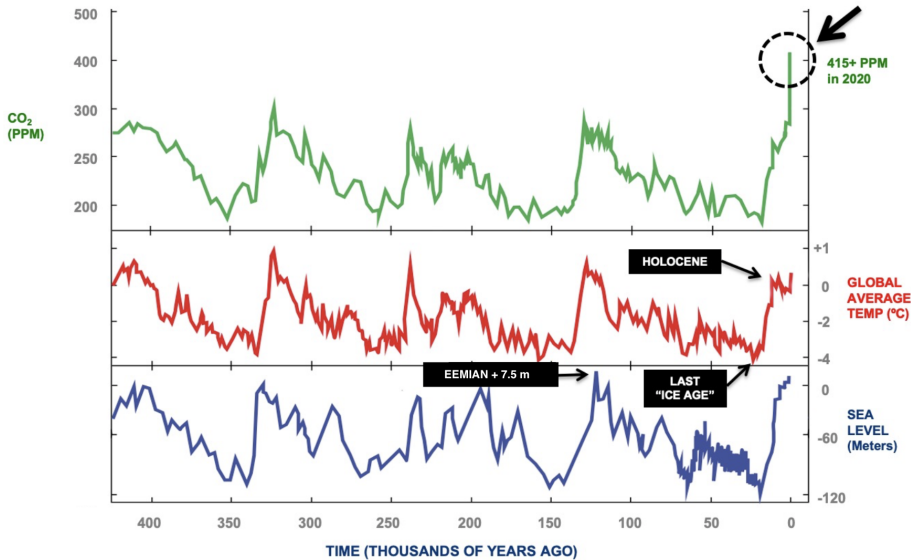
Figure 1.2: Carbon dioxide, temperature, and sea level. Figure credits: John Englander, adapted from Hansen and Sato (2012) with atmospheric carbon dioxide data from Lüthi et al. (2008) and sea level reconstruction data from Bintanja et al. (2005).

sions that is unprecedented in the past 66 million years (Zeebe et al., 2016). Some scholars suggest to refer to this time as the Anthropocene (Crutzen, 2006).

The present-day fossil fuel emissions impose a perturbation to the Earth's energy balance, with increasing levels of atmospheric greenhouse gasses (among which CO_2, see Figure 1.2). When looking at 21st century projections of global mean sea level rise and temperature increase (approximately 1 m and 1.5–4 K, respectively), this is well outside of the above-mentioned paleo-empirical ratio of about 20 meter sea level change for each 1 K temperature change. This relates to the sea-level commitment discussed earlier, and to the fact that different components of the Earth system have different response times to reach a new equilibrium. The relation between CO_2, the global mean temperature and sea level is non-linear on the centennial and decadal time scales. More understanding is needed about processes that govern ice sheet mass loss on these timescales.

1.4 Multidecadal and centennial timescale feedback mechanisms

Multiple processes govern ice sheet mass loss. These include ice sheet dynamical behaviour, interactions with the Earth system, and ice sheet-Earth system feedback mechanisms. Feedback mechanism in this sense of the word, and as used in this dissertation, is a term that is commonly thought to find its origin in electrical circuit

engineering to describe the system's response to a single perturbation. A positive feedback is a mechanism amplifying the initial effect, a negative feedback is a mechanism neutralizing the initial effect. Figure 1.3 provides an overview of the known interactions and feedback mechanisms related to ice sheets in the Earth system. Below we describe the main feedback mechanisms that are important to the Greenland Ice Sheet on the timescales of our interest, which is the decadal and centennial time scale.
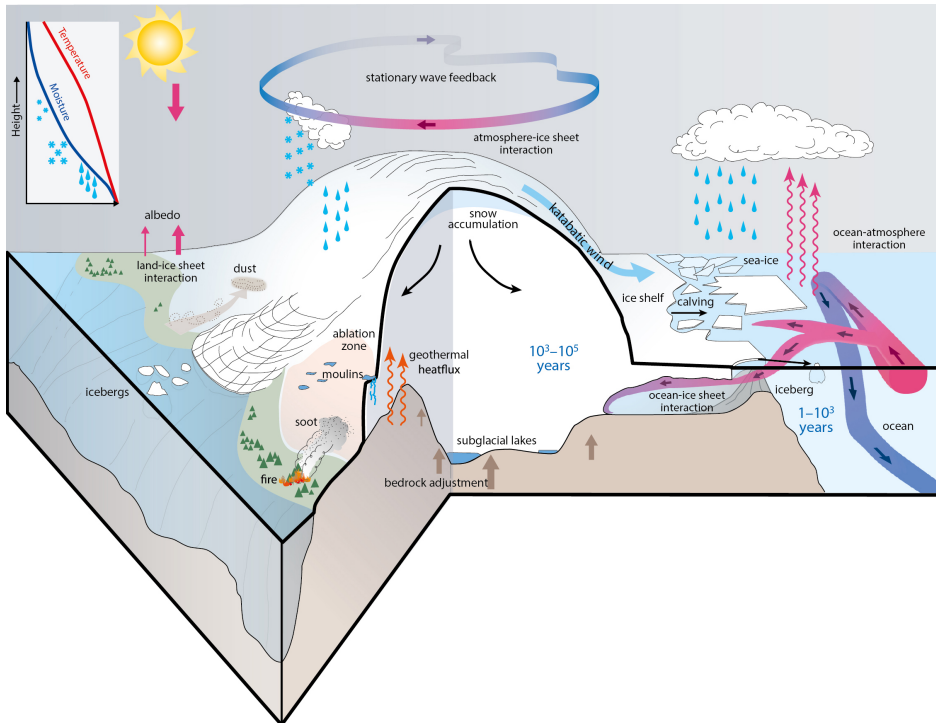
Figure 1.3: The interaction of ice sheets with the climate system on time scales of months to millions of years. Figure credits: WG I, Fig. 1 in Box 5.2, IPCC AR5, Church et al. (2013).

The SMB-elevation feedback (Oerlemans, 1981; Edwards et al., 2014a,b) is a positive feedback mechanism. In principle this is dictated by interactions between the ice sheet surface and the atmosphere. As the ice sheet gains mass (MB > 0), its elevation will increase. It is colder at higher altitudes, which preserved ice sheet mass. Vice versa, temperatures are higher at lower elevations. This promotes melt, and further ablation. A second aspect of the SMB-elevation feedback is the change in precipitation. The change in ice sheet elevation affects the atmospheric circulation and the location where the precipitation falls. Furthermore, the amount and type of the precipitation is affected via the temperature lapse rate.

The geometry-SMB feedback (Oerlemans, 1981) is a negative, stabilizing feedback mechanism. Ice flow can be formulated as the vertically integrated continuity equation for ice thickness (Equation 1.2, e.g., Huybrechts (1992); Van Den Berg et al.

(2006)):

$$\frac{\partial H}{\partial t} = -\nabla \cdot (H\mathbf{U}) + MB \tag{1.2}$$

with H the ice thickness, $\mathbf{U}$ the depth-averaged horizontal velocity vector, and MB the mass balance. Equation 1.2 states that the horizontal ice mass flux $H\mathbf{U}$ depends on the ice thickness, the surface gradient, and the mass balance. It follows that when the ice sheet gains mass from a positive SMB, the ice sheet advances down-slope. This leads to an increase in the width of the ablation area and an increase in the total surface mass loss, which in turn, dampens the initial mass gain. The other way around, when the ice sheet retreats, the ablation area decreases.

The ice-albedo feedback (Box et al., 2012) is a positive feedback mechanism. It relates a change in the surface reflectivity to changes in melt. Snow that is melting has a higher liquid water content than dry snow. The melt decreases albedo, which leads to more melting. Exposed bare ice has an even lower albedo. Vegetation processes as the ice sheet retreats may also add to the ice-albedo feedback (Stone and Lunt, 2013).

The coupling between the SMB and ice discharge (Lipscomb et al., 2013; Goelzer et al., 2013) is a negative feedback mechanism related to ice flow. When the ice sheet loses mass, the ice thins. Subsequent flow velocities decrease such that even less ice discharge happens at the outlet glaciers.

1.5 Open science questions about climate change and Greenland Ice Sheet mass loss

There are a number of pressing questions that arise on the intersection between climate dynamics and ice sheet dynamics with regard to the Greenland Ice Sheet. Below the main questions are discussed:

1. **How much can we expect the GrIS to contribute to global mean sea level rise the coming century, and how can uncertainty in SLR projections be decreased?**
   Ice sheet models and climate models are important scientific tools to estimate the future GrIS contribution to sea level rise. Following the IPCC's Fifth Assessment Report (AR5)(Church et al., 2013), the global mean sea level is projected to rise with 0.05 to 0.27 meter by 2100 due to GrIS mass loss, depending on the future scenario of greenhouse gas emissions (Figure 1.4). The projections of 21st century GrIS mass loss show a large uncertainty range (e.g., Bamber et al. (2019); van de Wal et al. (2019)). One source of uncertainty is in the future emission scenarios, dependent on how the world economy and population will evolve (O'Neill et al., 2016). A second source of uncertainty comes from differences among ice sheet models (Goelzer et al., 2018). A third source of uncertainty is due to an incomplete understanding of the complex interactions

and feedbacks between the ice sheets and the Earth system (e.g., Benn et al.
(2017); Moon et al. (2018)). For example, it is unclear how the partitioning
between surface mass loss and dynamical loss will evolve in a warming climate.
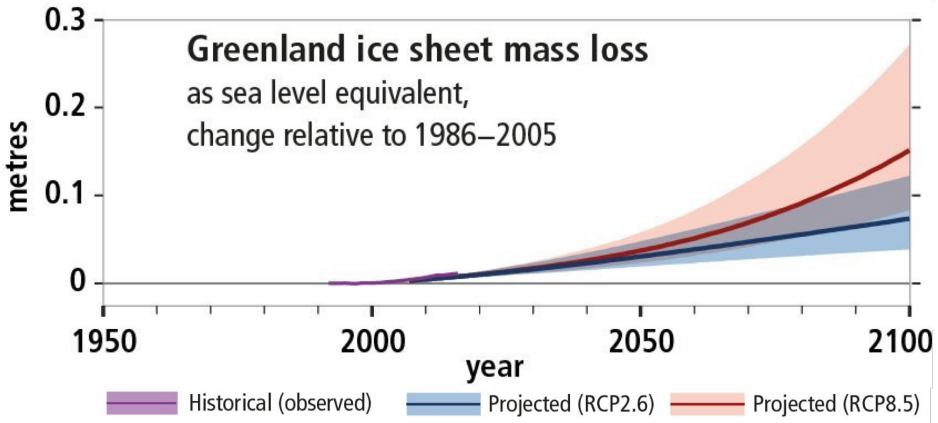
Figure 1.4: GrIS mass loss (m SLE): Observed historical changes since 1950, and projected
likely ranges for future changes under low (RCP2.6) and high (RCP8.5) emissions scenarios.
Figure credits: adapted from Figure SPM.1., Masson-Delmotte et al. (2018).

2. **What threshold of global mean temperature increase can be identified for
   irreversible GrIS mass loss?**
   A large focus of the current climate agreements is aimed at limiting the global
   mean temperature increase to a certain degree of warming. Therefore, a key
   variable of interest is the threshold of global mean temperature increase be-
   yond which GrIS mass loss is irreversible.

   Previous studies have used a three-dimensional ice sheet model coupled to a cli-
   mate model of intermediate complexity or to a global circulation model, where
   the information exchange between the climate and the ice sheet to calculate
   surface mass balance changes is based on temperature anomalies: a positive
   degree-day scheme (Ridley et al., 2005; Huybrechts et al., 2011). These studies
   yield estimates of warming degree thresholds, after which the ice sheet would
   further decline without requiring additional climate forcing due to the positive
   feedbacks. A limitation of these model set-ups is that the surface mass balance
   is not based on melt energy calculation from the surface energy balance. Rather
   the SMB is based on an empirical temperature anomaly scheme, which may not
   be appropriate for a transitioning climate, hence affecting the estimated range
   of temperature perturbations that lead to irreversible deglaciation. Robinson
   et al. (2012) and Levermann et al. (2013) use a regional climate model of inter-
   mediate complexity coupled to an ice sheet model, and finds lower threshold
   values than earlier studies. These results indicate that explicitly accounting for
   the ice-albedo and SMB-elevation feedbacks is necessary.

3. **What tipping points for irreversible GrIS mass loss can be identified?**
   As indicated above, a change in forcing may lead to irreversible GrIS mass loss
   due to positive feedbacks. Previous studies indicate the presence of hysteresis
   in ice sheet evolution, where the current evolution depends on its historical
   state (Charbit et al., 2008; Ridley et al., 2010). This means, a reversal of the
   forcing that induced the ice sheet retreat is not enough to restore the ice sheet
   to its original shape. A tipping point is reached when a small additional change
   prompts the system to transition towards a new equilibrium, usually at an ac-
   celerating rate. Identifying early indicators that the system is nearing a tipping
   point can be helpful information for policy makers in order to timely mitigate
   the change.

   A widely used metric to indicate the tipping point for irreversible mass loss
   is SMB=0. Greenland's ice caps, that is land-ice not attached to the main ice
   sheet, and glaciers are retreating (Bolch et al., 2013). Because of their smaller
   volume and area, glaciers and ice caps (GICs) are much quicker to respond
   to a changing climate. Using a high resolution regional climate model, Noël
   et al. (2017) identify an early indicator to a tipping point in the GICs in 1997
   at the time that the runoff rate increases faster than the melt rate. At this
   stage, the firn layer is no longer capable of buffering extra melt. Arguably the
   same mechanism is to be expected over the GrIS in the future in response to
   climate change. Other thresholds are a negative SMB (Gregory et al., 2004) or
   a negligible amount of ice discharge due to inland retreat (Ridley et al., 2005).

   A recent study by Gregory et al. (2020), using an ice sheet model coupled to
   a global climate model, addresses the above questions of GrIS irreversibility.
   Contrary to earlier studies, this study does not identify a particular warming
   threshold that marks the irreversibility of GrIS mass loss, but rather shows a
   broader temperature range within which the transition takes place. The au-
   thors argue that this differences relates to their use of a General Circulation
   Model (GCM) (Smith et al., 2020), that is, albeit its low spatial resolution of
   7.5° longitude by 5° latitude, able to capture atmospheric dynamical effects
   such as changes in snowfall and cloud physics in response to changes in the ice
   sheet topography.

4. **How does the changing GrIS affect the regional and global climate?**
   The climate affects the ice sheet, but the ice sheet also affects the climate.
   Ice sheets interact with the atmosphere as it constitutes as a barrier to atmo-
   spheric flow. Changes in ice sheet geometry may influence the location of semi-
   permanent synoptic scale pressure systems, and therefore may shift precipita-
   tion regimes. Recently observed atmospheric anomalies have been linked to
   increased surface mass loss (McLeod and Mote, 2016). It is uncertain whether
   these anomalies are anthropogenic, or within natural variability, and whether
   the frequency of blocking events will change in the future (Hanna et al., 2016).

   The GrIS also interacts with the global climate via the ocean by discharging
   meltwater. The sinking of cold, fresh water in the Arctic is thought to drive
   the large-scale oceanic circulation known as the Gulf stream or North Atlantic

Meridional Overturning Circulation (NAMOC). The northward branch of the NAMOC is a warm water current that transports heat towards Europa. Changes in GrIS meltwater production may slowdown the NAMOC, resulting in the decrease of the heat transport from equatorial regions to higher latitudes (Hu et al., 2009; Bakker et al., 2016) and subsequent changes in European climate.

1.6   State-of-the-art in coupling Earth System Models and Ice Sheet Models

Studying the effects of feedbacks on the evolution of GrIS mass change in a warming climate requires technical developments to the modelling tools that are currently available to the climate and ice sheet modelling community. Here we shortly describe the current tool-set, and the technical challenges that arise from the research needs.

Earth System Models (ESMs) are the primary tools to make projections of future global climate change. An ESM is a numerical representation of the Earth. It consists of a number of component models that represent various spheres of the Earth, i.e, the atmosphere, the ocean, the land, sea-ice, land-ice. The component models are a set of differential equations to approximate fluid motion, and/or parameterization schemes to describe state changes with empirical relationships for processes that are not (or cannot be) explicitly solved. A 3D mesh discretizes the component domain in smaller volumes (grid cells). Provided with external (time-dependent) forcing of solar radiation, and/or greenhouse gas emissions, the differential equations and parameterizations in each grid cell are solved for a predefined time-step size. The component models are coupled to one another to exchange information about changes in state and flux variables on the interface between one model and the other (for example, the land-atmosphere interface). Together, the coupled model system advances the Earth state in time, outputting time-dependent behavior of the Earth system. This is called an ESM simulation.

Historically, the earliest climate models that would simulate global general circulation patterns consisted of atmospheric circulation models coupled to ocean circulation models, referred to as Atmosphere-Ocean General Circulation Models (AOGCMs). Over the years, much advances have been made in the climate modelling community to more comprehensively represent the Earth system (Edwards, 2011), illustrated in Figure 1.5. Advances include the increases spatial and temporal resolution, and more complex physics (such as cloud physics) and biochemistry (such as the carbon cycle).

The results of ESM simulations provide important input to the IPCC report chapter on the physical science base of 21st century climate change. The Coupled Model Intercomparison Project (CMIP) (Meehl et al., 2000) is the framework within which scientists agree on guidelines for these model experiments. CMIP is initiated for comparability of the results from different modelling centers. Several emission scenarios are formulated to capture the spread of likely prospective social and economic pathways. The main parameters in these scenarios include population change,

greenhouse gas emissions, and land-use change. The current assessment cycle is the Coupled Model Intercomparison Project phase 6 (CMIP6). The results of the physical science base are presented in the IPCC Sixth Assessment Report in 2021 (Masson-Delmotte et al., 2021). The CMIP6 scenarios are called Shared Socio-economic Pathways (SSPs) (O'Neill et al., 2016). They range from a low forcing scenario (SSP1-2.6), to medium stabilization scenarios (SSP2-4.5 and SSP5-3.4OS), to very high emission scenarios (SSP3-7.0 and SSP5-8.5). The last two numbers of the scenario name indicate the radiative forcing value in W m^2 at the year 2100. The previous cycle, CMIP5, was the base of AR5 (Church et al., 2013). The CMIP5 emission scenarios are called Representative Concentration Pathways (RCPs) (van Vuuren et al., 2011), and also range between 2.6 and 8.5 W m^2.

The uncertainty related to the magnitude and rate of the ice-sheet contribution to 21st century SLR was recognized in the IPCC's AR5, and was highlighted as a key uncertainty (Church et al., 2013). This led to the establishment of the Ice Sheet Model Intercomparison Project for CMIP6 (ISMIP6), with its primary goal to estimate past and future sea level contributions from the GrIS and Antarctic Ice Sheet (AIS), together with associated uncertainties (Eyring et al., 2016; Nowicki et al., 2016). Its secondary goal is to investigate feedbacks between the ice sheet and climate, and impacts of ice sheets on the Earth system. Several modelling experiments have been formulated within ISMIP6 to systematically investigate the above. These include experiments with stand-alone Ice Sheet Model (ISM)s for which the multi-model results are published by Goelzer et al. (2020), experiments with ESMs for which the multi-model results are published by Fettweis et al. (2020), and experiments with bidirectionally coupled ESM-ISMs.

ISMs are numerical tools used to gain insight in the dynamics of ice sheets. Several approximations of the Navier-Stokes equations for fluid motion are suitable for describing ice flow. The Shallow Ice Approximation (SIA) is a first-order approximation that is widely used for paleo ice sheet simulations over glacial/interglacial timescales. It assumes that the main ice deformation is from the driving stress due to gravity, and from basal shear (Morland and Johnson, 1980; Morland and Smith, 1984), which translates to the vertical shear stress being dependent on the local thickness and on the surface slope. SIA is suitable to simulate large bodies of grounded ice with little local spatial variation in surface slope and ice velocities, however it is problematic when lateral shear and longitudinal stresses are large in relation to the driving stress, and they cannot be neglected, as they are in the SIA. A first-order approximation for ice flow with little basal traction is the Shallow Shelf approximation (SSA). In the SSA flow equation, the gravitational driving stress is countered by the longitudinal stresses (Morland, 1987; MacAyeal, 1989). More advanced ice sheets models employ a combination of SIA/SSA, where SIA is used for grounded ice and SSA for floating ice, and sometimes a form of hybrid SIA/SSA dynamics for ice streams. Another category of more advanced ISMs are the models with a higher order approximation of flow. An example is the Blatter-Pattyn higher-order approximation, which accounts for longitudinal stresses and transverse stress gradients, making it more appropriate to simulate dynamic behaviour of ice streams (Blatter,
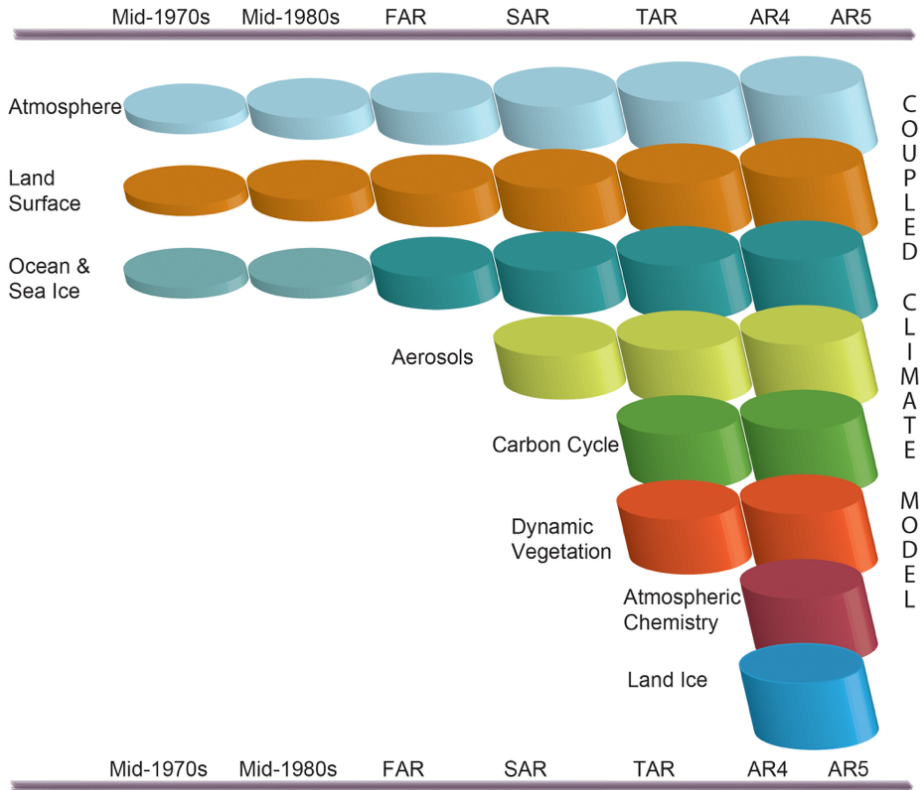
Figure 1.5: The development of coupled climate models that have been used in the IPCC Assessment Reports over the last 35 years. It shows how different components were coupled into climate models over time, with most recently: land-ice. Figure credits: WG I, Fig. 1.13 IPCC AR5).

1995; Pattyn, 2003). In addition to the flow approximation, the ISM contains parameterizations for physical processes that are not explicitly solved.

In technically integrating land-ice processes modelled by ISMs into ESMs, there has been much recent progress (Pollard, 2010; Vizcaino, 2014; Goelzer et al., 2017; Rybak et al., 2018; Hanna et al., 2020). Vizcaino et al. (2013) and Alexander et al. (2019) highlight the importance of computing SMB based on the surface energy balance; melt parameterizations based on temperature cannot simulate climate feedbacks and interactions in a physically realistic way. How realistic the SMB calculation is depends on the snow physics scheme (Van Kampenhout et al., 2017), the albedo calculation (Helsen et al., 2017), and model resolution (Gregory and Huybrechts, 2006; Lofverstrom and Liakka, 2018; Van Kampenhout et al., 2019), among other factors.

The addition of ice sheet flow to an ESM brings challenges due to the discrepancy in the required model resolution, both spatially and temporally. The land and atmosphere components of an ESM typically operate on grids with a resolution of 1°

(~100 km), taking internal time steps every hour or half-hour. The spatial resolution of an ISM is typically in the order of kilometers to tens of kilometers, and the temporal integration time is in the order of months or years. The spatial and temporal gap poses issues in terms of remapping and conserving of mass and energy in coupled climate/ice sheet models (Vizcaino, 2014). Finally, simultaneously simulating large-scale climate processes and local-scale ice sheet processes takes a considerable amount of processor core hours. Combined with the long response time of ice sheets and the desire for long simulations, the associated computational demand is challenging. Asynchronous and periodically coupling schemes are proposed as a solution (e.g., Lofverstrom et al. (2020)).

1.7   Research objectives

As outlined above, there are many open science questions regarding contemporary climate change and the role of land ice on the multidecadal and multicentennial time scales that are relevant for anthropogenic climate change. To find answers, it is advocated to further integrate climate dynamics and ice sheet dynamics. This dissertation aims to make a step towards a deeper understanding about the interactions and feedbacks between the GrIS ice flow, the surface mass balance, and the global Earth system. The following research questions are addressed in this dissertation:

1. **What model developments are necessary to integrate the main interactions and feedback mechanisms between the Greenland Ice Sheet and the Earth system in a model that simulates Earth system dynamics?**
   ESMs coupled to ISMs are important tools to better understand how ice sheet-climate interactions and feedbacks affect GrIS mass loss. As discussed above, the coupling between ESMs and ISMs brings major technical challenges. The main coupling features that are needed to simulate GrIS dynamics within an Earth System Model are identified and implemented using the Community Earth System Model version 2 (CESM2) (Danabasoglu et al., 2020) and the Community Ice Sheet Model version 2 (CISM2) (Lipscomb et al., 2019).

2. **Which processes are captured through the new ice sheet/climate model coupling?**
   To assess the gain from including the coupling features in CESM2-CISM2 indicated in objective (1), a comparison is done between a steady-state pre-industrial simulation and a simulation under a high CO_2 forcing scenario. The aim is to show the coupling features that enable the model to simulate a consistent co-evolution of climate and ice sheet.

3. **What estimates for 21st century GrIS mass loss does the coupled model provide for the SSP5-8.5 scenario?**
   The coupled CESM2-CISM2 framework is used to carry out simulations under historical (1850-2014) and SSP5-8.5 scenario (2015-2100) forcing. The simulations follow the protocols for coupled ice sheet–climate model experiments in

the framework of ISMIP6, Nowicki et al. (2016). The projection of 21st century global climate change is examined, as well as the projected GrIS contribution to global mean sea level. Results are compared to CESM2 simulations without an interactive ice sheet.

4. **How does the GrIS respond as an integral part of the Earth system to elevated atmospheric CO_2 on a multicentennial timescale?**
The coupled CESM2-CISM2 framework is used for a 350-year transient simulation with an idealized CO_2 scenario and a steady-state control simulation of the pre-industrial era. The purpose of this idealized scenario is to distinguish direct responses of climate and ice sheet from lagged responses and feedbacks.

   Processes of multicentury GrIS mass loss are investigated, with a focus on ice sheet/SMB/climate interactions and feedbacks. The timing and magnitude of the GrIS response in relation to global climate change, and the relative importance of the processes that govern GrIS behavior are investigated, as well as nonlinearities in the response to the forcing and apparent accelerations in the GrIS contribution to SLR.

1.8   Outline

Chapter 2 addresses research objectives 1 and 2. The chapter provides details on the coupled model that is used in this dissertation. Section 2.3 describes the coupling framework between the Earth System Model CESM2 and the Ice Sheet Model CISM2. The coupling features across model components are demonstrated in section 2.4.

Chapter 3 addresses research objective 3. The coupled model CESM2-CISM2 is used to simulate the period 1850-2100 under historical and SSP5-8.5 forcing. The analysis covers the model projection of 21st century global climate change and GrIS response.

Chapter 4 addresses research objective 4. The coupled model CESM2-CISM2 is used to simulate a multicentury, idealized elevated CO_2 scenario. The analysis focuses on the processes that are related to the acceleration of GrIS mass loss.

Concluding remarks and recommendations to improve and expand on this work are provided in Chapter 5.

Chapter 2

Description and demonstration of the coupled Community Earth System Model v2 - Community Ice Sheet Model v2 (CESM2-CISM2)

Sommige klimmen op elkaar schouders.
'Wie ben jij?' roepen ze.
'Bewolkt,' roep ik.
'Zwaar of half?' vragen ze.
'Licht,' zeg ik. 'Licht bewolkt.'

Toon Tellegen *Daar zijn woorden voor*

Earth system/ice sheet coupling is an area of recent, major Earth System Model development. This work occurs at the intersection of glaciology and climate science and is motivated by a need for robust projections of sea level rise. The Community Ice Sheet Model version 2 is the newest component model of the Community Earth System Model version 2. This paper describes the coupling and novel capabilities of the model, including: (1) an advanced energy-balance-based surface mass balance calculation in the land component with downscaling via elevation classes; (2) a closed freshwater budget from ice sheet to the ocean from surface runoff, basal melting, and ice discharge; (3) dynamic land surface types; and (4) dynamic atmospheric topography. The Earth system/ice sheet coupling is demonstrated in a simulation with an evolving Greenland Ice Sheet under an idealized high CO_2 scenario. The model simulates a large expansion of ablation areas (where surface ablation exceeds snow accumulation) and a large increase in surface runoff. This results in an elevated freshwater flux to the ocean, as well as thinning of the ice sheet and area retreat. These ice sheet changes result in reduced Greenland surface albedo, changes in the sign and magnitude of sensible and latent heat fluxes, and modified surface roughness and overall ice sheet topography. Representation of these couplings between climate and ice sheet is key for the simulation of ice and climate interactions.

2.1 Introduction

Land ice exists in the Earth system where perennial snow fields can form and develop into flowing ice masses (Agassiz, 1840). Once land ice has formed, the climate modulates ice dynamics by controlling processes of mass loss and gain at the ice sheet boundaries (Nye, 1963). Subsequently, as ice sheets evolve, they interact with the climate in ways that modify their own evolution (Fyke et al., 2018). The Earth system contains many such feedback mechanisms, including both positive (amplifying) and negative (moderating) processes. Feedback mechanisms between ice sheets and climate have been extensively studied. These include feedbacks between melt and albedo (Box et al., 2012), elevation and Surface Mass Balance (SMB) (i.e., the difference between accumulation and ablation at the surface) (Edwards et al., 2014a), SMB and ice discharge (Lipscomb et al., 2013; Goelzer et al., 2013), ice-sheet runoff and calving, ocean circulation, sea ice, ice-sheet climate (Day et al., 2013), and ice-sheet topography and atmospheric circulation (Ridley et al., 2005). Despite this body of work, much remains to be understood in the field of ice-sheet/Earth system feedbacks (Fyke et al., 2018) — including discovery of new feedback loops. Lack of understanding stems in part from the lack of fully coupled ice-sheet/Earth system models.

The modelling of ice-sheet response to climate change, and the response of the Earth System to ice sheet change, is an active, challenging area of research (Vizcaino, 2014). This research is largely motivated by the urgent need to better constrain projections of anthropogenic sea level rise. For example, the Greenland Ice Sheet (GrIS) and Antarctic Ice Sheet (AIS) have been losing mass at an accelerating rate in the last several decades (Velicogna et al., 2014; Tapley et al., 2019; Shepherd et al., 2019;

Velicogna et al., 2020), and are now major contributors to global mean sea level rise. Ice-sheet/Earth system interactions are a key aspect of this accelerating trend and must be studied in the coupled context over decadal to centennial timescales in order to develop robust future sea level projections in support of climate understanding, mitigation, and adaptation.

Previous work on integrating ice sheets into an Earth System Model (ESM) for present-day ice sheet configurations has been done by e.g. Ridley et al. (2005); Mikolajewicz et al. (2007); Vizcaino et al. (2008); Lipscomb et al. (2013); Vizcaino et al. (2014); Lofverstrom et al. (2020). Work on paleo climates, which usually spans longer time scales, has been done with an ESM of Intermediate Complexity (EMIC) (e.g., Fyke et al. (2011); Liakka et al. (2012)), and ESMs using asynchronous climate/ice sheet coupling (Gregory et al., 2012; Lofverstrom et al., 2015; Lofverstrom and Liakka, 2018).

Here, we present the coupling between the Community Earth System Model version 2 (CESM2) and the Community Ice Sheet Model version 2 (CISM2). This work extends preliminary coupling efforts with CESM1 and the Glimmer-CISM ice sheet model (Rutt et al., 2009), which focused on the development of the SMB calculation and application of this (one-way) coupled model to simulation of the GrIS response to future climate change (Lipscomb et al., 2013). CESM2-CISM2 is designed to interactively simulate the effects of climate on largely terrestrial ice sheets (and vice versa). At present, the main application of the model is to project future multi-century-scale mass loss of the GrIS in the broader Earth system and its contribution to global mean sea level change. Dynamic simulation of the Antarctic Ice Sheet is as of writing not included due to technical advances needed in order to simulate marine ice sheets, particularly regarding ocean-shelf coupling. Within the framework of the Ice Sheet Model Intercomparison Project for CMIP6 (ISMIP6) (Nowicki et al., 2016; Eyring et al., 2016), this paper and a companion paper on model spin-up (Lofverstrom et al., 2020) serve as the primary background documentation for coupled Atmosphere-Ocean General Circulation Model - Ice Sheet Model (AOGCM-ISM) ISMIP6 experiments using CESM2 (Muntjewerf et al., 2020a,b). Beyond ISMIP6, CESM2-CISM2 is intended to simulate past, present, and future climates, in which ice sheet dynamics and ice-sheet/Earth system interactions are considered important aspects of the overall system.

Interactive coupling of the AIS is not supported in the model versions that are described here and used for coupled ISMIP6 simulations. The main challenges involve ocean interactions with marine-based ice, which are essential for modeling the AIS. Work is under way to support interactive coupling with the AIS and paleo ice sheets, in addition to the GrIS, in future versions of CESM.

This chapter is organised as follows. Section 2.2 describes the model and its components. Section 2.3 describes the coupling between CESM2 and CISM2. Section 2.4 demonstrates the coupled CESM2-CISM2 for the GrIS with a pre-industrial simulation and a simulation under an idealised scenario of high atmospheric CO_2. Section 2.5 discusses the novelty of the coupled model and the potential for future developments. Finally, Section 2.6 presents primary conclusions.

2.2 Model Description

CESM2 is a state-of-the-art, coupled ESM primarily maintained at the National Center for Atmospheric Research (NCAR). With atmosphere, land, ocean, sea-ice, and ice sheet components that interactively exchange state information at run-time, CESM2 allows for realistic simulations of Earth's climate (Danabasoglu et al., 2020). The sections below provide detailed descriptions of the physics and interactions that are relevant for realistic Earth system/ice-sheet coupling. A comprehensive description of CESM2 can be found in Danabasoglu et al. (2020).

2.2.1 The Atmosphere Model

Atmospheric processes are simulated by the Community Atmosphere Model version 6 (CAM6), using a finite-volume dynamical core (Lin and Rood, 1997; Gettelman et al., 2019). The model operates on a nominal 1° (0.90° latitude × 1.25° longitude) horizontal grid and 32 levels in the vertical with the upper boundary at 3.6 hPa (∼40 km). CAM6 includes substantial improvements of every atmospheric physics parameterization compared to its predecessor CAM5, except for radiative transfer. The Cloud Layers Unified by Binormals (CLUBB) (Bogenschutz et al., 2013) scheme has replaced earlier schemes for boundary layer turbulence, shallow convection and cloud macrophysics. The two-moment cloud microphysics scheme (MG2) (Gettelman et al., 2015) has been updated. The major innovation in MG2 is to carry prognostic precipitation species – rain and snow – in addition to cloud condensates. MG2 interacts with the MAM4 aerosol microphysics scheme (Liu et al., 2015) to calculate condensate mass fractions and number concentrations. The improved cloud microphysics reduce cloud biases over Greenland, including the representation of cloud liquid water and longwave cloud forcing (Lenaerts et al., 2020). Parameterizations of subgrid-scale surface drag have been modified from CAM5. First, topographic orientation (ridges) and low-level flow blocking effects have been incorporated into the orographic gravity wave scheme (Scinocca and McFarlane, 2000). Second, the boundary layer form drag is now parameterized with the scheme of Beljaars et al. (2004), which improves the representation of orographic precipitation (notably over southeast Greenland), near-surface wind, and turbulent heat and moisture fluxes (van Kampenhout et al., 2020).

2.2.2 The Ocean Model

Ocean processes are simulated by the Parallel Ocean Program version 2 (POP2) (Smith et al., 2010; Danabasoglu et al., 2012). POP2 runs on a nominal 1° horizontal grid with a displaced pole over Greenland to avoid grid singularities in the Arctic Ocean. This has the additional benefit of relative high effective resolution around Greenland and in the deep water formation regions in the Labrador Seas. The vertical z-coordinate is discretized in 60 levels, with uniform 10 m spacing in the upper 160 m, increasing to 250 m in the deep ocean. POP2 conserves volume.

2.2.3   The Land Model

Land processes are simulated by the Community Land Model version 5 (CLM5) (Lawrence et al., 2019), which includes a wide range of biogeophysical and biogeochemical processes and snow hydrology. CLM5 uses the same nominal 1° horizontal grid as CAM6. To represent spatial heterogeneity in the landscape, CLM5 uses a fractional approach where calculations are carried out over a hierarchy of surface types. The uppermost level of the hierarchy is the *land unit*; each grid cell is divided into fractions representative of glacier, lake, wetland, urban, vegetated, and crop surfaces. The second, *column* level captures heterogeneity in state variables within each land unit. In the case of the glacier land unit, columns are defined based on surface elevation. In the following, such a column is referred to as an Elevation Class (EC) (see (Lipscomb et al., 2013)). The elevation classes allow to account for the impact of subgrid scale variations in topography on the surface mass balance and surface energy balance calculations. To be able to downscale the SMB of a previously non-glaciated grid box to the ice sheet model grid, virtual elevation classes exist. Virtual elevation classes are ECs in vegetated land units. They exist in a predefined domain, in this case the greater terrestrial Greenland area. Finally, the different vegetated land units have a Plant Functional Type (PFT). This allows for a variety of crop and vegetation types, including bare ground.

Vertical discretization is different between soil and snow within the model: the soil column has a fixed number of layers, while snow/firn has a variable number of layers and a maximum allowed snow depth H_{max}. Vegetated land units have 15 layers, the lower 5 being specified as bedrock. The subsurface of glacier land units consists of 15 ice layers that are fully frozen and impervious to water infiltration. Snow/firn is represented by up to 12 snow layers, depending on the total thickness. Each snow layer has a prescribed maximum thickness that is larger for deeper layers. When a snow layer exceeds its maximum thickness, excess mass is transferred downward. If there is no layer beneath, a new layer is initialized. The CLM5 default H_{max} is 10 m water equivalent (WE). In areas with perennial snow cover, this depth allows the development of a firn layer that is sufficiently deep for firn hydrological processes, such as refreezing and storage of surface melt water. From fresh snow accumulation, the model simulates compaction of snow into firn, with prognostic density and "pore" space, considering the effects of snow mass overburden, snow metamorphism, and enhanced wind-driven surface compaction (Van Kampenhout et al., 2017).

Snow albedo is calculated using the Snow, Ice, and Aerosol Radiation model (SNICAR), which accounts for vertically-resolved solar absorption, snow grain size evolution, and snow with impurities from aerosols (Flanner and Zender, 2006; Flanner et al., 2007). SNICAR simulates the spectral albedo of snow in a multi-layer approximation, to account for vertically heterogeneous properties and heating. Albedo is computed for five spectral bands, accounting for grain size changes and aerosol heating and scattering. The resulting albedo is averaged to the visible and near-infrared bands used in CLM5. The capability to simulate aerosol deposition on snow allows for studies of its impact on surface albedo and snow melt (e.g., Li and Flanner (2018)).

Heat and water fluxes and phase changes between liquid and solid water are calculated in all vertical layers for each column and/or PFT given the overlying atmospheric heat fluxes as upper boundary condition. The lower boundary is assumed to have a net zero heat flux. CLM5 calculates the surface energy fluxes separately for the snow-covered and snow-free fractions of a land unit.

Surface runoff is routed to the ocean by the Model for Scale Adaptive River Transport (MOSART) (Li et al., 2015). Transport is based on present-day topography gradients, and is simulated with time-varying velocities and channel water depths.

2.2.4   The Sea-Ice Model

Sea ice is represented by the Los Alamos National Laboratory sea ice model version 5 (CICE5) (Hunke et al., 2017). Sea-ice dynamics are determined by horizontal transport, ridging, and elastic-viscous-plastic rheology. The sea-ice temperature and salinity profiles are resolved in eight layers in the vertical for each thickness category in an ice thickness distribution. Also, a three-layer snow model calculates the vertical temperature distribution in the snow pack on the sea-ice. The horizontal grid is shared with the ocean component.

2.2.5   The Land-Ice Model

Ice sheets are simulated by the CISM2 (Lipscomb et al., 2019). CISM2 is a parallel, three-dimensional thermomechanical ice sheet model that can solve several approximations of the Stokes equations for incompressible viscous flow. The default ice-flow solver for Greenland simulations in CESM2 is a depth-integrated higher-order approximation based on Goldberg (2011). By using a depth-integrated effective viscosity, the model achieves accuracy close to that of the higher-order Blatter-Pattyn approximation (Blatter, 1995; Pattyn, 2003), but at much lower computational cost. At present, the Greenland domain is a 4-km rectangular grid based on a polar stereographic projection, using 11 terrain-following sigma levels in the vertical. Basal sliding is parameterized in CISM2 with a pseudo-plastic sliding law as described by Aschwanden et al. (2016). In standard Greenland simulations, ice discharge at marine margins uses a flotation criterion, where all floating ice immediately calves to the ocean. CISM2.1 also supports more advanced calving schemes, potentially more appropriate for ice sheets with large ice shelves.

2.3   Earth System/Ice Sheet Coupling

The description of the coupling between CESM2 and CISM2 is organized in four subsections (Figure 2.1). Support for interactive, time-evolving ice sheets is currently limited to Greenland. Glaciated regions elsewhere (i.e., the Antarctic ice sheet and smaller ice caps and mountain glaciers) are treated as in the default CESM2 configuration with prescribed ice sheets. See for more details the CESM2 Land Ice technical

documentation Leguy et al. (2018) and the CLM5 technical documentation Lawrence et al. (2020).
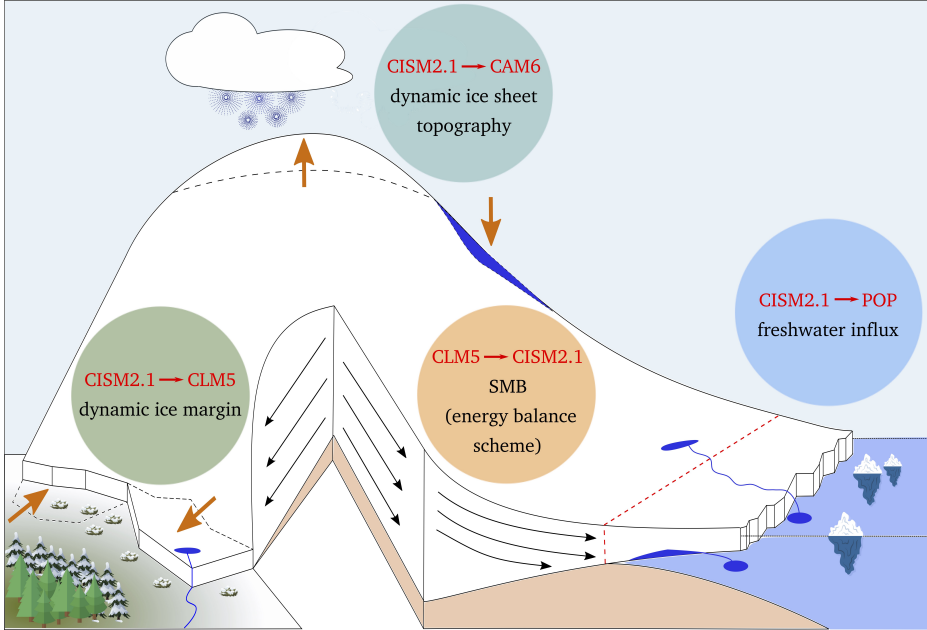
Figure 2.1: Schematic of four elements of coupling between ice sheets and other Earth system components, courtesy of M. Petrini.

2.3.1 Surface Mass Balance Calculation

The SMB is calculated explicitly using the melt that is calculated from the surface energy balance, and not based on a parameterization. The calculation is done in CLM5 and on multiple elevation classes per grid cell. The SMB is defined as the difference between accumulation from precipitation, and surface loss from runoff and sublimation:

$$\text{SMB} = Precipitation - Runoff - Sublimation, \tag{2.1}$$

Precipitation can fall as either snow or rain. While snowfall contributes directly and positively to the SMB, rainfall can only contribute positively if it refreezes within the snow pack. Otherwise it contributes to runoff and is routed together with (non-refrozen) melt water to the ocean by the river model MOSART. The SMB can therefore be reformulated as the sum of snowfall and refrozen rainfall, minus the sum of melt and sublimation:

$$\text{SMB} = Snowfall + Refreezing - Sublimation - Melt. \tag{2.2}$$

Drifting snow processes (Lenaerts et al., 2012) are not yet accounted for in CESM2.
Melt energy is calculated from the sum of net surface radiation, latent and sensible
turbulent surface fluxes, and ground heat fluxes at the atmosphere-snow interface
(Lawrence et al., 2019):

$$E_M = SW_{net} + LW_{net} + LHF + SHF + GHF \qquad (2.3)$$

where E_M denotes available melt energy, SW_{net} is the net shortwave radiation at the
surface, LW_{net} is net longwave radiation, LHF is latent heat flux, SHF is sensible heat
flux, and GHF is ground heat flux, all in W m^{-2}.

The surface energy and mass budgets of ice sheets depend strongly on elevation
(Van de Wal et al., 2012; Hermann et al., 2018). However, differences in horizontal
resolution between CISM2 (4 km) and CLM5 (nominal 1-degree) imply that multi-
ple CISM2 grid cells exist within each CLM5 cell. This discrepancy in resolution is
particularly challenging around the steep ice sheet margins, where and the coarse
CLM5 resolution makes it difficult to resolve gradients in the surface mass balance.
To overcome this challenge, CLM5 uses multiple ECs (Fyke et al., 2011; Lipscomb
et al., 2013; Vizcaino et al., 2014; Sellevold et al., 2019) to account for subgrid-scale
variations in elevation over glaciated land units. This method bins the glaciated
land unit fraction of each CLM5 grid cell based on the resolved topography in the
higher-resolution ice-sheet model. For each EC, surface energy fluxes and their im-
pact on SMB are calculated independently by downscaling atmospheric variables at
the CLM5-CAM6 coupling frequency (every half hour in the current model configu-
ration). The CLM5 grid cell temperature is downscaled to the EC elevation using a
uniform lapse rate (by default -6 K km^{-1}). Model sensitivity to the lapse rate choice
was assessed in Sellevold et al. (2019). With the fixed lapse rate and the assumption
of vertically uniform relative humidity, EC-specific potential temperature, specific hu-
midity, air density, and surface pressure are determined. To tune the magnitude of
the elevation feedback, the incoming longwave radiation can optionally be down-
scaled using a default lapse rate of -32 Wm^{-2} km^{-1} (Van Tricht et al., 2016). Finally,
precipitation is partitioned into rain or snow according to the elevation-corrected
near-surface temperature. Precipitation is assumed to be 100% snow (frozen) if the
downscaled surface temperature is below -2°C, and rain (liquid) if the temperature
is above 0°C. Between these temperatures, precipitation falls as a mix of rain and
snow based on a linear ramping relationship. To conserve energy, a sensible heat flux
is applied at the surface to compensate for the latent energy absorbed or released in
rain-snow conversion.

Elevation classes allow to account for the impact of subgrid scale variations in to-
pography on the surface mass balance and surface energy balance calculations. The
model uses ten elevation classes, with boundaries at 0, 200, 400, 700, 1000, 1300,
1600, 2000, 2500, 3000, and 10000 m. An additional vegetated EC allows snow to
accumulate and form glacier ice in previously non-glaciated grid cells. Within each
elevation class, the "representative" (or actual) elevation is set as the mean of all
CISM grid cell surface elevations falling within it. Typically, one or two elevation
classes are sufficient to represent the distribution of ice sheet elevations within a

CLM5 grid cell in the relatively flat regions of the ice sheet interior. Conversely, more elevation classes are needed to capture topographic variation on the steep ice sheet margins. The remaining ECs in a grid cell are virtual; that is, their area fraction is zero. SMB calculations in virtual ECs allow to realistically initialise a temperature profile when an EC first acquires a nonzero area value. The elevation classes calculations are done in a predefined domain. Figure 2.2 shows how much area each EC covers on the CLM grid for a pre-industrial, equilibrated GrIS (Lofverstrom et al., 2020) (see section 2.4).
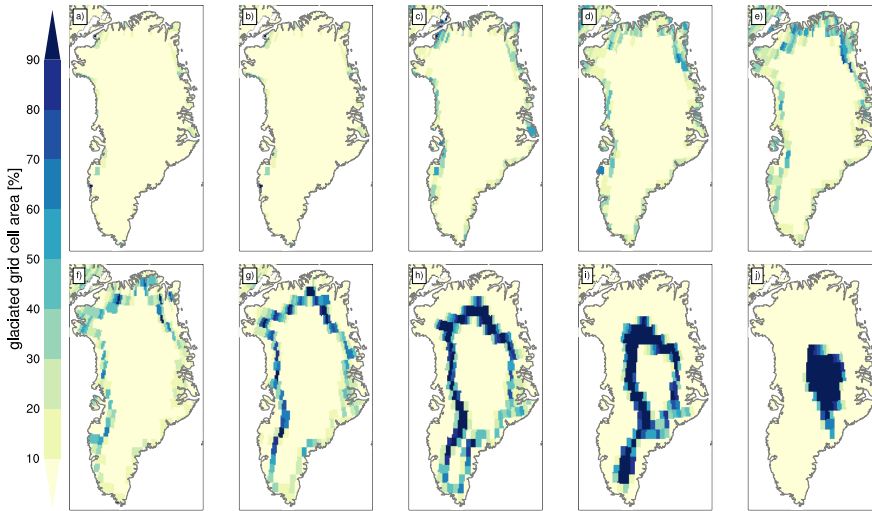
Figure 2.2: Area percentage of glacier elevation classes in the glaciated fraction of land model CLM5 grid cells, for the default 10 elevation bins: a) EC1: 0–200 m; b) EC2: 200–400 m; c) EC3: 400–700 m; d) EC4: 700–1000 m; e) EC5: 1000–1300 m; f) EC6: 1300–1600 m; g) EC7: 1600–2000 m; h) EC8: 2000–2500 m; i) EC9: 2500–3000 m; j) EC10: 3000–10000 m. The ice sheet topography is from the pre-industrial simulation described in Section 4.

Physically, the interface between snow and ice is characterised as the point at which densities of solid ice are reached, and no additional snow compaction as a result of overburden pressure can occur. In CLM5, the conversion of snow to ice is based on depth; any snow accumulation exceeding a prescribed threshold (10 m WE by default) is assumed to turn to ice. In CESM simulations without interactive ice sheets, this ice is sent to the ocean as a solid runoff flux, but in coupled CESM-CISM runs, it is sent to the ice sheet model as accumulation (i.e., a positive SMB). Mass variations in snow and firn layers are only considered in the land model, while variations in ice mass "belong" to the ice sheet model. Therefore, the SMB sent from CLM5 to CISM2 is defined as the difference between (annually integrated) ice accumulation and ablation. Accumulation is the sum of snowfall and refrozen rain wherever the maximum allowed CLM5 snow depth is reached (10 m WE by default). An equal amount of mass is then removed from the lowest snow layer to allow refreshing of surface density and albedo (the albedo calculation is detailed in Section 2.2.3). The annual integrated melt that takes place on bare ice (which may be exposed after

the snow pack has disappeared) is passed to the ice sheet model as ablation (i.e., a negative SMB). In ice-free regions of CISM2, negative SMB from CLM5 is ignored. The SMB definition used in the ice sheet-land model coupling does not take into account variations of mass within the snow and firn pack. Thus, the SMB received by CISM reflects long-term changes in ice thickness, but not seasonal-to-interannual variations in snow depth. This approximation is valid for equilibrated climate and SMB, but introduces a bias during transient climates, especially in the vicinity of the Equilibrium Line Altitude (ELA). The reason is a delay in the transition from positive or negative SMB, or vice versa, when using SMB that includes snow pack changes, versus using SMB as the difference between ice accumulation and ice ablation.

After annual SMB is accumulated in CLM5 for each glacier-covered EC, the SMB is remapped from the coarse land model grid to the higher-resolution ice sheet model grid through trilinear interpolation and renormalization. The remapping procedure targets a) local accuracy, b) smooth SMB gradients without any imprint of the coarse land model grid, c) preservation of the spatial distribution of accumulation and ablation areas, and d) conservation of mass. To reach all these targets, the downscaling algorithm proceeds as follows:

1. The CESM2 coupler (the interface between the land and ice-sheet models) accumulates and averages the SMB in each land model grid cell over the coupling interval (annually for synchronous land/ice sheet coupling).

2. SMB in each EC is (horizontally) bilinearly interpolated from the land model to the ice-sheet model grid.

3. In each ice-sheet grid cell, the SMB is linearly interpolated in the vertical between adjacent ECs to the appropriate surface elevation in the ice-sheet model.

4. Mass discrepancy (%) following these interpolations is quantified by separately evaluating the total area-weighted accumulation and ablation on the source grid (i.e., the land-model, accounting for elevation classes) and destination grid (i.e., the ice-sheet model). This results in two normalization factors, one for the accumulation region and one for the ablation region. For the coupled GrIS simulations described here, the mass discrepancy usually is less than 10%, and thus the normalization factors fall between 0.9 and 1.1.

5. In each ice-sheet grid cell, the SMB is multiplied by the appropriate normalization factor to ensure mass conservation.

2.3.2   Freshwater Fluxes from the Ice Sheet to the Ocean

Surface runoff, ice discharge, and basal melt comprise the freshwater flux from the ice sheet to the ocean. Marine-terminating glaciers discharge ice directly to the ocean. Thus, the coupling is only from ice to ocean, and no information is passed from the ocean to the ice sheet. As a result, CESM does not yet simulate ocean-forced melting of marine-terminating glaciers, as described by Goelzer et al. (2020) and Slater et al. (2020) for standalone GrIS experiments for ISMIP6. Surface runoff consists of liquid

water at the ice sheet surface that is not refrozen in the snow pack. Surface runoff fluxes are computed in the surface hydrology module of CLM5. Basal melting occurs where the base of the ice sheet is at the pressure melting point due to frictional and geothermal heat. Basal melt flux is computed in CISM2 (for details, see Lipscomb et al. (2019)) and sent to the ocean, where it is treated in the same way as surface runoff from CLM5.

The relevant aspects of water fluxes to the ocean, from a coupling perspective, are the source (i.e., land or ice-sheet model), timing, and phase (i.e., solid or liquid). Surface runoff fluxes are calculated in the land model and coupled to the ocean on hourly time scales. The ice sheet model, on the other hand, computes annual ice discharge and basal melting rates, which are supplied to the ocean at a constant rate throughout the following year (without seasonal modulation). Solid ice fluxes from ice discharge are melted instantaneously (temperature of ice is assumed to be 0°), and the energy for the phase change is extracted from the global surface ocean. For liquid fluxes, the temperature difference between the liquid-phase water flux and the ocean temperature is assumed to be negligible, such that no net heat transfer occurs. Since the water volume in POP2 is fixed, the ocean model converts freshwater fluxes to virtual salinity fluxes.

Water flux routing depends on the model component. Surface runoff from the land model is routed downhill by the river transport model MOSART to the ocean. Once on the ocean grid, the water is distributed in the upper three model levels (upper 30 m) using an estuary box model (EBM; Sun et al. (2017)). Solid ice discharge and basal melt fluxes from the ice-sheet model are sent to the ocean using nearest-neighbour conservative regridding. Solid-phase water fluxes are distributed horizontally in the surface ocean using a Gaussian distribution with radius of 300 km. This horizontal distribution mitigates unrealistic local frazil sea-ice growth caused by extraction of heat to melt ice, especially in winter when the ocean surface is near the freezing point.

2.3.3 Dynamical Land–Ice Sheet Mask

The advance and retreat of ice sheet margins changes land-surface properties (e.g. surface albedo), which in turn impacts the full range of surface processes. Each CLM5 grid cell can represent several different land units (e.g., vegetated and glaciated surface types) at the same time. Ice-sheet/climate coupling thus requires accommodation for dynamic (interactive, or time-evolving) land units, as the ice sheet margin changes.

Dynamic land units are implemented as follows. In each CLM5 grid cell, glacier elevation classes are initialized in accordance with the topography in CISM2. As the ice-sheet topography evolves, the coupler remaps the new ice-sheet geometry from CISM2 to CLM5. The coupler also uses the ice sheet extent in CISM2 to recompute the fractional glacier coverage (in each elevation class) in each CLM5 grid cell that overlaps the CISM2 domain. Adjustments are made to the total glacier area of the grid cell, as well as the glacier area and mean topographic height in each elevation

class. CLM5 land units are updated at the CISM2 coupling frequency (i.e., annually
for synchronous climate/ice sheet coupling).

The transition from vegetated to glaciated land unit when the ice sheet margin
advances (or vice versa, from glaciated to vegetated when the margin retreats) re-
quires conservation of mass and energy in each CLM5 grid cell. As the total glacier
area in each CLM5 grid cell changes, the area of each subgrid column (i.e., elevation
class) also changes. Each column in CLM5 has a different subsurface water, energy,
carbon and nitrogen content. Specifically, vegetated columns have soil layers, while
glacier columns have subsurface ice layers. CLM5 does not adjust the below-ground
states for water and energy when the fractional areas of land units change. Instead,
correction fluxes are applied to ensure conservation of mass and energy. Runoff
fluxes (either positive or negative) are generated to conserve liquid water and ice,
and sensible heat fluxes are generated to conserve energy. These correction fluxes
are typically small compared to the physical fluxes of water and energy, and they
are distributed evenly throughout the following year to MOSART and CAM6, respec-
tively. Regarding soil carbon and nitrogen, glacier land units typically do not track
this. When the ice sheet retreats, it is assumed to contribute zero carbon and ni-
trogen to the newly vegetated land unit's soil column. When the ice sheet advances,
however, the glacier land unit will store the carbon and nitrogen from the previously-
vegetated land unit. The carbon and nitrogen contents remain unchanged until the
area deglaciates again. Further details can be found in Leguy et al. (2018), section
6.3 and Andre et al. (2020), section 2.27.

When the ice sheet retreats, the vegetation types that regrow on deglaciated land
are determined by the input map of PFTs. The default PFT distribution in CESM2
is based on present-day observations (Bonan et al., 2002). By default, land areas
under the GrIS are prescribed as bare ground. A more realistic approach is to change
the vegetation to be consistent with the evolving climate, but this requires running a
vegetation model offline (e.g., Kaplan et al. (2003)) and manually updating the PFT
map.

Running with POP2, the land-sea mask must remain fixed at run-time. The
Modular Ocean Model version 6 (MOM6) (Adcroft et al., 2019), which will replace
POP2 in future CESM versions, can simulate an evolving ocean–ice sheet boundary,
but is not yet supported for coupled CESM-CISM applications with realistic ice sheets.

2.3.4 Dynamical Ice Sheet Surface Topography

As ice-sheet geometry evolves over long timescales, changes in topography can in-
fluence atmospheric circulation. For century-scale or longer coupled ice-sheet/Earth
system simulations, this becomes an important feedback. In the case of CESM2,
this means updating the topographic boundary conditions. The topography updat-
ing routine modifies CAM6's boundary conditions and restart files based on ice-sheet
elevation changes in CISM2. The required files for this workflow are a source file of
CISM2 topography, a destination file of surface boundary conditions on the CAM6
grid, and a high-resolution topography data-set to inform on elevations over non-

ice-sheet-covered land surface regions. In our case, this data-set is the GMTED2010, a 30 arc-second (nominally 1 km resolution) global Digital Elevation Model (DEM) from the United States Geological Survey (USGS) on a rectilinear latitude-longitude grid (Danielson and Gesch, 2011). The topography updating procedure is as follows:

1. The regional ice-sheet topography from the 4-km rectangular CISM grid is bilinearly interpolated and merged with the full global 30-arcsecond DEM data-set.

2. The NCAR topography generation software for unstructured grids (NCAR_topo; Lauritzen et al. (2015)) computes the surface topography variables and maps them to the CAM 1-degree finite volume grid. The mapped variables are surface geopotential (PHIS); the standard deviation of large subgrid-scale topography (SGH) (approximately >3 km and <grid-scale); and the standard deviation of small subgrid-scale topography (SGH30) (approximately <3 km). The latter two variables estimate subgrid surface roughness, and are used in the CAM6 parameterizations of orographic gravity wave drag and the Beljaars turbulent orographic form drag, respectively.

3. Updated CAM surface topography variables are merged into the standard CAM default restart file and topographic boundary condition in preparation for the next run period.

2.4   Model Demonstration

To demonstrate the coupling across model components in CESM2-CISM2, we compare the simulated GrIS energy and mass fluxes in a pre-industrial simulation and a simulation under a high CO_2 forcing scenario. Given that simulations with this model are computationally demanding, we have used simulations that are also used in a scientific application publication. We have tried to avoid any scientific relevance of the demonstrated analysis, as the aim is to illustrate two contrasting climate states, and show the coupling features that enable the model to simulate a transient but coherent climate between them. The analysis focuses on behaviour of the four coupling aspects that are described in Section 2.3 (SMB, ocean freshwater budget from Greenland, dynamic ice sheet margins, and surface topography updating).

2.4.1   Experimental Set-Up and Model Configuration

The pre-industrial (PI) steady-state simulation is designed following the guidelines of the Coupled Model Intercomparison Project phase 6 (CMIP6) as specified in Eyring et al. (2016), with a fixed atmospheric CO_2 concentration of 284.7 ppmv. The idealised high-CO_2 scenario (hereafter hCO_2) is a 350–year simulation that starts with a transient component in which the atmospheric CO_2 concentration increases by 1% per year for 140 years (until the CO_2 concentration is 1140 ppmv, or four times the pre-industrial value), after which it is held fixed until model year 350. The experimental set-up is described in detail in Nowicki et al. (2016).

Both simulations are initialized from the spun-up pre-industrial climate/ice sheet state described in Lofverstrom et al. (2020), of which the procedure is explained in more detail in Chapter section 3.2.4. In the spun-up state, the GrIS volume is about 12% larger than the observed present-day ice sheet (estimated 7.4 m sea level equivalent; Morlighem et al. (2017)), and the residual drift is ∼0.03 mm/yr of GrIS mass gain. The simulated ice sheet area is larger by 15%, with most of the differences in the north. Lofverstrom et al. (2020) provides a more detailed comparison of the spun-up GrIS with observations and regional climate model reconstructions.

The model configuration used here is the same as in CESM2 without an evolving GrIS, except for several minor modifications, as permitted by the ISMIP6 guidelines (Nowicki et al., 2016). These modifications were implemented to limit over-growth of the GrIS during the multi-millennial spin-up (Lofverstrom et al., 2020). First, the CLM5 default precipitation repartitioning as described in Section 2.3.1 is modified so that rain falling in sub-freezing conditions immediately runs off to the ocean rather than being converted to snow. This change compensates for excessive precipitation in the model (van Kampenhout et al., 2020). Second, we reduced the magnitude of the elevation feedback by turning off the downscaling of longwave radiation in the EC scheme. Also, we limited excessive ice sheet expansion by specifying that, for non-glaciated areas, ice sheet inception is only allowed in grid cells directly adjacent to the main ice sheet. Regarding interactive CISM2 parameters: the calving parameterization is based on a flotation criterion where any floating ice is assumed to calve immediately. The GrIS topography is updated annually at run-time in the land model based on the evolving ice sheet surface topography. Offline updates in the atmosphere model are done every 10 years.

2.4.2   Results

In the following analysis, the mean pre-industrial state is compared to a 20-year segment of the idealised high-forcing simulation (years 201–220). In this segment, the climate has warmed significantly and ice sheet changes are noticeable. The global mean surface temperature is 7 K warmer than the PI-mean. The GrIS area and volume are 7% and 3.8% smaller than in the PI, respectively (Table 2.1). The substantial mass loss between the PI and hCO$_2$ simulations (-13 Gt yr^{-1} compared to -1506 Gt yr^{-1}; Table 2.1) reflects rapid GrIS deglaciation in the hCO$_2$ case. Conversely, ice discharge decreases in the hCO$_2$ case, as the margin thins and migrates inland from the coast Muntjewerf et al. (2020b).

Surface Mass Balance

Figure 2.3 shows mean annual cycles of GrIS-integrated surface mass balance components. The PI SMB is positive for ten months of the year. The most negative SMB is in July (μ [σ]: -1.16 [0.95] Gt day^{-1}). The summer (June - July - August (JJA)) mean snowfall of 1.73 [0.55] Gt day^{-1} is slightly less than the annual value of 1.97 [0.27] Gt day^{-1}. Refreezing of meltwater within the snow and firn layers (2.71 [0.88] Gt day^{-1}) contributes substantially to the net SMB. However, the sum of melt

Table 2.1: Climate and ice sheet variables: mean [standard deviation] over the selected 20-year period.

		pre-industrial	hCO$_2$
Global			
	T$_{2m}$ (K)	287	294
GrIS			
	Area (m^2)	1.97×10^{12}	1.82×10^{12}
	Volume (m^3)	3.23×10^{15}	3.11×10^{15}
	SMB (Gt yr^{-1})	585 [85]	-1293 [217]
	Ice discharge (Gt yr^{-1})	574 [5]	196 [19]
	BMB (Gt yr^{-1})	-24 [0]	-17 [0]
	MB (Gt yr^{-1})	-13 [84]	-1506 [214]
	Rate of SLR (mm yr^{-1})	0.03 [0.23]	4.18 [0.59]
Greenland			
	Runoff DJF (Gt yr^{-1})	95 [22]	185 [31]
	Runoff JJA (Gt yr^{-1})	857 [118]	6197 [533]

and sublimation (4.98 [1.35] Gt day^{-1} and 0.61 [0.03] Gt day^{-1}, respectively) is larger than the sum of snowfall and refreezing, resulting in the slightly negative net summer SMB.

In the hCO$_2$ simulation, the number of months with a positive SMB decreases to seven, and the annual mean SMB is negative (Table 2.1). The extended melt season is characterised by both an earlier onset of the melt season (April, versus May in the PI) as well as a later ending (October-November, versus September in the PI). As in the PI run, the largest negative SMB is simulated in July (-27.09 [2.82] Gt day^{-1}), with melt as the main contributor (35.78 [2.89] Gt day^{-1}). Not all additional melt water contributes to the surface mass loss, as the amount that refreezes increases as well (to 7.44 [0.98] Gt day^{-1}). Snowfall decreases in the summer months, and increases in the fall and early winter. Sublimation decreases in the summer and increases during the rest of the year

The range of melting in these simulations agrees with a recent study by Tedesco et al. (2013), which put the extreme melt year of 2012 in historical perspective. Mean daily melt of about 6 Gt day^{-1} in July was modelled by MAR for the period 1958-2011, with a maximum of about 16 Gt day^{-1}. The modeled extreme melt in 2012 was 22 Gt day^{-1}, with is less negative than the CESM2.1 July average in hCO$_2$, but far more negative than PI values.

Figure 2.4 maps the climatological SMB in CISM2.1 for the two simulations. For PI, the model simulates ablation zones around all margins, with the widest ablation zone in the southwest. High SMB along the southeast coast is well represented, due to high precipitation from simulated storm tracks impinging on Greenland from the North Atlantic. The interior and the northern half of the ice sheet are much drier than the south, in accordance with present-day measurements and reconstructions (Ettema et al., 2010; Noël et al., 2018).
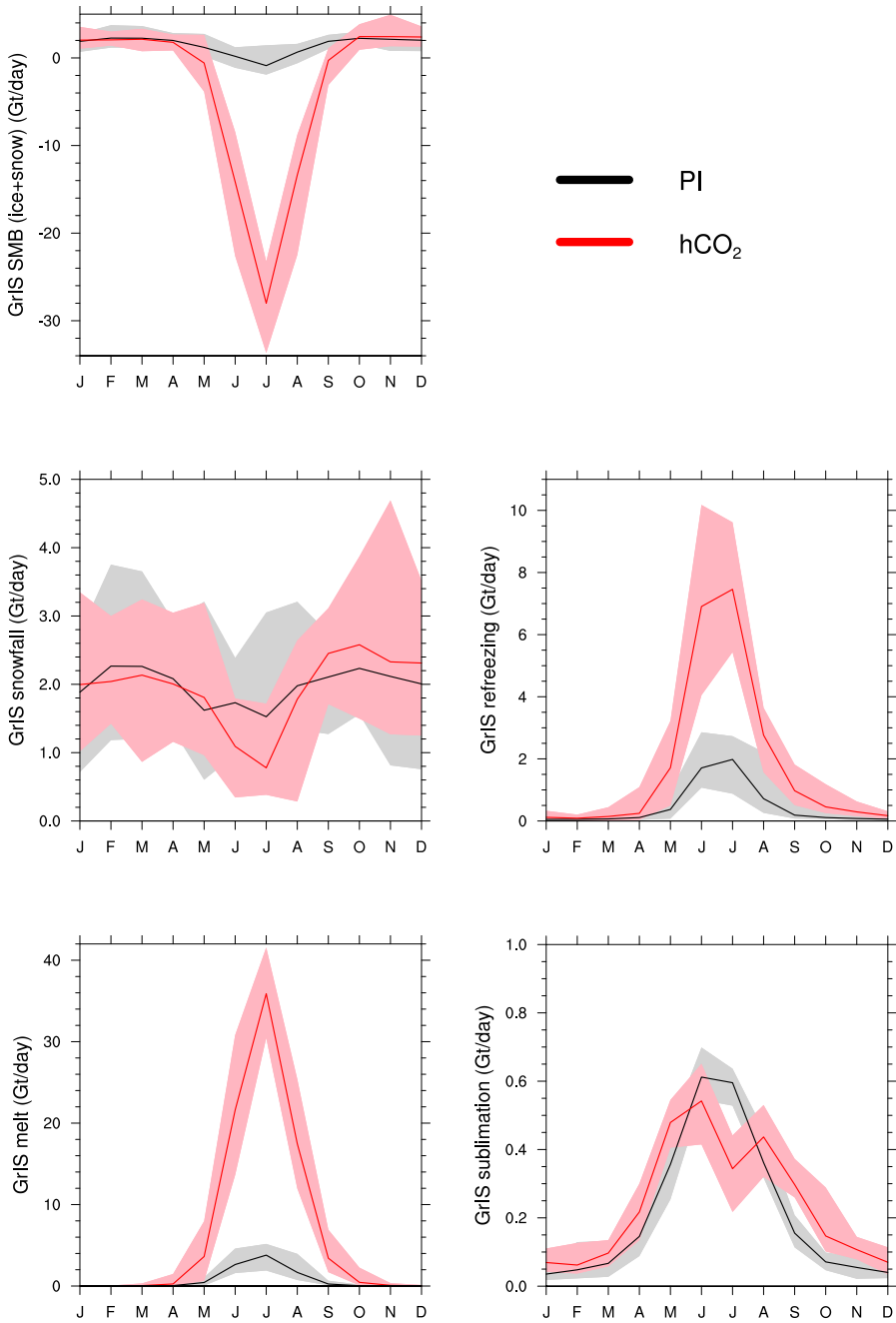
Figure 2.3: Climatology of the GrIS-integrated surface mass balance (Gt day^{-1}) and components (SMB = snowfall + refreezing - melt - sublimation) from the land model CLM5 for (black) pre-industrial forcing and (red) high atmospheric CO_2 forcing. Solid line is the mean, and shaded area is the range over the 20-year period.
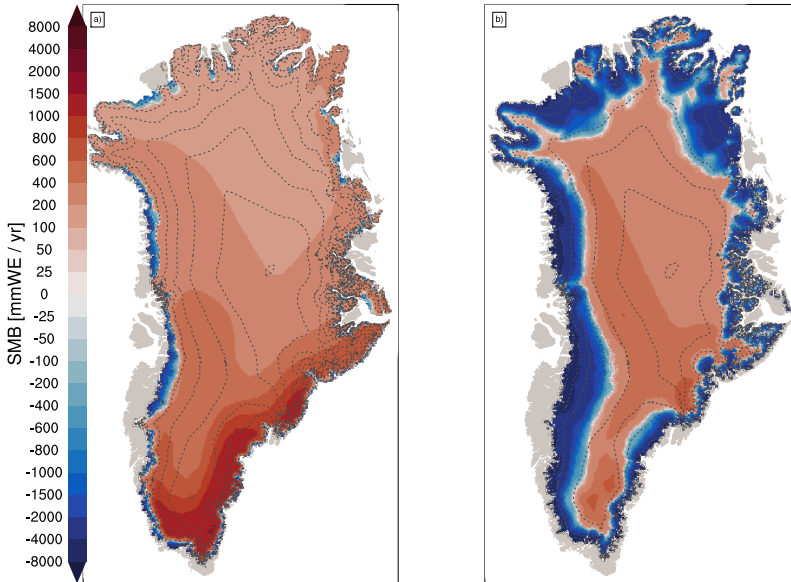
Figure 2.4: 20-year mean surface mass balance (mm WE yr^{-1}) from the ice sheet model CISM2 for (a) pre-industrial forcing and (b) high atmospheric CO_2 forcing. Accumulation zone in red, ablation zone in blue. Dashed lines show ice sheet elevation contours at 500-m intervals.

For the PI run, the GrIS-integrated annual-mean SMB is 585 [85] Gt yr^{-1} (Table 2.1). This is within the bounds of the SMB at the end of the spin-up simulation (591 [83] Gt yr^{-1}, Lofverstrom et al. (2020)). van Kampenhout et al. (2020) used observations and regional climate models to evaluate the GrIS climate and SMB for the period 1961-1990 in CESM2.1-only runs with non-evolving, present-day observed topography. The multi-ensemble mean GrIS SMB from this study is 508 [73] Gt yr^{-1}, slightly lower than for the PI CESM2.1-CISM2.1 run and in good agreement with the reconstruction by the regional climate model RACMO forced with reanalysis.

In the hCO$_2$ run, the integrated SMB decreases to -1293 Gt yr^{-1} (Table 2.1).The ablation areas expand, and the average equilibrium line altitude (ELA) rises above 2000 m. The SMB slightly increases in the high interior regions because of enhanced snowfall (Muntjewerf et al., 2020b; Sellevold and Vizcaino, 2020).

Figure 2.5 shows how the SMB simulation is coupled with the simulated climate over Greenland. In the PI, the average summer near-surface temperature is at least several degrees below the melting point for most of the GrIS except in the ablation areas, where it is at or near the melting point (Fig. 2.5a). In hCO$_2$, temperatures at or above the melting point largely correspond with the ablation areas (Fig. 2.5b). The map of temperature increase is not uniform (Fig. 2.5c), as the ablation areas (where the surface temperature is held at the melting point) warm less than the interior. Over the ablation areas (Fig. 2.4), albedo decreases in hCO$_2$ from greater exposure of bare ice (Fig. 2.5,d-f). The turbulent heat flux from the atmosphere to the ablation areas increases (Fig. 2.5g-i) as the atmosphere warms well above the melting point

(Fig. 2.5b-c), while the surface is constrained to the melting temperature.
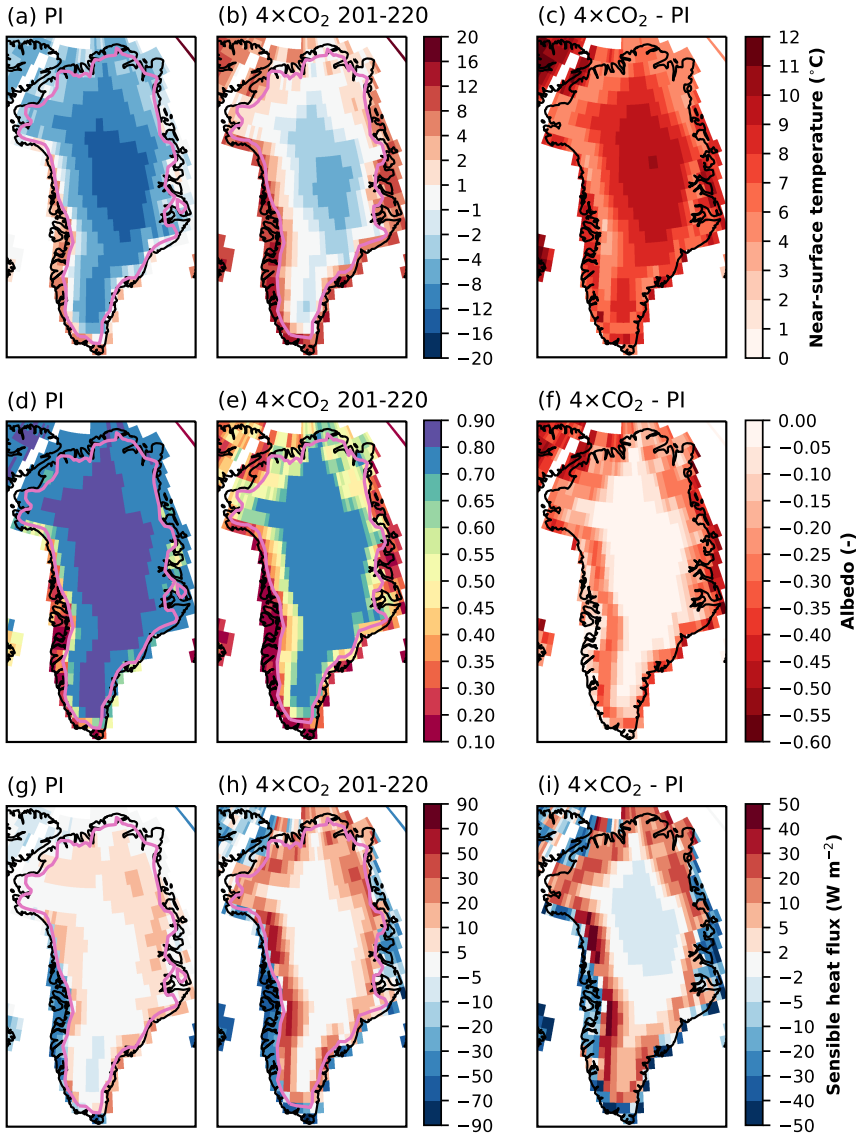
Figure 2.5: Simulated summer JJA Greenland climate from the land model CLM5 for pre-industrial forcing (first column), high atmospheric CO_2 forcing (hCO_2, years 201-220, second column), and difference (third column): (a-c) near-surface temperature (°C), (d-f) albedo, (g-i) sensible heat flux (positive from atmosphere to surface, W m^{-2}) .

Freshwater Fluxes

The simulated fluxes to the CESM2 ocean component include ice discharge in the solid phase, along with surface runoff and basal melt in the liquid phase. Basal melt is not discussed here, given that it is an order of magnitude smaller than ice discharge and surface runoff, and the simulation does not include ice shelves or sub-shelf melt. Figure 2.6a shows CISM2 ice discharge in the PI. The largest contributions are from Jakobshavn in the west, and from Helheim and Kangerlussuaq in the southeast. Muntjewerf et al. (2020a), Supplementary Information compared the simulated ice discharge in a CESM2-CISM2 historical simulation with observations for the recent decades. In the hCO_2 segment (Fig. 2.6b), the ice sheet margin has retreated inland and thinned around the margins. As a result, the ice discharge decreases by a factor of three (Table 2.1). Ice velocities increase in the intermediate area between the margin and the high interior as a result of increased topographic gradient due to greater thinning in the margins. The ocean receives the solid water flux corresponding to the ice discharge (Fig. 2.6c and 2.6d), with the highest inputs in the southeast and northeast.

The PI annual average runoff is 351 [45] Gt year^{-1}. On average, there is five times more runoff in the hCO_2 run than in the PI run (Table 2.1). This is due to a much higher peak in summer melting, as seen in the seasonal cycle of GrIS-integrated runoff in Figure 2.7a. Figure 2.7 shows the spatial extent of July runoff for the PI (left panel) and hCO_2 (right panel). The spatial pattern of runoff corresponds closely with the ablation simulation in Figure 2.4, with ablation zones being relatively narrow in the PI but extending far inland in the hCO_2. Figures 2.7d and 2.7e show where the JJA runoff enters the ocean in the PI and hCO_2, respectively. Consistent with the largest increases in ablation area and magnitude, the largest runoff increases in the hCO_2 are found along the western and southeastern coasts.

Margin Advance and Retreat

The difference in GrIS area between hCO_2 and PI is -0.15×10^6 km^2 (-7.6%) (Table 2.1). The loss of CISM ice-covered area in the hCO_2 case redistributes EC areas within CLM grid cells and replaces glacier land units with vegetation. Figure 2.8 compares the percentage of grid-cell glaciated fraction in the PI and hCO_2 simulations. The largest changes are found along the southern and eastern margins. This strongly affects land surface properties (e.g., albedo) and the energy exchange with the atmosphere in the deglaciated areas (Fig. 2.5). The largest albedo changes over Greenland correspond to deglaciated areas (compare Fig. 2.8 and Fig. 2.5d-f). The retreat of the ice sheet (e.g., in mid-eastern Greenland) reverses the sign of the summer sensible heat flux from positive (surface to atmosphere) to negative (atmosphere to surface) (Fig. 2.5g-h), since incoming radiation can warm the tundra above the melting point (Fig. 2.5b), while glaciated surfaces are held at the melting point (Fig. 2.5a). Further changes in the Greenland climate related to ice sheet margin retreat for the extension of the hCO_2 simulation to year 350 are shown in Muntjewerf et al. (2020b).
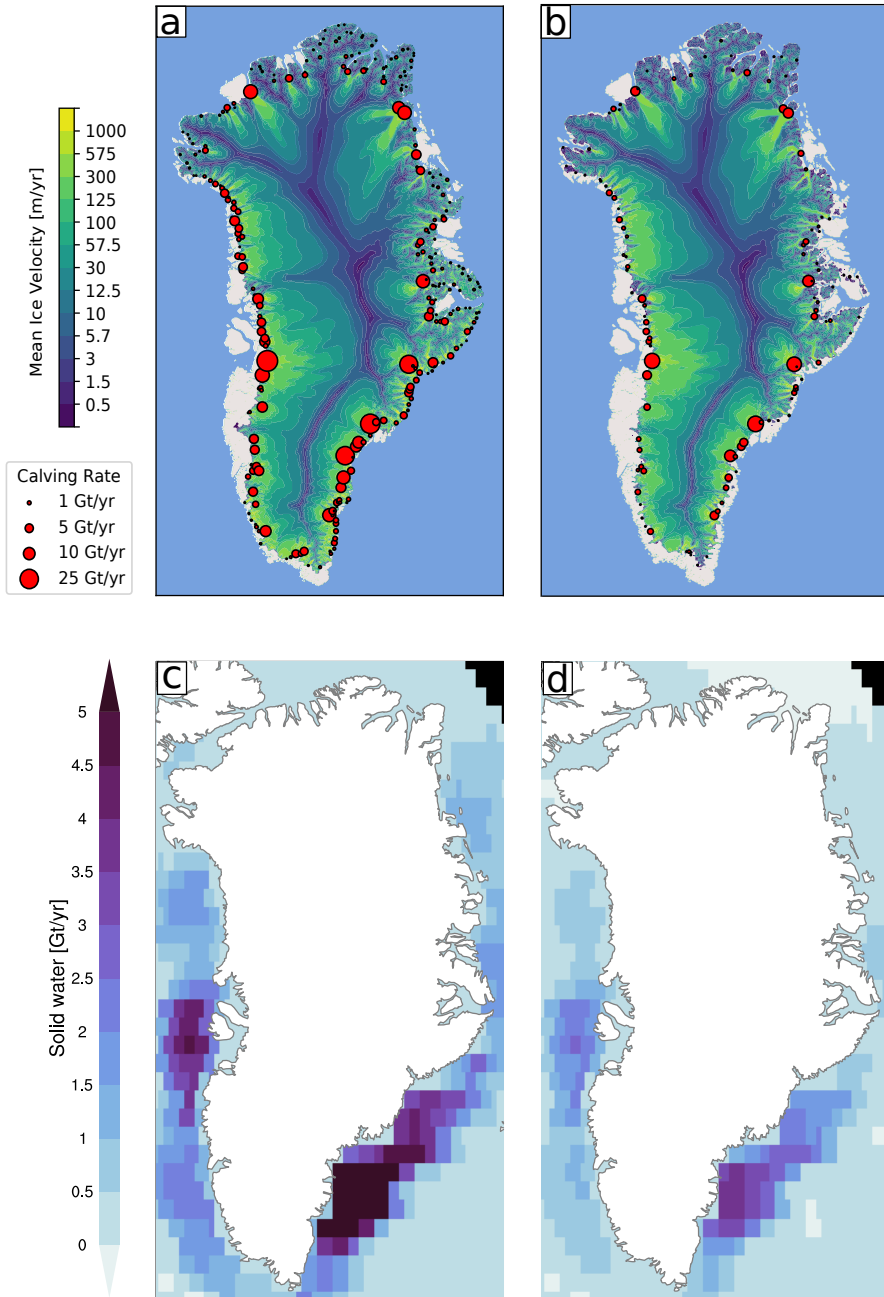
Figure 2.6: Simulated solid freshwater fluxes from Greenland (ice discharge) to the ocean. Top: CISM2 dynamic ice discharge for the modelled outlet glaciers (red circles; Gt yr^{-1}) and surface ice velocity (background, m yr^{-1}) for (a) pre-industrial forcing and (b) high atmospheric CO_2 forcing. Mean over the 20-year period. Bottom: POP2 solid phase freshwater input (Gt yr^{-1}) for (c) pre-industrial forcing and (d) high atmospheric CO_2 forcing. Mean over the 20-year period.
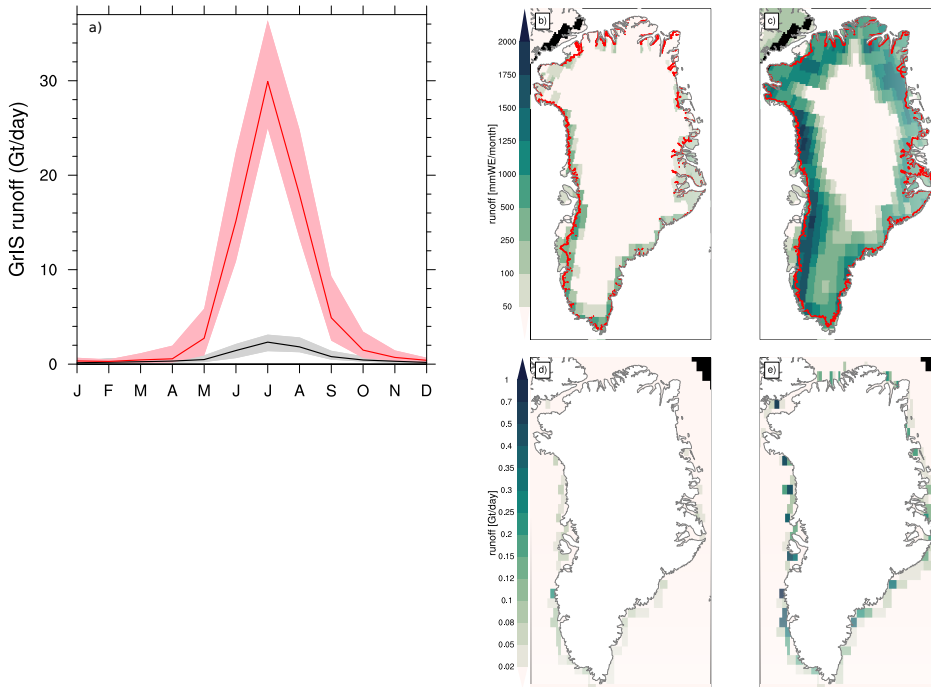
Figure 2.7: Runoff: a) climatology from the land model CLM5 of GrIS integrated runoff (Gt day^{-1}) for (black) pre-industrial forcing and (red) high atmospheric CO_2 forcing. Solid line is the mean, and shaded area is the range over the 20-year period. Spatial map of JJA Greenland runoff as generated in the land model CLM5 (mm WE month^{-1}) for b) pre-industrial forcing and c) high atmospheric CO_2 forcing; mean over the 20-year period. Red line denotes the ice sheet margin. Spatial map of JJA runoff from Greenland as received by the ocean model POP2 (Gt day^{-1}) for d) pre-industrial forcing and d) high atmospheric CO_2 forcing; mean over the 20-year period.

Ice Sheet Topography Changes

The total GrIS volume decreases by 0.12×10^6 km^3 (3.7%) (Table 2.1) in the hCO$_2$ run. Figures 2.9a and 2.9b show the surface elevation in CISM2, with the greatest thinning along the margins and in the south (Fig. 2.9c). Differences in elevation correspond with the spatial pattern of SMB changes in Fig. 2.4. Figures 2.9d and 2.9e show the corresponding surface elevation in the atmosphere model. While the atmosphere model cannot directly resolve small-scale ice sheet topography changes, these changes are captured in subgrid-scale topography variance fields: large-scale (3 km $< \sigma <$ 100 km; Figures 2.9g, 2.9h) and small-scale ($\sigma <$ 3 km) surface elevation variance (Figures 2.9j, 2.9k). As ice thins near the margin, the topography gradient increases over the ablation areas, resulting in increases in (both large and small) subgrid elevation variations. Anomalies for the small subgrid scale coincide largely in sign with those of large scale, albeit with reduced magnitude, with some exceptions around the areas of ice sheet retreat, particularly in the east. These might be related to the complex sub-grid topography of the region. As the margin thins
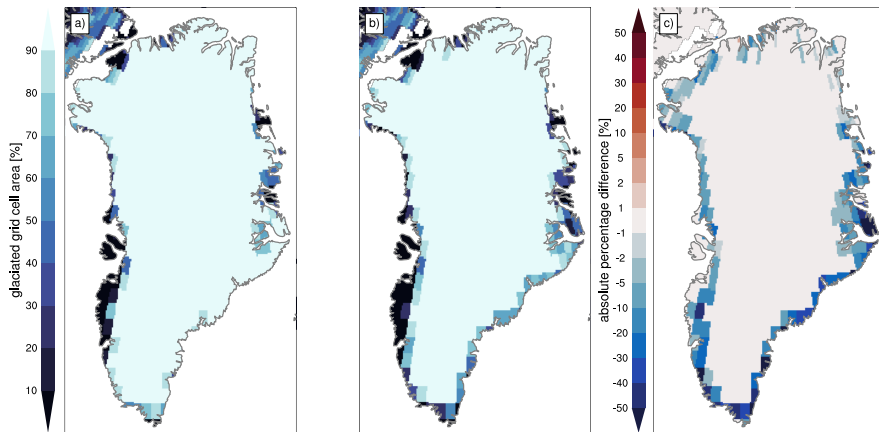
Figure 2.8: Simulated percentage of glaciated fraction (sum of all ECs) per grid cell in the land model CLM5 for (a) pre-industrial forcing, (b) high atmospheric CO_2 forcing, and (c) the difference of (a) and (b).

and retreats, the elevation differences between high, formerly ice-covered regions and lower, ice-free regions decrease. This results in some increases in the fine-scale topographic gradient.

2.5   Discussion

This study presents the coupled ice sheet and Earth system model CESM2-CISM2, which includes a higher-order ice sheet model, an advanced surface mass balance calculation with explicit simulation of albedo and refreezing, and a high- complexity ("IPCC-class") Earth System Model that accounts for simulated changes in ice sheet area, elevation, and freshwater fluxes to the ocean. The coupled model conserves mass and energy, an important feature for robust long-term simulations of climate and ice sheet changes (Fischer et al., 2014).

The elevation-class method used for SMB downscaling (Lipscomb et al., 2013; Sellevold et al., 2019), paired with conservative trilinear remapping, is used to bridge the spatial resolution gap between the land and the ice sheet components. Compared with previous model versions (Vizcaino et al., 2013, 2014), the SMB calculation has been substantially improved in CESM2 (Danabasoglu et al., 2020); e.g., through the implementation of a wind-dependent snow albedo scheme, an increased maximum allowed snow depth, and explicit simulation of snow and firn compaction (Van Kampenhout et al., 2017). Advances in the representation of clouds and turbulent fluxes have also contributed to a more realistic Greenland climate and surface melt. CESM2 simulates a realistic GrIS SMB for the historical period and a fixed present-day ice sheet topography (van Kampenhout et al., 2020) (Noël et al., 2019). The calculation of SMB in the land component permits direct coupling between SMB and climate, as
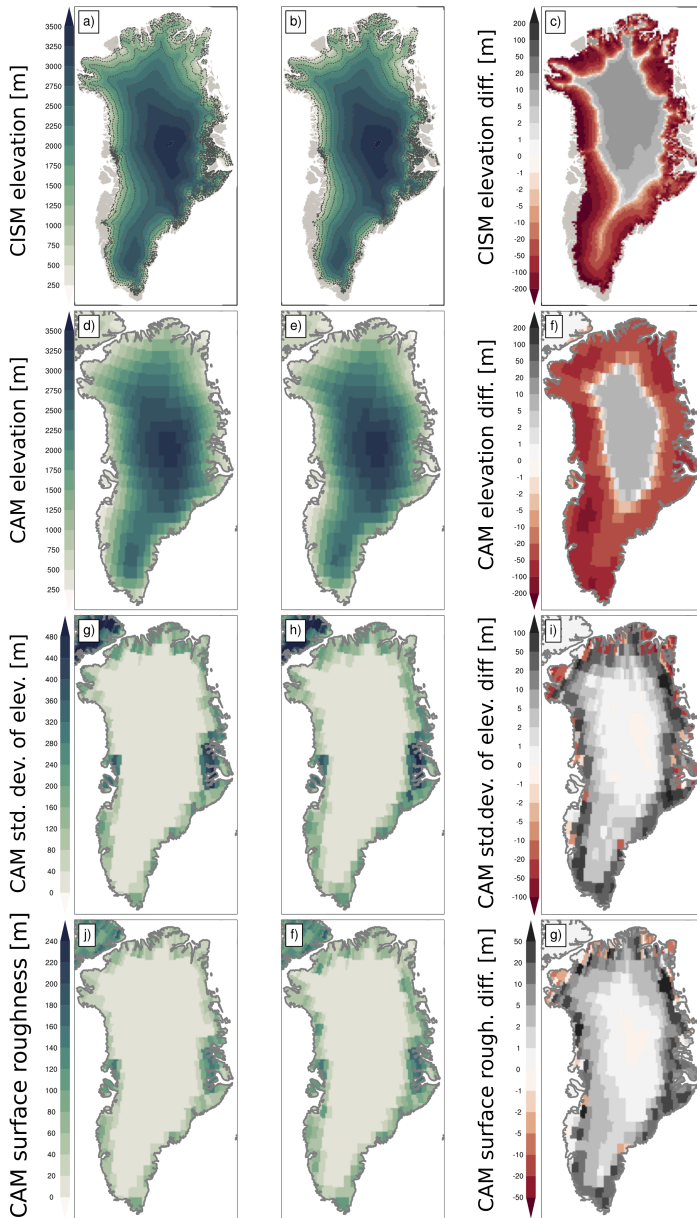
Figure 2.9: Greenland topography in the ice sheet model CISM2. Surface elevation (m) for (a) pre-industrial forcing, (b) high atmospheric CO_2 forcing, and (c) the difference of (a) and (b). Dashed lines are ice sheet elevation contours at 500-m intervals. Panels (d) and (e) show the surface elevation in the atmosphere model for these two periods, with the difference in (f). Panels (g) and (h) show large subgrid-scale standard deviation of surface elevation *SGH* (m) in the atmosphere model, with the difference in (i). Panels (j) and (k) show the small subgrid-scale standard deviation in elevation *SGH30* (m) in the atmosphere model, with the difference in (l).

for instance surface albedo affects the atmosphere–surface fluxes (see Fig. 2.4 and
2.5, where expanded ablation areas result in lower summer surface albedo). This is
an improvement over previous modelling efforts in which the SMB was typically cal-
culated offline with input from a climate model (e.g., Vizcaino et al. (2015); Ridley
et al. (2005); Gregory and Huybrechts (2006); Aschwanden et al. (2019)).

Compared to standard CESM2 with prescribed ice sheet geometry, the coupled
model provides more physically based runoff and ice discharge fluxes to the ocean,
as these correspond to the SMB calculation in the land model and the calving flux
in the ice sheet model. This enables spatio-temporally varying ice sheet freshwa-
ter fluxes to the ocean, which is important for realistically simulating the ocean re-
sponse to ice sheet meltwater (Lenaerts et al., 2015). The coupled model features
a dynamic (or "time-evolving") glacier mask that enables a more realistic represen-
tation of land processes in regions that glaciate when the ice-sheet margin expands
(or vice versa, become ice-free when the margin retreats). These transitions substan-
tially alter the turbulent and radiative surface fluxes (primarily in summer; section
2.4.2) as shown in the contrast between contiguous glaciated and non-glaciated ar-
eas in Greenland climate reconstructions (Ettema et al., 2010; Van den Broeke et al.,
2016).With the current calving parameterization that calves all floating ice, marine
terminating glaciers can not be simulated. This is a limitation as there are modelling
studies that indicate a competition between enhanced ice discharge from glacier ac-
celeration and decreased ice discharge from thinning due to surface mass loss Goelzer
et al. (2020); Slater et al. (2020).

The coupling between ice sheets and the broader Earth system will be further
developed in later model versions. Future model developments will include two-way
coupling to the ocean, as ocean thermal forcing can drive the retreat of marine-based
ice Joughin et al. (2012); Bondzio et al. (2018); Khazendar et al. (2019). Other
planned improvements include the implementation of a dynamic ice sheet–ocean
mask Straneo et al. (2013), especially for paleo studies Meccia and Mikolajewicz
(2018), as well as a dynamic land–ocean mask that adjusts to changing ice shelf
extent over the ocean. These developments will become feasible with the transition
from POP2 to MOM6 Adcroft et al. (2019) as the CESM ocean component, since
MOM6 allows ocean circulation in evolving ice-shelf cavities.

Also, runoff in the land surface hydrology model could be routed along dynamic
ice-sheet surface gradients, instead of being prescribed based on present-day topog-
raphy. Another desirable feature is dynamic vegetation, which can modify the climate
through albedo and ecosystem feedbacks (Sturm et al., 2005; Rombouts and Ghil,
2015; Thompson and Koenig, 2018). This feedback is potentially important for long
transient climate simulations (> 500 yr) where both ice sheets and vegetation may
change substantially due to low-frequency changes in external forcing, as in the study
by Ziemen et al. (2014).

Finally, we reflect on computational expense. As for all highly complex ESMs
with medium to high resolution atmosphere and ocean components, the computa-
tional cost of CESM2 is high, although the additional cost of running CISM is small
(less than 1% of the total model cost). The simulations presented here were run

on the Cheyenne high-performance computer, using 2160 processors with a load-balanced processor layout. The model cost is around 3000 processor-hours for one simulated year, with throughput of about 17.5 simulated years per wall-clock day; see Table 1 in Lofverstrom et al. (2020). Since much interest of coupled Earth system/ice sheet simulations lies in centennial or millennial timescales, techniques to reduce costs for long simulations are needed. One possible approach is the development of robust, flexible, modular coupling schemes, using "asynchronous" or "periodic synchronous" coupling (Pollard et al., 1990; Ridley et al., 2005; Mikolajewicz et al., 2007; Ziemen et al., 2014). A similar approach was adopted to generate the initial conditions for the simulations in this study (Lofverstrom et al., 2020).

2.6   Conclusion

This study describes and demonstrates the interactive coupling of CESM2 with CISM2. The current coupling is bi-directional throughout the ice sheet–snow–climate domain, and uni-directional through the ice sheet–ocean interface. This paper covers four primary aspects of the coupling:

- Energy-balance and SMB calculations in the land model, with SMB remapped to the higher-resolution ice sheet grid.

- Solid ice discharge from the ice sheet model to the ocean model.

- Dynamic surface types in the land model as the ice sheet advances or retreats.

- Evolution of the land–atmosphere boundary with changing ice-sheet surface topography.

We demonstrated the capabilities of the new model by comparing a pre-industrial simulation with a transient, high-CO_2 simulation. In the warmer climate, the GrIS-integrated SMB becomes negative for the annual mean, has a much larger amplitude in the seasonal cycle, and expanded ablation zones. With greater melt in low-elevation regions, the ice sheet margins thin. This results in steeper topographic gradient near the equilibrium line altitude, enhancing ice flow from the interior to the margins (Fig. 2.6a,b). The magnitudes of runoff and its seasonal variation increase. At the same time, the ocean receives less ice discharge as marine-terminating glaciers thin and recede inland. This illustrates the coupling between ice-sheet melt, ice discharge, and freshwater forcing to the ocean. As the ice sheet retreats, previously glaciated areas become bare soil or vegetated, reducing the surface albedo and modifying the magnitude and/or sign of turbulent heat exchange with the atmosphere. The evolving ice sheet topography alters the mean topography and sub-grid variability seen by the atmosphere model, modifying the atmospheric circulation.

CESM2-CISM2 is one of a small number of coupled ice sheet–climate models participating in the CMIP6 -endorsed ISMIP6 experiments (Nowicki et al., 2016), with studies of 1850–2100 historical and SSP5-8.5 simulations (Muntjewerf et al., 2020a), and of pre-industrial and transient 1% CO_2 simulations (Muntjewerf et al.,

2020b). These simulations are an important contribution to an international effort to include ice sheets as interactive components of Earth System Models.

Chapter 3

Greenland Ice Sheet Contribution to 21st Century Sea Level Rise as Simulated by the Coupled CESM2–CISM2

> Vanavond gaan we slapen
> en morgen zien we wel
>
> ———————————————
>
> Boudewijn de Groot *Avond*

The Greenland Ice Sheet mass balance is examined with an Earth system/ice sheet model that interactively couples the Greenland Ice Sheet to the broader Earth system. The simulation runs from 1850 to 2100, with historical and SSP5-8.5 forcing. By the mid-21st century, the cumulative Greenland Ice Sheet contribution to global mean sea level rise is 3 mm. During the second half of the 21st century, the surface mass balance becomes negative in all drainage basins, with an additional sea level rise contribution of 86 mm. The annual mean mass loss in the last two decades is 2.7 mm sea level equivalent yr^{-1}. The increased contribution from the surface mass balance (3.1 mm yr^{-1}) is partly offset by reduced ice discharge from thinning and retreat of outlet glaciers. The southern drainage basins contribute 73% of the mass loss in mid-century, but 55% by 2100, as surface runoff increases in the northern basins.

3.1   Introduction

During the past two decades, the Greenland Ice Sheet (GrIS) has lost mass at an increasing rate (Shepherd et al., 2019) and has become a major contributor to global mean sea level rise (SLR) (Chen et al., 2017). The polar ice sheets were identified in the Intergovernmental Panel on Climate Change (IPCC) Fifth Assessment Report (AR5) as large sources of uncertainty in 21st century SLR projections (Church et al., 2013) A recent expert assessment estimates that by 2100, the GrIS will contribute between 20 mm and 990 mm sea level equivalent (SLE), with a median of 230 mm SLE (Bamber et al., 2019). The uncertainty in SLR stems partly from insufficient understanding of the complex interactions and feedbacks among ice sheets, Surface Mass Balance (SMB), and climate (Fyke et al., 2018), highlighting the importance of studies with coupled Earth system/ice sheet models (Vizcaino, 2014; Goelzer et al., 2017).

Many studies on future ice sheet evolution have been done using regional climate models with static ice sheet topography (Tedesco and Fettweis, 2012; Rae et al., 2012; Lenaerts et al., 2015), or dynamic ice sheet models with prescribed climate forcing (e.g., Graversen et al. (2011); Aschwanden et al. (2019); Ruckamp et al. (2019)). By accounting only for climate–SMB interactions or ice sheet–SMB interactions, these studies miss interactions between ice sheet dynamics and climate. Further, some studies with partially coupled ice sheet–climate models have used positive degree-day (PDD) schemes, which parameterize melt based on the number of days the temperature is above the melting point (e.g., Ridley et al. (2005); Mikolajew-icz et al. (2007); Vizcaino et al. (2008); Huybrechts et al. (2011)). In new climate regimes, however, empirical relations between melt and temperature may no longer hold, and an explicit Surface Energy Balance (SEB) calculation is necessary (Bauer and Ganopolski, 2017).

Physics-based models that explicitly resolve the SEB and snowpack processes are needed to simulate feedbacks, such as the ice-albedo feedback (Bougamont et al., 2007). A main challenge is the fine horizontal grid resolution needed to realistically simulate SMB gradients (Van den Broeke et al., 2008). There has been recent progress in coupling an SEB-based SMB calculation with ice dynamics using

regional climate models of both intermediate complexity (Krapp et al., 2017; Born et al., 2019) and higher complexity (e.g., regional climate model MAR, Le clec'h et al. (2019)). However, the use of global models with SEB-based SMB to simulate Earth-system interactions with ice sheets has been limited (Vizcaino et al., 2008, 2015).

In this study, the Community Earth System Model version 2 (CESM2) (Danaba-soglu et al., 2020) with the Community Ice Sheet Model version 2 (CISM2) inter-active GrIS (Lipscomb et al., 2019) is used to simulate the period 1850-2100 under historical and SSP5-8.5 forcing. The model includes an SEB-derived SMB calculation with multiple elevation classes (Fyke et al., 2011; Lipscomb et al., 2013; Sellevold et al., 2019), and thus is able to capture ice sheet–SMB–climate feedbacks. The simulations follow the protocols for coupled ice sheet–climate model experiments in the framework of the Ice Sheet Modeling Intercomparison Project for CMIP6 (IS-MIP6; Nowicki et al. (2016)). This paper presents the CESM2-CISM2 projection of 21st century global climate change and GrIS response, as well as the projected GrIS contribution to global mean sea level. Results are compared to CESM2 simulations without an interactive ice sheet.

3.2 Method

3.2.1 The Community Earth System Model (CESM2)

The Community Earth System Model version 2 (CESM2) (Danabasoglu et al., 2020) is a comprehensive, fully-coupled Earth system model that is contributing simula-tions of past, present, and future climates to the Coupled Model Intercomparison Project phase 6 (CMIP6) (Eyring et al. (2016)). CESM2 includes component mod-els of the atmosphere (Community Atmosphere Model version 6 (CAM6)), land (Community Land Model version 5 (CLM5; Lawrence et al. (2019)), ocean (Parallel Ocean Program version 2 (POP2); Smith et al. (2010); Danabasoglu et al. (2012)), sea-ice (Los Alamos National Laboratory sea ice model version 5 (CICE5; Hunke et al. (2017)), river transport (Model for Scale Adaptive River Transport (MOSART); Li et al. (2015)), and land-ice (CISM2; Lipscomb et al. (2019)). The simulations described here were run with nominal 1-degree horizontal resolution (∼110 km at the equator) in the atmosphere, land, ocean, and sea ice components. The ice sheet model was run on a 4-km limited-area grid centered on Greenland.

3.2.2 Interactive Earth System/Ice-Sheet Coupling

CESM2-CISM2 supports an evolving Greenland ice sheet that is interactively coupled to other Earth system components. The SMB is computed in CLM5 as the difference between annual snow accumulation and surface ablation, derived from the surface energy balance and snow pack hydrology. The SMB is calculated for multiple eleva-tion classes in glaciated grid cells to account for subgrid-scale variations in surface climate and SMB components (Fyke et al., 2011; Lipscomb et al., 2013; Sellevold et al., 2019). The SMB is remapped from the CLM5 grid to the higher-resolution

CISM2 grid, using a trilinear interpolation scheme that conserves both the total ablated and the total accumulated mass (Leguy et al., 2018).

Freshwater fluxes from the GrIS to the ocean are the sum of surface runoff from CLM5, and basal meltwater and ice discharge from CISM2. Surface runoff is routed to the ocean via MOSART, accounting for the surface slope, and basal meltwater reaches the ocean by nearest-neighbor routing. In the ocean, meltwater is distributed over the upper 30 m (Sun et al., 2017). Solid ice discharge (i.e., calving) is also routed to the nearest ocean neighbor, but is spread diffusively in the ocean surface layer over a region extending up to 300 km from the coast, and is melted instantaneously using energy from the ocean surface. Ocean thermal forcing to calving fronts is not simulated. Greenland's floating ice shelves, such as Petermann, are not simulated, and thus the basal melt term refers only to grounded ice. This term is small compared to mass loss from surface runoff and calving, and is disregarded in the remaining discussion.

Dynamic land units in CLM5 enable the transition from glaciated to non-glaciated land cover, consistent with the evolving ice sheet margin in CISM2. The ice sheet surface topography in CISM2 is used to recompute the glacier coverage in CLM5 at runtime, modifying the albedo, soil, and vegetation characteristics. Surface elevation and topographic roughness fields in CAM6 are updated every 10 years to incorporate ice-sheet geometry changes in atmospheric calculations. The coupling is further described in Chapter 2.

3.2.3 Experimental Set-Up

We analyze two simulations: a historical run from 1850 to 2014, and its continuation to 2100 following the SSP5-8.5 scenario (Nowicki et al., 2016; O'Neill et al., 2016). The historical forcing is a reconstruction based on observations of greenhouse gas concentrations, stratospheric aerosol data (volcanoes), land use change, and solar insolation. The pre-industrial (1850 CE) CO_2 concentration is 287 ppmv, increasing to 397 ppmv in 2014. Further details on the forcing protocol can be found in Eyring et al. (2016). The SSP5-8.5 scenario starts in 2015 at the end of the historical period, and ends in 2100 when the atmospheric CO_2 concentration is 1142 ppmv and the radiative forcing is +8.5 W m^{-2} relative to pre-industrial.

3.2.4 Initialization/spin-up procedure

The coupled model is initialized with a ∼10,000 year pre-industrial steady state simulation with CESM2-CISM2, of which the procedure is detailed below. A fully synchronously coupled spin-up with CESM2-CISM2 is not feasible due to the high computation cost of the model, mainly of the atmosphere component. An efficient procedure has been designed to perform the model spin-up.

In this procedure, two model configurations are alternated, where one demands less computational resources than the other. The first configuration uses the computationally expensive, fully coupled model with all components active (so-called *BG*

configuration). The second uses a data-atmosphere model. In this configuration, all other components are active (so-called *JG* configuration). The JG uses the atmosphere forcing generated in the preceding fully coupled BG segment. Furthermore, the ice sheet dynamics are accelerated by a factor of ten in the JG configuration. This is needed to initialize the thermal structure of the ice sheet.

For the ice sheet model initialization, the present-day observed Greenland Ice Sheet geometry and bedrock Morlighem et al. (2014) were combined with a Holocene internal temperature structure Fyke et al. (2014a). All other model components are initialized from a pre-industrial steady state simulation with a pre-release CESM2.0 version. During the spin-up, the external forcing is kept constant at the pre-industrial (1850) atmospheric CO_2 concentration (284 ppmv) and the orbital parameters are fixed.

The spin-up started with a BG segment of 35 years. From the end state of the first BG segment, a 150-year JG segment started. The JG segments use the last 30 years of the preceding BG as a data-atmosphere forcing, cycling though it 5 times. A combined BG segment + JG segment with the same atmospheric climate result in the simulation of 35 atmosphere years; 185 ($35 + 5 \times 30$) ocean, land, sea-ice years; and 1535 ($35 + 5 \times 300$)) ice sheet years. After this, the atmosphere surface elevation is updated with the evolved ice sheet topography taken from the ice sheet model CISM2, using the NCAR global model topography generation software Lauritzen et al. (2015). Then a new 35-year BG segment started.

This procedure of BG+JG and topographic updating was repeated six times. The simulation ended with an additional 100–year BG segment. At the end of the simulation a near-equilibrium state was reached after 310 simulated atmosphere model years; 1210 land, ocean, and sea-ice model years; and 9310 ice sheet model year. The computational expense of this spin-up is about 7% of a fully synchronous CESM2-CISM2 spin-up of the same length.

The initial condition of the historical simulation is the spun-up model state. At the beginning of our simulation, the GrIS is in near-equilibrium with the simulated pre-industrial climate of CESM2, with residual drift of about 0.03 mm SLE yr^{-1}. This initial GrIS overestimates the present-day observed area and volume by about 15% and 12%, respectively.

3.2.5 Basin-Scale Analysis

For regional-scale analysis, we use six major Greenland drainage basins defined by Rignot and Mouginot (2012). The basins are directly remapped onto the CISM grid since the modeled drainage divide locations roughly agree with observations (see velocity fields of Figure 3.3a, showing observations from Joughin et al. (2010, 2015), and 3.3b, and ice discharge per drainage basin in Table 3.3). In regions where the ice sheet extent is overestimated, drainage basins are extended to the ice sheet margin. By extending each drainage basin from the margin into the ocean based on the ice flow direction, we also define six major ice–ocean sectors that receive freshwater from each basin.

3.3 Results

The analysis focuses on three climatological periods: the contemporary period (average over 1995–2014) from the historical simulation, and the mid-century (2031–2050) and end-of-century (2081–2100) from the SSP5-8.5 simulation.

3.3.1 Evolution of Global Climate and GrIS Mass Budget

The atmospheric CO_2 concentration increases from 287 ppmv in 1850, to 397 ppmv in 2014, 566 ppmv in 2050, and 1142 ppmv in 2100 (Figure 3.1, Table 3.1). The simulated end-of-century global mean near-surface temperatures increase is 5.4 K relative to pre-industrial. With respect to the contemporary period (1995–2014), the simulated global temperature increases by 1.4 K at mid-century and by 4.6 K at end-of-century. The Arctic Amplification (AA) factor, defined as the ratio of temperature change north of 60°N to the global mean, is 2.0 by mid-century and 1.8 by end-of-century. The decrease in AA between mid- and end-of-century is significant ($p < 0.01$) and is likely the result of reduced sea ice cover, since AA depends on the magnitude of sea ice change (e.g., Dai et al. (2019)). At mid-century, sea ice concentration is still declining throughout the year, while at end-of-century, the Arctic is ice-free in late summer and early fall and thus experiences no further loss.

Table 3.1: Carbon dioxide forcing, global mean temperature change w.r.t. pre-industrial, GrIS contribution to sea level rise and partition into components, and GrIS area for contemporary, mid-century and end-of-the-century periods. The mean [standard deviations] are given over the time period indicated in header, except for the atmospheric CO_2 concentration, the cumulative sea level rise and the GrIS area, which are given for the end and/or start year of the time segment. GrIS Mass Balance = Surface Mass Balance – Ice Discharge - Basal Melt. Cumulative sea level rise corresponds to the periods 1850-2014 for "Contemporary", 1850-2050 for "Mid-century", and 1850-2100 for "End of century". Mass Balance and Sea Level Rise rate relate by 360 Gt yr^{-1} = 1 mm yr^{-1}.

	Contemporary (1995-2014)	Mid-century (2031-2050)	End of century (2081-2100)
Atmospheric CO_2 (ppmv)			
start of time segment	361	458	884
end of time segment	397	566	1142
Global mean T2m change (K)	0.8	2.2	5.4
Cumulative SLR (mm)			
end of time segment	5	23	109
SLR rate (mm yr^{-1})	0.08	0.55	2.68
Mass Balance (Gt yr^{-1})	-27 [81]	-196 [71]	-964 [258]
SMB (Gt yr^{-1})	564 [82]	350 [75]	-565 [278]
Ice discharge (Gt yr^{-1})	568 [4]	523 [10]	379 [24]
Basal melt (Gt yr^{-1})	24 [0]	23 [0]	20 [0]
GrIS area (10^6 km^2)			
end of time segment	1.965	1.958	1.909

The simulated North Atlantic Meridional Overturning Circulation (NAMOC) (defined as the maximum of the overturning stream function north of 28°N and below 500 m depth in the North Atlantic basin) is relatively stable during the historical period, with a mean of 24 Sv (blue line in Fig. 3.1b). The only exception is an anomalously stronger overturning circulation in the 1960s, when the NAMOC increases by about 3 Sv. RAPID-AMOC measurements at 26°N in the Atlantic basin give a mean overturning strength of 17 ± 3.3 Sv for 2000–2018 (Frajka-Williams et al., 2019), in good agreement with the simulated value (18.7 ± 2.4 Sv) at this latitude over the same period. During the 21st century, the simulated overturning cell progressively weakens, collapsing to 8.6 Sv by end-of-century (Table 3.2).

Table 3.2: Comparison of mean [standard deviations] of surface mass balance (Gt yr^{-1}, upper half of the table) and NAMOC index (Sv, lower half of the table) for CESM2-CISM2 (results of this study) and ensemble of CESM2 simulations with prescribed-surface-elevation, non-dynamical Greenland ice sheet (that is, with non-active CISM2) for historical and several SSP scenarios (simulations contributing to CMIP6).

	#	Historical (1850-2014)	Contemporary (1995-2014)	Mid-century (2031-2050)	End of century (2080-2099)
SMB					
CESM2-CISM2					
- Historical	1	588 [90]	571 [80]		
- SSP5-8.5	1			359 [84]	-511 [283]
CESM2					
- Historical	11	455 [39]	390 [28]		
- SSP1-2.6	2			252 [65]	88 [97]
- SSP2-4.5	3			267 [58]	21 [80]
- SSP3-7.0	2			227 [76]	-269 [106]
- SSP5-8.5	2			192 [90]	-906 [307]
NAMOC					
CESM2-CISM2					
- Historical	1	24.0 [1.0]	23.8 [0.7]		
- SSP5-8.5	1			18.2 [1.4]	8.6 [1.5]
CESM2					
- Historical	11	23.8 [0.9]	23.8 [0.9]		
- SSP1-2.6	2			18.1 [1.5]	11.6 [0.6]
- SSP2-4.5	3			17.9 [1.4]	10.4 [0.8]
- SSP3-7.0	2			19.1 [1.1]	12.0 [1.1]
- SSP5-8.5	2			18.8 [1.5]	8.6 [1.3]

The simulated climate change drives a positive GrIS contribution to global mean SLR (Figure 3.1c). The rate of mass loss increases from the pre-industrial near-equilibrium (0.03 mm SLE yr^{-1}) to 0.08 mm SLE yr^{-1} during the contemporary period, 0.55 mm SLE yr^{-1} by mid-century, and 2.68 mm SLE yr^{-1} by end-of-century (Table 3.1). The associated SLR is 23 mm SLE by 2050 and 109 mm SLE by 2100.
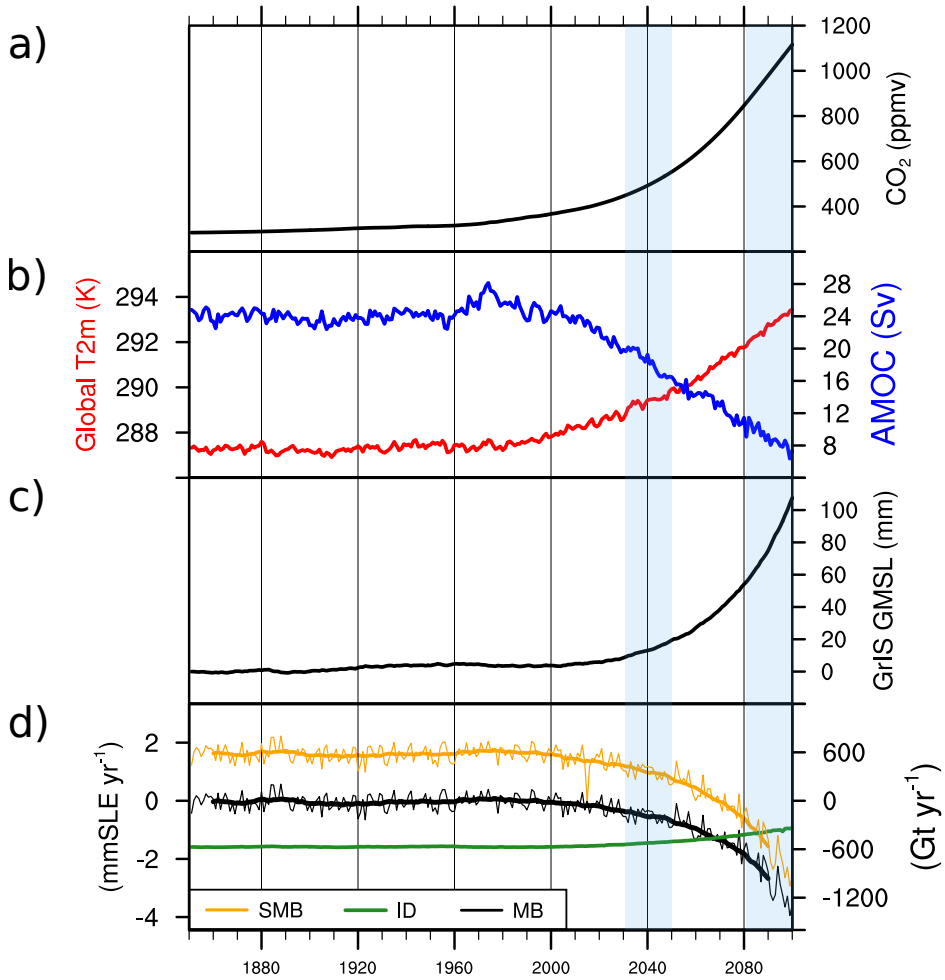
Figure 3.1: CESM2-CISM2 1850-2100 evolution of (a) CO_2 forcing; (b) global mean temperature (K) and NAMOC index (Sv); (c) cumulative Greenland contribution to global mean sea level rise; and (d) Mass Balance (MB) contribution to global mean sea level rise and components of the mass budget (SMB, Ice Discharge) with right axis: Gt yr^{-1}, left axis: mm yr^{-1} . The blue-shaded areas denote the mid-century (2031-2050, left), and end-of-century (2081-2100, right) periods.

Estimates of 2003–2013 Greenland mass loss from the Gravity Recovery and Climate Experiment (GRACE) satellite mission range from 0.77 to 0.79 mm SLE yr^{-1} (Velicogna et al., 2014; Schrama et al., 2014; Ran et al., 2018). The simulated SLR in the contemporary period is underestimated, likely for several reasons. First, a substantial part of the observed mass loss is attributed to ocean forcing (Wood et al., 2018), which is missing in the model. Second, anomalous atmospheric circulation, in particular blocking over Greenland, has contributed to the observed mass loss but is not simulated correspondingly in global climate models (Delhasse et al., 2018; Hanna et al., 2018). Other model biases (e.g., initial ice sheet topography) can ex-

plain the remaining differences. The temperature change at the time of mass loss acceleration is approximately 2.7 K with respect to pre-industrial. By 2100, the simulated GrIS area and volume decrease by 3% and 1.2%, respectively, compared to the pre-industrial ice sheet.

The SMB is the main contributor to GrIS mass loss (Figure 3.1d, Table 3.1). By mid-century, the GrIS-integrated SMB is still positive (350 Gt yr^{-1}), and 214 Gt yr^{-1} lower than in the contemporary period. Based on a linear, long-term trend, the integrated SMB becomes negative by 2077. The expansion of ablation areas (i.e., areas with average SMB < 0) accelerates with similar timing. By mid-century, the SMB is strongly reduced in southern Greenland (Figure 3.2), and by end-of-century, the ablation areas extend far inland around the entire ice sheet, including the northern periphery. At the northern margins, the ablation zone advances later, and progresses faster inland, than at the southern margins. By end-of-century the northern surface mass loss also has intensified. In the ice sheet interior, the SMB moderately increases due to greater snowfall.

As the SMB becomes more negative, the ice sheet thins (Figure 3.2,b-c). Most of the thinning occurs in the south and below the 2000-m elevation contour, while the ice sheet interior moderately thickens (Figure 3.2,e-f). Surface velocities increase in the intermediate areas between the high interior and the ice sheet margins (Figure 3.2,h-i) where the surface is steeper because of SMB-induced margin thinning. Conversely, surface velocities decrease at the thinner margins. As a result, total ice discharge is reduced by 8% (45 Gt yr^{-1}) at mid-century and by 33% (189 Gt yr^{-1}) at end-of-century compared to the contemporary period (Table 3.1 and Figure 3.3). The reduced discharge partly compensates for the mass loss due to more negative SMB (214 Gt yr^{-1} and 1129 Gt yr^{-1} at mid-century and end-of-century, respectively; see Table 3.1).

3.3.2   Sea Level Rise Contribution by Drainage Basin

This section presents mid-century and end-of-century mass balance changes for individual drainage basins, with the contemporary mass budget as a reference (Figure 3.5). The simulated ice discharge for the integrated GrIS and for the SE basin is in reasonable agreement with observations (Enderlin et al. (2014), Table 3.3). Regions with ice discharge overestimation (SW, NE and NO) correspond with regions of ice thickness overestimation, and vice versa (NW, CW).

By mid-century, the mean total GrIS mass loss is 169 Gt yr^{-1} (Figure 3.4), as the result of an SMB decrease partly offset by reduced ice discharge. In all six drainage basins the SMB decreases but remains positive (Figure 3.5), with the largest reductions in the SW (66 Gt yr^{-1}) and SE (80 Gt yr^{-1}), There is a modest mid-century decrease in the NE basin (32 Gt yr^{-1}), with smaller reductions in the CW, NW and NO basins. Taken together, the SMB in the northern basins (NO, NW, NE) decreases by 55 Gt yr^{-1}, or about 26% of the six-basin total.

At the end of the century (right panel in Figure 3.4), the mean mass budget of the GrIS has decreased by 935 Gt yr^{-1} compared to the contemporary budget,
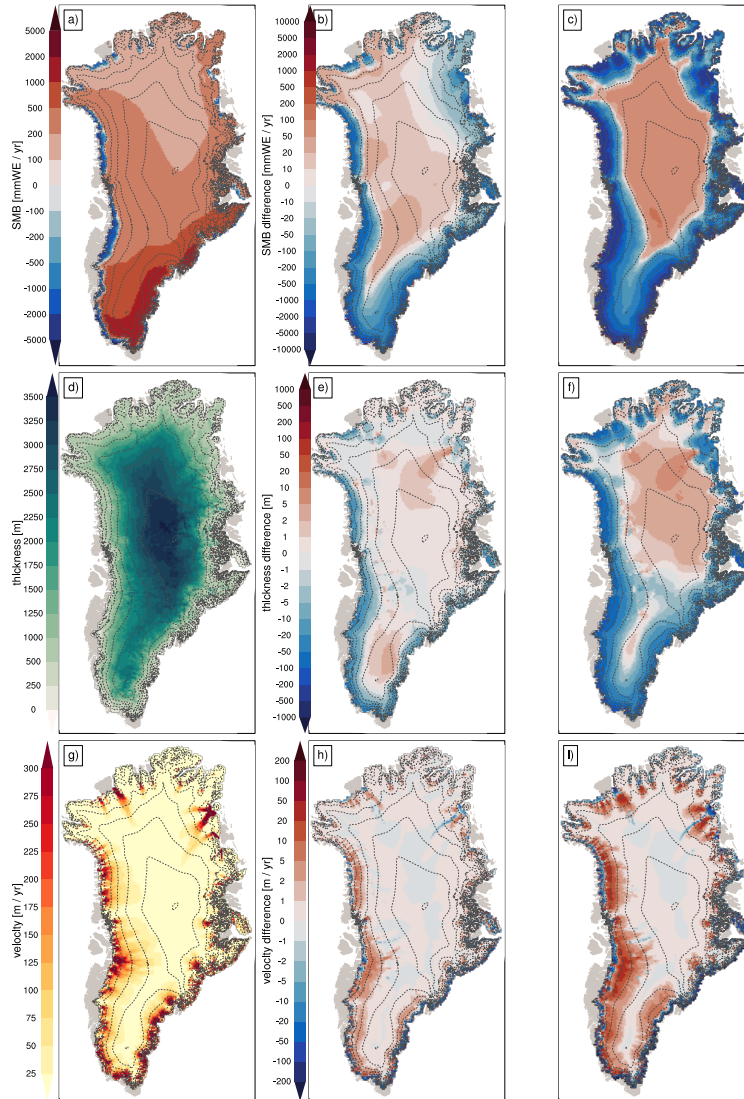
Figure 3.2: Change in SMB (kg m^{-2} yr^{-1}), ice thickness (m), and surface velocities (m yr^{-1}), by mid-century (middle) and end-of-century (right) with respect to the contemporary period (1995-2014, left, absolute values).

and the total surface mass balance is reduced by 1129 Gt yr^{-1}. The mass loss from ice discharge is reduced by 189 Gt yr^{-1}, partly (17%) cancelling the surface mass loss. The largest end-of-century decreases in SMB (290 Gt yr^{-1}) and ice discharge (81 Gt yr^{-1}) are in the SE basin, which make the second largest SLR contribution (215 Gt yr^{-1}; right panel in Figure 3.5). The SW basin, with the next largest SMB decrease (272 Gt yr^{-1}) and a smaller reduction in discharge (27 Gt yr^{-1}), is the largest net contributor to SLR (235 Gt yr^{-1}). The three northern basins also have large SMB decreases: 203, 145, and 141 Gt yr^{-1}, respectively, for the NE, NO, and
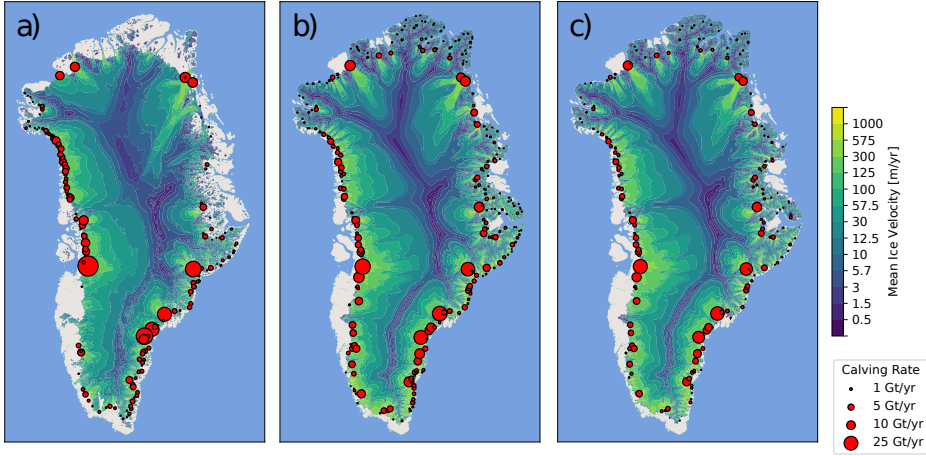
Figure 3.3: Maps of ice discharge (circles, Gt yr^{-1}) and surface velocity (background contours; m yr^{-1}) from: a) observations (2000-2006 ice discharge from Enderlin et al. (2014) and surface velocity from Joughin et al. (2010, 2015), b) model historical period (2000-2006), and c) model end of SSP5-8.5 (2081-2100).

Table 3.3: Average ice discharge (Gt yr^{-1}) for the GrIS, and per drainage basin, from observations over the period 2000-2005 Enderlin et al. (2014) and from the CESM2-CISM2 simulation over the same time period.

	Observed	Simulated
GrIS	510	569
NW	101	59
CW	101	77
SW	23	71
SE	224	220
NE	41	99
NO	20	43

NW basins. Together, the northern basins contribute 43% of the total end-of-century SMB decrease and 45% of the total SLR.

3.3.3   Freshwater Fluxes

This section presents the mid-century and end-of-century freshwater fluxes to the ocean from individual drainage basins (Figure 3.6). The change in total freshwater fluxes is moderate at mid-century, with runoff increasing by less than 200 Gt yr^{-1} (from 427 to 619 Gt yr^{-1}), and a small decrease in the solid flux (i.e., ice discharge), from 481 to 430 Gt yr^{-1} (Figure 3.6). By this time, the NAMOC has already decreased by 6 Sv (Figure 3.1), suggesting that increased Greenland freshwater fluxes play only a minor role in weakening the NAMOC.

By end-of-century, runoff has more than tripled compared to the contemporary
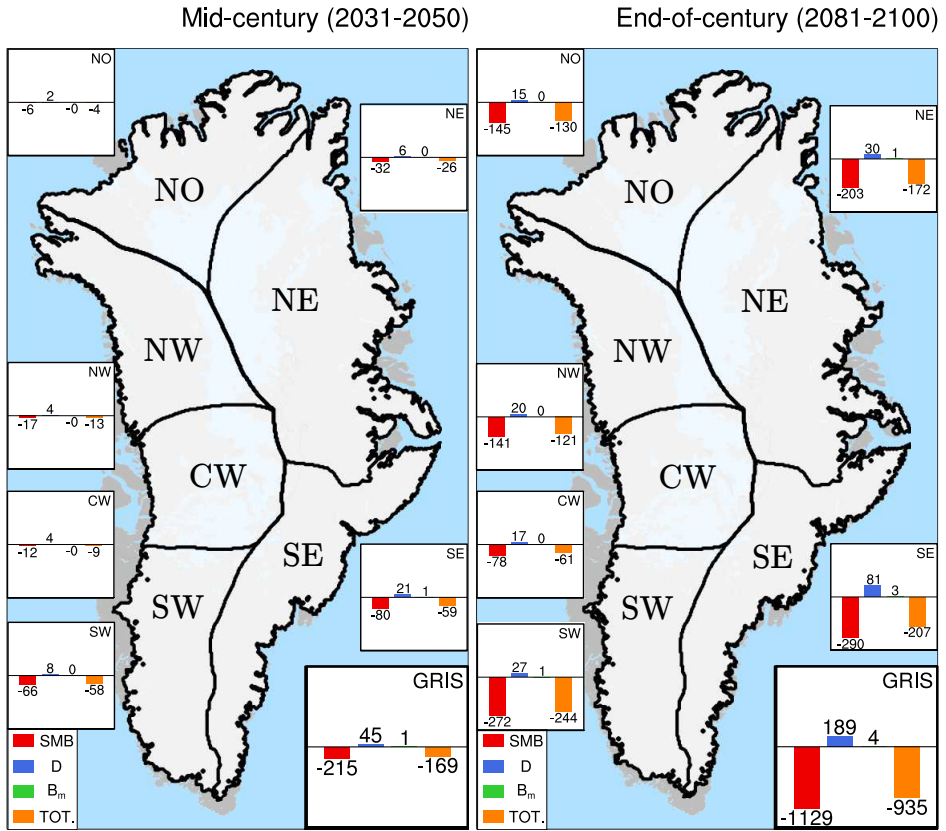
Figure 3.4: Change in GrIS mass balance (TOT) and components with respect to the contemporary budget (1995-2014) for mid-century (2031-2050, left), and end-of-century (2081-2100, right), in Gt yr^{-1}. GrIS mass balance (TOT; orange) = Surface mass balance (SMB; red) - Ice discharge (D; blue) - Basal melt (B$_m$; green). Note that Ice discharge and Basal melt are defined negative here for graphical purposes.

period, increasing to 1445 Gt yr^{-1} (Figure 3.6). The reduced ice discharge (260 Gt yr^{-1}) results in a total freshwater flux that is not quite double the contemporary flux (1705 Gt yr^{-1} compared to 908). Per basin, the SW and SE regions contribute the most to the total runoff during all periods. However, their relative contribution decreases from 63% in the contemporary period to 48% at end-of-century. Thanks to a large increase in runoff, the relative freshwater contribution from the northern basins (NW, NE, and NO) increases from 29% in the contemporary period to 44% at end-of-century.

Throughout the simulation, the SE region has the largest GrIS ice discharge in absolute terms (Figure 3.6). Relative to the contemporary discharge, all basins have similar reductions of around 10% at mid-century, but by end-of-century the northern basins have the greatest reductions (62%).
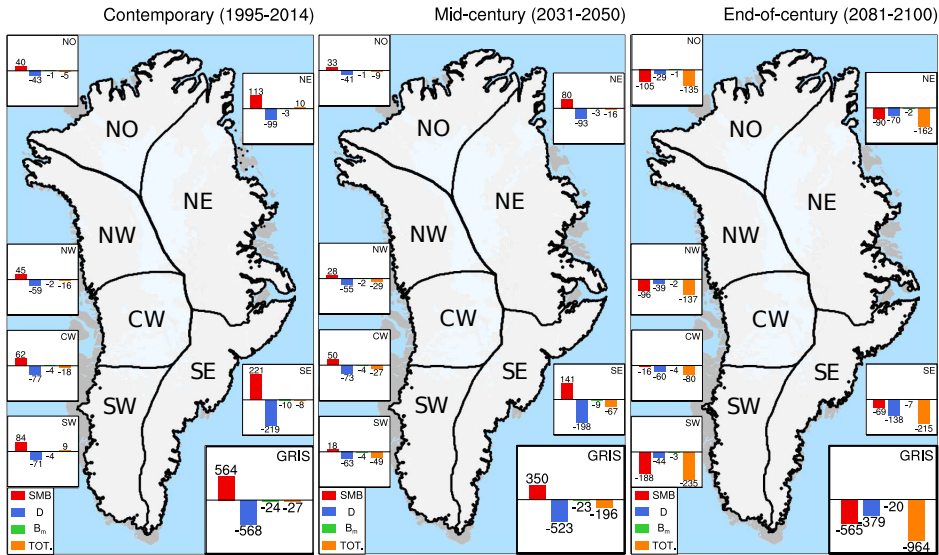
Figure 3.5: Mass balance (TOT) and components for the Greenland Ice Sheet and individual basins (NO, NE, SE, SW, CW, NW, NO) in the last 30 years of the historical simulation (contemporary period, 1995-2014). Right panel: same as in the left panel, with values expressed as anomalies to the PI-control simulation. GrIS mass balance (TOT; orange) = Surface mass balance (SMB; red) - Ice discharge (D; blue) - Basal melt (B_m; green). Note that Ice discharge and Basal melt are defined negative here for graphical purposes.

3.3.4 Comparison to CESM2 Simulations without an Interactive Greenland Ice Sheet

Finally, we compare the SMB and NAMOC responses to the historical ensembles and a suite of scenario simulations conducted using CESM2 without an interactive GrIS, but with the same SEB-based SMB calculation. We consider 11 ensemble members from the historical period, and the following scenario simulations between 2015-2100: SSP1-2.6 (2 members), SSP2-4.5 (3 members), SSP3-7.0 (2 members), and SSP5-8.5 (2 members), with scenario details provided by O'Neill et al. (2016).

Compared to CESM2-CISM2, the CESM2 simulations have a lower contemporary and end-of-century SMB, and a greater SMB sensitivity to warming (Figure 3.7 and Table 3.2). Also, the reduction in SMB between the full historical mean [1850-2014] and the contemporary mean [1995-2014] is larger in CESM2 (65 Gt yr^{-1}, from 455 to 390 Gt yr^{-1}) than in CESM2-CISM2 (17 Gt yr^{-1}, from 588 to 571 Gt yr^{-1}). The contemporary CESM2-CISM2 overestimates the SMB (Noël et al., 2018), Also, there is higher interannual SMB variability than CESM2 (80 Gt yr^{-1} vs. 28 Gt yr^{-1}, Table 3.2). These differences are, at least in part, because the SMB is calculated over a different ice sheet topography. CESM2 simulates a realistic SMB for the contemporary period (Noël et al., 2019).

At end-of-century under SSP5-8.5 forcing, the SMB is almost 400 Gt yr^{-1} lower in CESM2 compared to CESM2-CISM2 (-906 vs -511 Gt yr^{-1}). The smaller SMB
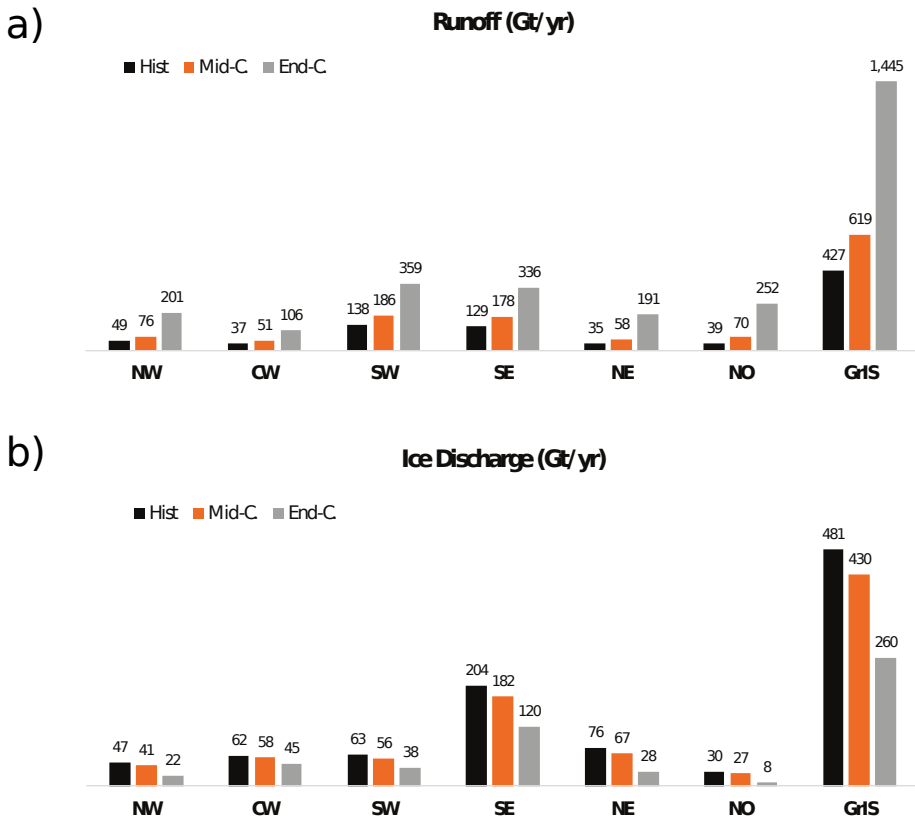
Figure 3.6: Freshwater flux (Gt yr^{-1}) from (a) Greenland runoff and (b) ice discharge per basin for the contemporary, mid-century and end-of-century periods.

reduction in CESM2-CISM2 is likely the result of dynamic removal of high-melt areas on the margins. These areas are allowed to remain in the non-evolving CESM2 simulation, favoring an overestimate of SMB decline. The CESM2-CISM2 response to SSP5-8.5 does, however, exceeds the CESM2 response to less extreme scenarios, including SSP3-7.0. Despite the differences in SMB magnitude, the timing of SMB evolution in the two models is similar for SSP5-8.5.

NAMOC evolution also is similar in CESM2-CISM2 and CESM2 simulations (Figure 3.7 and Table 3.2). The peak NAMOC strength in the second half of the 20th century, mentioned in section 3.3.1, is present in both simulations. Generally, the NAMOC in CESM2 is sensitive to external forcing in the 21st century, with large reductions in all scenarios including SSP1-2.6. In the SSP5-8.5 projections, there is no discernible differences in NAMOC weakening between simulations with and without dynamical GrIS.
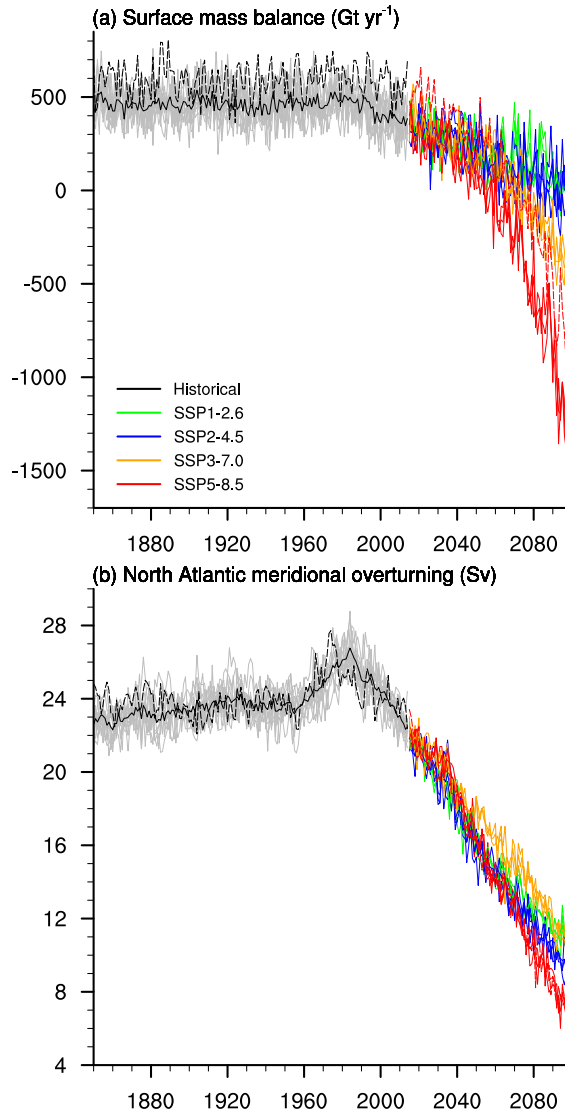
Figure 3.7: Comparison of evolution of a) SMB (Gt yr^{-1}) and b) NAMOC index (Sv) for the historical (black, dashed) and SSP5-8.5 (red, dashed) coupled simulations in this paper versus CESM2 historical (black, solid) and scenario simulations (solid) with a prescribed-surface-elevation, non-dynamical Greenland ice sheet (that is, with non-evolving CISM2). Thick lines represent CESM2 scenario-ensemble means.

3.4 Discussion and Conclusions

This study presents the first simulations performed with CESM2-CISM2 including an interactive Greenland Ice Sheet. The projected GrIS contribution to SLR by 2100 in the SSP5-8.5 scenario is 109 mm, in general agreement with pre-AR5 multi-model results (Bindschadler et al., 2013) and the AR5 (Church et al., 2013). The latter gives

a likely range of 70 to 210 mm. Our projection also lies within the range of post-AR5 estimates from Fürst et al. (2015), Calov et al. (2018), and Golledge et al. (2019), which are of 102 ± 32 mm, 46–130 mm, and 112 mm, respectively. Vizcaino et al. (2015) gave a lower estimate (58 mm), based on a coupled Earth system/ice sheet model of coarse resolution (3.75°) with an energy-balance-based melt calculation. Aschwanden et al. (2019) estimated a higher range of 140–330 mm, using an ice sheet model forced with spatially uniform warming. In our projection, the negative SMB trend increases sharply at mid-century, so that most of the SLR contribution is after 2050.

This study projects an increased contribution of the northern basins to total GrIS mass loss after mid-century, in agreement with previous studies. Noël et al. (2019) found a 46% expansion of ablation area in northern Greenland between the early 1990s and 2017, almost twice as much as in the south, because runoff in the north and northeast increased relative to the total runoff due to longer exposure of bare ice. The high response in the north is also explained by the relatively wide ablation zones from low surface slopes (Van den Broeke et al., 2016). In 21st century RCP4.5 and RCP8.5 projections with the regional climate model MAR with static GrIS topography, Tedesco and Fettweis (2012) also found a high sensitivity of SMB to higher temperatures in the north. Similarly, Lenaerts et al. (2015), in a 21st century RCP4.5 projection with the regional climate model RACMO, projected a strongly nonlinear response of runoff in northern and northeastern Greenland, in connection with low meltwater buffering capacity of the snow pack.

Chapter 4

Accelerated Greenland ice sheet mass loss under high greenhouse gas forcing as simulated by the coupled CESM2–CISM2

Vaak kwam het zo ver, werd de
meteorologiese brutaliteit tot zulke toppen
gedreven, dat de eerste sneeuw niet meer viel
in de winter of de herfst, niet meer in de
nazomer of het begin van de zomer zelfs,
maar nog vroeger, in de lente, op het eind van
de vorige winter, en steeds maar vroeger, jaren
te vroeg op den duur

Gust Gils *Berichten om bestwil*

The Greenland Ice Sheet is now losing mass at a rate of 0.7 mm of sea level equivalent per year. Here we explore the Greenland Ice Sheet evolution and interactions with global and regional climate under high greenhouse gas forcing with the Community Earth System Model version 2, which includes an interactive ice-sheet component (the Community Ice Sheet Model version 2) and an advanced energy-balance-based calculation of surface melt. We run an idealized 350-year scenario in which atmospheric CO_2 concentration increases by 1% annually until reaching four times pre-industrial values at year 140, after which it is held fixed. The global mean temperature increases by 5.2 K and 8.5 K by years 131–150 and 331–350, respectively. The projected Greenland Ice Sheet contribution to global mean sea level rise is 107 mm by year 150, and 1140 mm by year 350. The rate increases from 2 mm yr^{-1} at year 150 to almost 7 mm yr^{-1} by year 350. The accelerated mass loss is caused by rapidly increasing surface melt as the ablation area expands, with associated albedo feedback and increased sensible and latent heat fluxes. This acceleration occurs for a global warming of approximately 4.2 K with respect to pre-industrial. It is in part explained by the quasi-parabolic shape of the ice sheet, which favors rapid expansion of the ablation area as the equilibrium line altitude approaches the interior "plateau".

4.1   Introduction

This chapter presents the results of a multicentury (350-year) simulation of global climate and Greenland Ice Sheet (GrIS) evolution in an idealized scenario. Atmospheric CO_2 increases by 1% annually to four times the pre-industrial value and is kept fixed then at this high concentration for the remainder of the simulation. The goal is to investigate multicentury GrIS mass loss with a focus on ice sheet/climate interactions and feedbacks. We assess the timing and magnitude of the GrIS response in relation to global climate change, and the relative importance of the processes that govern GrIS behaviour. We also investigate nonlinearities in the response to the forcing and apparent accelerations in the GrIS contribution to sea level rise (SLR).

Section 4.2 describes the coupled model and the experimental setup. The main results are discussed in section 4.3, which includes subsections on (1) overall global climate change, (2) GrIS and drainage basins mass changes, (3) ice sheet dynamics, (4) spatial analysis of the surface mass balance and (5) spatial analysis of the surface energy balance. Section 4.4 contains the discussion and conclusions.

4.2   Method

4.2.1   Model description

Model simulations were carried out with Community Earth System Model version 2 (CESM2) (Danabasoglu et al., 2020), a fully coupled, global Earth System Model (ESM) with prognostic components of the atmosphere, ocean, land, sea ice, and land ice. CESM2 is one of the models contributing to the Coupled Model Intercomparison

Project phase 6 (CMIP6) (Eyring et al., 2016) and the Ice Sheet Model Intercomparison Project for CMIP6 (ISMIP6) (Nowicki et al., 2016). The atmosphere is simulated with the Community Atmosphere Model version 6 (CAM6), using the Finite Volume dynamical core (Lin and Rood (1997); Gettelman et al. (2019)), on a nominal 1-degree horizontal grid with 32 vertical levels. The ocean component is the Parallel Ocean Program version 2 (POP2) (Smith et al., 2010), which runs on a nominal 1deg displaced-pole grid with 60 vertical levels. Sea ice is represented by the Los Alamos National Laboratory sea ice model version 5 (CICE5) (Hunke et al., 2017), which runs on the same horizontal grid as POP2. Land processes are simulated by the Community Land Model version 5 (CLM5) (Lawrence et al., 2019), which runs on the same horizontal grid as CAM6. The CLM5 snow pack includes up to 10 vertical layers with a maximum total depth of 10 m water equivalent (WE). CLM5 further includes the Model for Scale Adaptive River Transport (MOSART) to handle land surface runoff based on topographic gradients.

The GrIS is simulated using the Community Ice Sheet Model version 2 (CISM2) (Lipscomb et al., 2019) on a 4-km rectangular grid with 11 terrain-following vertical levels. The velocity solver uses a depth-integrated higher-order approximation (Goldberg, 2011) of the Stokes equations for ice flow. A pseudo-plastic sliding law and a simple basal hydrology model as described by Aschwanden et al. (2016) is used to parameterize basal sliding. In this scheme, the yield stress is determined by the till friction angle and the effective pressure. The former depends on the bedrock elevation via a fixed piecewise linear relationship. The bedrock evolves due to glacial isostatic adjustment according to an Elastic Lithosphere Relaxing Asthenosphere (ELRA) model. Calving in this study is parameterized with a flotation criterion, whereby floating ice is discharged instantaneously to the ocean.

4.2.2 Model Evaluation without interactive GrIS

To place the analysis in this section in the context of model skill, the main findings of the CESM2 non-evolving Greenland present-day climate evaluation study of van Kampenhout et al. (2020) are summarized here and in Table 4.1. The study uses an ensemble of six historical simulations (1850-2014) with non-evolving GrIS of present-day observed geometry. The CESM2 climatological mean of the reference period 1961-1990 is taken and compared with a suite of benchmark products: reanalyses, satellite observations, and polar regional climate model RACMO simulation.

van Kampenhout et al. (2020) generally conclude that CESM2 simulates the Greenland climate reasonably well in terms of large-scale dynamics, cloud properties, Surface Mass Balance (SMB) and Surface Energy Balance (SEB). The CESM2 SMB is overestimated by 60 Gt yr^{-1}. This is mainly due to the overestimation of precipitation in CESM2 compared with RACMO (Table 4.1). The area of the ablation zones in the north and east is underestimated. SEB-related biases in CESM2 with respect to RACMO includes a low snow albedo: the GrIS integrated annual-mean albedo in CESM2 deviates from that in RACMO with -0.049. A larger amount of shortwave radiation is absorbed in CESM2 and the summer net radiation (R_{net}) is generally

larger too, particularly at lower elevations. On the other hand, CESM2 simulates weaker non-radiative fluxes than RACMO. In sum, the summer melt energy is similar. Regarding clouds: van Kampenhout et al. (2020) note that the annual mean GrIS-average cloud liquid water path (LWP) in CESM2 is 29.9 g m^{-2} versus 20.2 g m^{-2} in satellite data from CloudSat-CALIPSO. The overestimation is located particularly in the south of the ice sheet. The CESM2 bias in the LWP is relevant in the context of SEB analysis, due to the sensitivity of longwave radiation for liquid water in the atmosphere.

Table 4.1: Overview of GrIS-integrated SMB components from CESM2 without evolving GrIS and RACMO2.3p2, for the period 1961-1990, as computed by from van Kampenhout et al. (2020).

Mean mass flux (Gt yr^{-1})	RACMO2.3p2 1961-1990	CESM2-static 1961-1990
Area GrIS (km^2)	1693317	1699077
Snowfall	642 [70]	705 [67]
Rain	19 [5]	59 [14]
Sublimation	30 [2]	32 [3]
Melt	324 [54]	367 [74]
Refreezing	157 [21]	198 [41]
Runoff	184 [41]	224 [45]
SMB	447 [99]	508 [73]
Ablation area (%)	8.0	7.5

4.2.3 Coupling Description

In the default CESM2 configuration, ice sheets do not evolve, but the simulations described here with CESM2-CISM2 have a dynamic GrIS that is interactively coupled to other Earth system components. The model features an SMB calculation with a surface-energy-balance calculation of melt. The SMB is defined as:

$$\text{SMB} = Precipitation - Runoff - Sublimation, \tag{4.1}$$

Precipitation is the sum of snowfall and rain. While snowfall contributes directly and positively to the SMB, rainfall only does so if it refreezes in the snow pack. If not, it runs off. The SMB can therefore be reformulated as:

$$\text{SMB} = Snowfall + Refreezing - Sublimation - Melt. \tag{4.2}$$

melt energy (E_M) is calculated from the surface energy balance:

$$E_M = SW_{net} + LW_{net} + LHF + SHF + GHF \tag{4.3}$$

with the available melt energy (E_M), the net shortwave radiation (SW_{net}), the net longwave radiation (LW_{net}), the latent heat flux (LHF), the sensible heat flux (SHF) and the ground heat flux (GHF).

The SMB is computed in CLM5 in multiple Elevation Classs (ECs). In this study (and by default), there are up to 10 ECs with fixed elevation ranges per glaciated grid cell (Lipscomb et al., 2013; Sellevold et al., 2019). The EC downscaling uses a fixed near-surface temperature lapse rate of $6\,K\,km^{-1}$, and specific humidity is downscaled assuming constant relative humidity with elevation. Rainfall is converted to snowfall when the near-surface temperature is lower than -2°C, and snowfall to rainfall when the near-surface temperature is higher than 0°C. In the case of snowfall-to-rainfall conversion, the resulting rainfall is routed directly to the ocean. The EC scheme features interactive coupling to CAM6 and explicit modelling of albedo, refreezing, and snow and firn compaction (Van Kampenhout et al., 2017; van Kampenhout et al., 2020). The SMB is then downscaled by the coupler to the higher-resolution CISM grid using a trilinear remapping scheme (bilinear in the horizontal and linear in the vertical), with corrections of accumulation and ablation to conserve global water mass.

The freshwater flux received by POP2 from the GrIS is the sum of surface runoff from CLM5, and basal melt and ice discharge from CISM2. These fluxes are supplied as salinity anomalies. Surface runoff is routed to the ocean via MOSART based on topographic gradients. These gradients are static; that is, they are not updated during the simulations to account for changes in the ice sheet topography. In the ocean, this flux together with basal melt from CISM2 is distributed by an estuary box model over the upper 30 m of the grid cell (Sun et al., 2017). Ice discharge as calculated by CISM2 is delivered to the nearest ocean grid cell and spread horizontally in the surface layer with a Gaussian distribution with a half-width radius of 300 km. This ice is melted instantaneously, with the corresponding latent heat removed from the ocean.

In CLM5, land surface types (known as land units) change dynamically from glaciated to vegetated as the ice sheet retreats, and vice versa when the ice sheet advances. The ice sheet surface topography from CISM2 is used to recompute the fractional glacier coverage in each CLM5 grid cell, modifying the albedo and soil and vegetation characteristics. The evolving ice-sheet topography is coupled offline, at regular intervals, to the atmosphere model, which enables orographic circulation feedbacks. For this study, mean surface elevation and sub-grid-scale surface roughness fields of CAM6 are updated every 10 model years based on CISM2 topography.

4.2.4   Experimental setup

We analyse two simulations: a 300-year control simulation of the pre-industrial era (year 1850 CE; Danabasoglu (2019b)) and a 350-year transient simulation with an idealized CO_2 scenario (Danabasoglu, 2019a). The atmospheric CO_2 concentration increases by 1% per year until reaching 1,140 ppmv, four times the pre-industrial value (hereafter 4xCO_2) in year 140 (Figure 4.1a). The 4xCO_2 level is maintained for the remaining 210 years. The purpose of this idealized scenario is to distinguish direct responses of climate and ice sheet from lagged responses and feedbacks without the effects of aerosol and land use changes that are included in the Shared Socio-

economic Pathway (SSP) scenarios. These simulations are part of ISMIP6. Further details on the forcing scenarios are provided by Eyring et al. (2016), and details on the experimental setup are provided by Nowicki et al. (2016).

Both simulations start from the spun-up pre-industrial Earth system/ice sheet state described by Lofverstrom et al. (2020)(the spin-up procedure is explained in more detail in Chapter 3.2.4). A near-equilibrium state was obtained by alternating between a fully coupled configuration with all model components active, and a more efficient partially coupled configuration with an inactive atmosphere model and the atmosphere data of the previous timeslice as forcing. After almost 10,000 years of ice sheet spin-up time, the residual drift in the near-equilibrated GrIS volume is 0.03 mm sea level equivalent (SLE) yr^{-1}, with GrIS volume and area overestimated by 12% and 15%, respectively, compared to present-day observations. The simulated pre-industrial ice sheet velocities and SMB compare reasonably well with present-day observations and regional modelling reconstructions. van Kampenhout et al. (2020) evaluated the SMB and Greenland climate in CESM2 simulations with GrIS topography fixed at observed present-day values, and Muntjewerf et al. (2020a) evaluated the simulated present-day ice discharge in CESM2 with evolving GrIS topography.

The analysis focuses on two main periods, broadly representative of one-century and multicentury change in the GrIS. We refer to years 131–150 (two decades around the time the model reaches $4xCO_2$) as "CO_2-stabilization", and to years 331–350 as "end-of-simulation". The CO_2-stabilization period has similar radiative forcing to the CMIP RCP8.5 and SSP5-8.5 scenarios at the end of the 21st century (Muntjewerf et al., 2020a; Vizcaino et al., 2015). The end-of-simulation period illustrates the multicentury GrIS response to elevated greenhouse gas forcing, comparable to year 2300 under high scenario forcing (e.g., Aschwanden et al. (2019); Vizcaino et al. (2015)). Both periods are indicated in Figure 4.1 by blue shading. The anthropogenic signal is considered to be emerged from natural background climate variability in the first long-lasting occurrence of the 20-year running mean value outside the two standard deviation range of the non-perturbed era, following the primary criterion in Fyke et al. (2014b).

4.2.5 Basin analysis

Six drainage basins have been used as defined by Rignot and Mouginot (2012). The basin delineation has been extended up to the simulated ice sheet margin where the simulated ice sheet area is larger than observed. These basins are referred to as north-west (NW), central-west (CW), south-west (SW), south-east (SE), north-east (NE), and north (NO); see Figure 4.2.

4.3 Results

4.3.1 Global climate change

The elevated CO_2 (Figure 4.1a) results in a top of the atmosphere (TOA) radiation imbalance (Figure 4.1b). The TOA imbalance increases until CO_2-stabilization and decreases thereafter. In response to the TOA imbalance, the global annual average near-surface temperature increases. The increase happens with an approximate constant rate in the first 140 model years, which results in a warming of 5.2 K (σ=0.3 K) at CO_2-stabilization (Figure 4.1c). In the next two centuries, the temperature increases by an additional 3.3 K as the ocean continues to warm. By end-of-simulation, the global warming trend decreases to 0.1 K decade^{-1}. The TOA imbalance decreases to about 2 W m^{-2}. This means the Earth system is not near an equilibrium at this stage, 200 years after CO_2-stabilization. A weak warming trend is expected if the simulation were to be continued, as it can take several millennia for the Earth system to reach a new equilibrium state (Rugenstein et al., 2020).

The near-surface temperature evolution in the Arctic (defined as north of 60°N) and on the GrIS follow a generally similar trajectory to the global mean. Arctic Amplification (AA), the ratio between Arctic and global mean temperature increase, is 1.6 (Figure 4.1c), with much of the signal originates from Arctic sea ice loss. GrIS amplification (the ratio of GrIS and global temperature increase) is about 1.2; it is smaller than the AA because the GrIS is a terrestrial region with a perennial ice/snow cover that holds the summer surface temperature near the melting point.

The greatest warming occurs in the Arctic basin, Canadian archipelago, and Antarctica; with annual mean changes of more than +18 K by end-of-simulation. The large warming in the high Arctic and Antarctic is largely connected with the decreasing sea ice cover. The Arctic becomes seasonally sea-ice free by the end of the first simulation century, and nearly completely ice free by year 270 with March sea-ice extent reaching below 2×10^6 km^2.

The North Atlantic Meridional Overturning Circulation (NAMOC) weakens significantly during the period of CO_2 increase. The NAMOC index – defined as the maximum overturning stream function north of 28°N and below 500 m – decreases at a rate of about 0.12 Sv yr^{-1} until year 140, and with 0.06 Sv yr^{-1} from year 140 to 170, to reach values below 6 Sv. The thickness of the upper, poleward-moving branch of the overturning cell diminishes. The location of the maximum overturning migrates equatorward and towards the surface. Significant NAMOC reduction and shallowing of the overturning cell in elevated CO_2 scenarios are common in CMIP6 ocean models, that generally simulate a greater NAMOC decline than the CMIP5 models (Weijer et al., 2020).

4.3.2 GrIS contribution to global mean sea level rise

The trajectory of mass loss in the 1% simulation can be separated into three distinct periods based on changes in time series trend. The GrIS responds slowly in the first
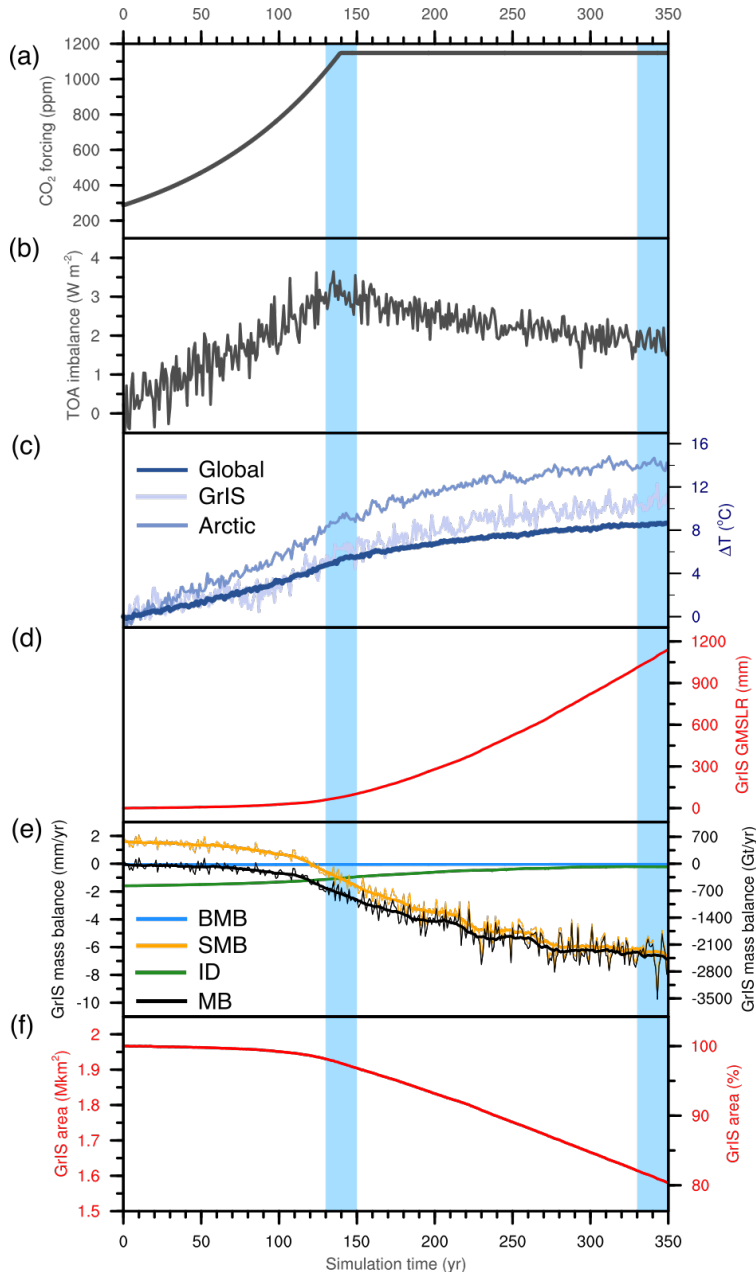
Figure 4.1: Evolution of (a) CO_2 (ppmv), (b) TOA radiation imbalance (W m^{-2}), (c) global, GrIS and Arctic region (north of 60°N) annual near-surface temperature anomaly with respect to pre-industrial mean (°C), (d) cumulative GrIS contribution to global mean sea level rise (mm SLE), (e) mass balance (MB, black) and components (SMB, orange; ice discharge (ID), green; basal mass balance (BMB), blue) (mm SLE yr^{-1} on left y-axis, and Gt yr^{-1} on the right y-axis), and (f) GrIS total area (left y-axis, million km^2) and percentage with respect to initial area (right y-axis). Ice discharge in BMB is defined as negative in (e) for visualization purposes.

period (years 1-119), and mass loss increases by 2.4 Gt yr^{-2}. The contemporary observed peak mass loss of 270 ±27 Gt yr^{-1} between 2007 and 2012 (0.75 mm SLE yr^{-1}, Shepherd et al. (2019)) is reached early in the second century of the simulation. The second period is the period of strongest mass loss acceleration. From year 120, the mass loss increases with 11.3 Gt yr^{-2} until year 225. At the start of this period, the global warming signal is 4.2 K. By CO_2-stabilization, early in this period of strong acceleration, the annual average SLR rate is over 2 mm yr^{-1} and the cumulative SLR is 107 mm (Table 4.2). The mass loss further increases in the third period but the acceleration slows down; during years 226–350 the mass loss increases with 4.6 Gt yr^{-2}. By end-of-simulation, after two centuries of sustained 4xCO_2 forcing, the annual average mass loss rate is ten times as large as at CO_2-stabilization. The total contribution to SLR is 1,140 mm by year 350. 19% of the ice sheet area is lost.

Table 4.2: Annual rate of GrIS mass loss (mm SLE yr^{-1}), cumulative GrIS mass loss (mm SLE), mass balance components (Gt yr^{-1}), and GrIS area (10^6 km^2). Mass Balance (MB) = Surface Mass Balance (SMB) – Ice Discharge (ID) + Basal Mass Balance (BMB). Three time periods are shown, corresponding to pre-industrial (years 1–300) and 1% simulations (years 131–150 and 331–350). Values are time-average [with standard deviation between square brackets if applicable].

	Pre-industrial	Years 131–150	Years 331–350
ANN mass loss	0.03 [0.23]	2.16 [0.47]	6.58 [1.04]
Cumulative mass loss	11	107	1,140
MB	-13 [84]	-764 [160]	-2,350 [358]
SMB	585 [85]	-367 [166]	-2,259 [357]
ID	574 [5]	378 [26]	77 [8]
BMB	-24 [0]	-19 [4]	-14 [0]
GrIS area	1.966	1.918	1.598

By the time of CO_2-stabilization, the SMB in all drainage basins is negative (Table 4.5). The largest reductions in SMB with respect to the pre-industrial are found in SE (-228 Gt yr^{-1}) and SW (-227 Gt yr^{-1}). The NE basin sees the third largest SMB loss (-171 Gt yr^{-1}). The smallest SMB losses are modelled in the CW, NO and NW basins, which together make of 34% of the total GrIS SMB reduction.

Total GrIS ice discharge diminishes by one-third of the pre-industrial value (-196 Gt yr^{-1}). The largest decrease is in the SE basin (37% less than in the pre-industrial), which is the basin with the largest initial calving flux. The ice discharge in the CW basin changes the least, with a decrease of 24% from the pre-industrial. From present-day remote sensing observations it is found that ice discharge increases since the 1980s, mostly driven by the retreat of glacier fronts, and with the largest speedup occurring in the NW and CW basins (King et al., 2020). Ocean thermal forcing to the outlet glacier is thought to be a driving mechanism. Comparing the projection to present-day observations, our model does not reproduce the increase in ice discharge, as it does not include ocean thermal forcing to the outlet glaciers. On the other hand, other modelling studies indicate a competition between enhanced ice discharge from glacier acceleration and decreased ice discharge from thinning due to surface mass loss (Goelzer et al., 2020).

The total basins mass change, like for the GrIS as a whole, is dominated by the SMB loss. The SW basin simulates the largest MB decrease (-198 Gt yr^{-1}), followed by the SE, NE, NW, NO and CW basins respectively. The largest contributor to the GrIS mass change at end-of-simulation is surface loss. The impact of surface loss is partially compensated by a reduction in ice discharge: the ice discharge flux at end-of-simulation is 497 Gt yr^{-1} smaller than in the pre-industrial simulation. The SW basin still has the largest surface mass loss. Where the NE was third at CO_2-stabilization, now it is the second largest but the NE now is second largest and SE have switched the NE and SE basins are second and third, respectively. The ice discharge flux further decreases all around the GrIS, ranging from -73% with respect to the pre-industrial in the NE basin up to -99% in the SW. This decreasing calving flux relates to the modelled margin thinning and retreat.

The mass loss rate at end-of-simulation increases in all basins compared to the CO_2-stabilization period, but the amount of the increases varies. The CW and NO basins show the largest increases between CO_2-stabilization and end-of-simulation. This coincides with a relatively late acceleration in the surface mass loss in these basins, and a relatively late timing of the emergence of the anthropogenic signal from the SMB natural variability (year 118 in the CW, and year 106 in the NO basin) compared to the average of all basins (year 93). The relative contribution of the SE basin to the total GrIS mass loss, that was largest at the time of CO_2-stabilization (19%) decreases to 12% at end-of-simulation. The SE basin responds early to the atmospheric forcing; with the anthropogenic signal in the SMB timeseries emerging in year 76. However, the SMB remains positive in this basin for a long time (to year 134) compared with the whole ice sheet (year 121), due to the high initial SMB, as this region receives large amounts of precipitation from the storm tracks, which is the reason that this basin cannot maintain its role as largest contributor to the GrIS mass loss.

A recent regional climate modelling study with the model RACMO forced with reanalysis data (Noël et al., 2019) finds that the relative role of the northern basins to the total GrIS mass loss increases between the 1990s and 2010s . Our simulation, too, shows an increasing relative contribution of the northern basins to the total-GrIS mass loss under the elevated CO_2 scenario. From the pre-industrial contribution of 35% of the total GrIS absolute SMB, the share of the northern basins increases to 44% at CO_2-stabilization. Two centuries after CO_2-stabilization, it increases slightly to 48%.

The southern drainage basins contribute the most to the simulated mass loss. The regions of largest mass loss between 2000 and 2010 have been observed with the Gravity Recovery and Climate Experiment (GRACE) mission in the SE and NW, due to ice loss in marine terminating glaciers (Bevis et al., 2019). Wang et al. (2019) find indications from GRACE and GPS observations that all southern GrIS drainage basins accelerate their ice mass loss. In our study, the largest initial mass loss is modelled in the southern drainage basins, and to a lesser degree in the north-west basin (Table 4.5). Further, Bevis et al. (2019) found the largest continuous acceleration of mass loss in the SW basin and therefore hypothesize that the SW basin will become a major

player in future GrIS mass loss. This hypothesis is supported by our simulation: the largest contribution to the GrIS SLR at end-of-simulation come from the SW basin.

4.3.3 Ice dynamical change

Figure 4.3 shows the spatial distribution of SMB and ice discharge change, as well as changes in surface velocity. Positive feedbacks mechanisms associated with albedo and elevation amplify and propagate the SMB response long after the forcing has stabilized, with the surface mass losses continuing to increase two centuries after CO_2-stabilization. Maximum surface mass loss values are found in the western and southern ablation zones, with local annual SMB rates at the ice sheet margin as low as -8 m yr^{-1}. The ablation zone expands throughout the simulation, raising the Equilibrium Line Altitude (ELA) to around 2000 m by years 131–150, and to 2500 m by years 331–350.

The expansion of the ablation zone results in extensive ice sheet thinning (Figures 4.3e and 4.3f), which in turn leads to increased ice flow from the interior towards the margins (Figures 4.3h and 4.3i). This ice flow acceleration is due to the formation of steeper slopes as the ELA rises. In fact, the ice sheet thickens somewhat in the interior, as a result of local increases in snowfall from an enhanced hydrological cycle (spatial maps of changes in snowfall and rain are discussed in section 4.3.4). As a result, the slope increases substantially where the ablation and accumulation zones meet. This increases the driving stress, giving higher velocities in the transition area between the high interior and the thinning margins. While faster flow partly reduces mass loss at the margins as ice advection from the interior increases, it favors inland migration of the equilibrium line and upstream thinning (e.g., Vizcaino et al. (2015)).

The gross pattern of SMB, velocity, and thickness change by year 140 is similar to the changes by 2081-2100 under the SSP5-8.5 simulation, however in the latter, the GrIS reaches a more negative SMB (-565 vs. -376 Gt yr^{-1}) due to a stronger increase in CO_2 forcing late in the simulation (after 2070) Muntjewerf et al. (2020a). As the ice sheet margins thin and retreat, outlet glaciers decelerate, resulting in almost 200 Gt yr^{-1} lower discharge by years 131-150 (Table 4.2). By end-of-simulation, ice sheet retreat results in a generally terrestrial margin. The ablation region covers around 60% of the total GrIS area.

4.3.4 Evolution of the Surface Mass Balance components

This section discusses the SMB and its components that are modelled by the land model, and defined in equations 4.1 and 4.2. We analyse the change patterns of the SMB components and properties of the snow/firn pack in order to gain further insight in the process of GrIS mass loss at the surface.

Surface mass balance: precipitation, runoff and sublimation

The SMB computed in the land model CLM5 decreases from 547 to -508 Gt yr^{-1} at CO_2-stabilization, to -2569 Gt yr^{-1} at end-of-simulation (Table 4.3). The anthro-
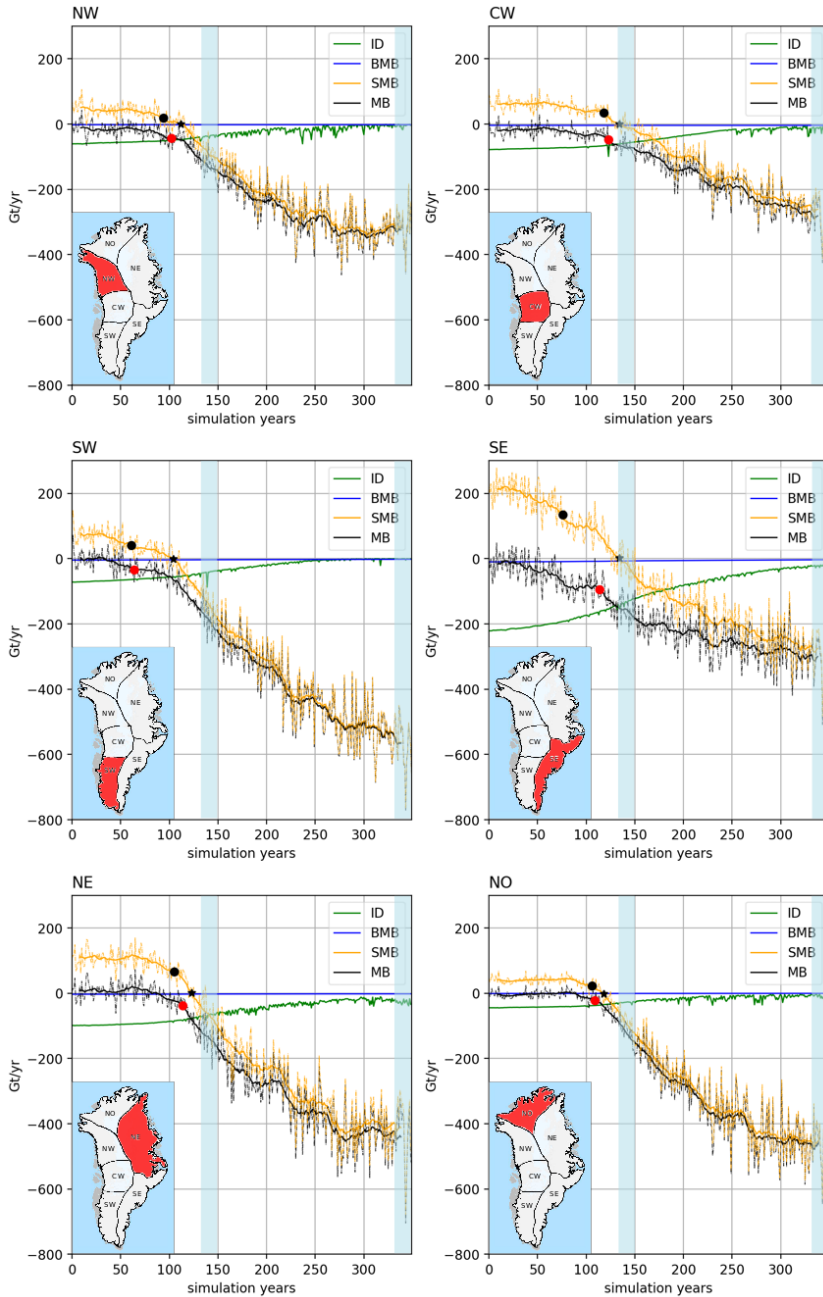
Figure 4.2: Basin timeseries of Mass Balance (black), Surface Mass Balance (orange), Basal Mass Balance (blue), and Ice discharge (green, defined as negative for visualization purposes)(Gt yr^{-1}). The MB and SMB solid lines: 20-year running mean values, other lines: yearly. Red dot: MB emergence. Black dot: SMB emergence. Black star: 20-year running mean SMB=0.
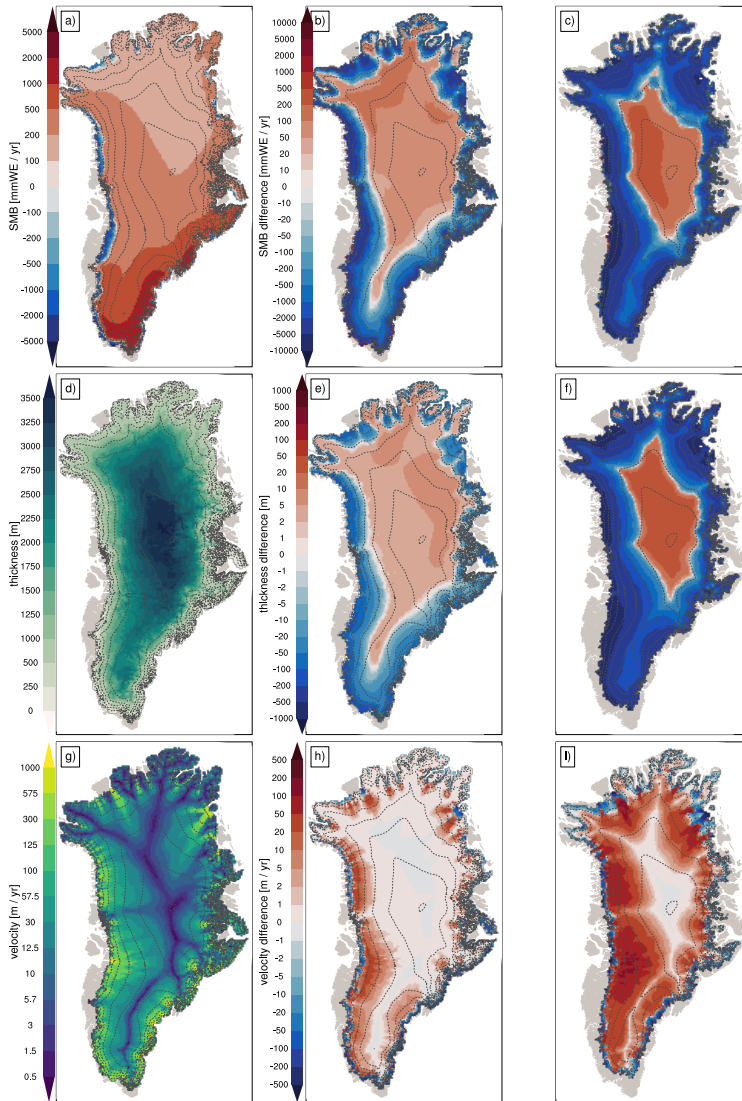
Figure 4.3: Pre-industrial absolute values (left column) and difference values of model years 131–150 (middle column) and 331–350 (right column) with respect to the pre-industrial. First row) Surface mass balance (mm yr^{-1}) with accumulation zones: SMB > 0 and ablation zones: SMB < 0, second row) ice sheet thickness (m), and third row) surface velocity (m yr^{-1}).

pogenic signal emerges in year 73 (Table 4.6). The SMB response downscaled to the
4-km ice sheet model grid is already discussed in section 4.3.3 (Figure 4.3). Figures
4.4.a.1-3 show the spatial SMB evolution in the coarser 1° CLM5 grid.

The GrIS atmosphere is significantly wetter in the CO_2-stabilization climate and
in the end-of-simulation climate compared to the pre-industrial, with 45% and 99%
increases in total precipitable water, respectively, and 18% and 33% increases in pre-
cipitation rates (Table 4.3). This is expected from the warming atmosphere and the
Clausius-Clapeyron rate at which the atmosphere's capacity to hold water increases
per degree temperature increase (Held and Soden, 2006). Arctic wetting trends are
commonly projected in human-induced climate warming scenarios in other mod-
elling studies (e.g., Schuenemann and Cassano (2010); Bintanja and Selten (2014);
Lenaerts et al. (2020); Bintanja et al. (2020)).

The GrIS-integrated anthropogenic signal emerges relatively late in the precipi-
tation time series from the background variability, in year 184. Contrary to the rest of
the ice sheet, precipitation decreases in the SE basin which is due to a strong decrease
in snowfall. The anthropogenic signal in the SE and SW basins does not emerge (Ta-
ble 4.6). Sellevold and Vizcaino (2020) attribute the smaller precipitation signal to
noise ratio in the southeast region to precipitation reductions from regional cooling
that is induced by NAMOC weakening, as a competing process to global warming
that generally enhances precipitation. Spatially, the precipitation increases inland,
adding more mass to the deep interior (Figure 4.4.b.2 and 4.4.b.3).

The surface runoff is the largest loss term in the SMB Equation 4.1. It increases
strongly, and early. The GrIS-integrated anthropogenic signal emerges in year 41.
There is almost five times the amount of runoff at CO_2-stabilization as in the pre-
industrial (Table 4.3). The runoff increases simultaneously with the ELA shifting to
higher elevations and the ablation zones expanding (Figure 4.5.a.2 and 4.5.a.3). The
amount of runoff at end-of-simulation is 13 times higher than in the pre-industrial.
The northern basins experience the largest relative increase: the contribution of the
three northern basins to the GrIS total runoff increases from 26% at pre-industrial to
51% at end-of-simulation.

Net deposition of water vapor in the pre-industrial era is simulated in the inte-
rior at elevations above the 2000 m elevation isoline. Mass is lost below 2000 m
due to sublimation (Figure 4.5.b.1). This result in the CESM2-CISM2 pre-industrial
simulation compares well with results from the regional climate model RACMO for
the present-day climate: Ettema et al. (2010) find year-round net deposition in the
dry snow zone, while sublimation is modelled in the spring and summer in regions
below 2000 m where the surface is heated but not yet melting. The simulated GrIS-
integrated sublimation initially increases as the ablation areas expand, but the flux
decreases after the first century of the simulation as deposition start to take place on
the bare ice. This pattern is simulated in all basins, except for the SW basin where
the sublimation flux decreases from the start, due to its relatively large ablation area.
Sublimation at CO_2-stabilization reaches further inland. At end-of-simulation, depo-
sition occurs all along the ice sheet margin except the east (Figure 4.5.b.3). The
anthropogenic signal of GrIS-integrated sublimation emerges from the background

variability in year 87 (Table 4.7).
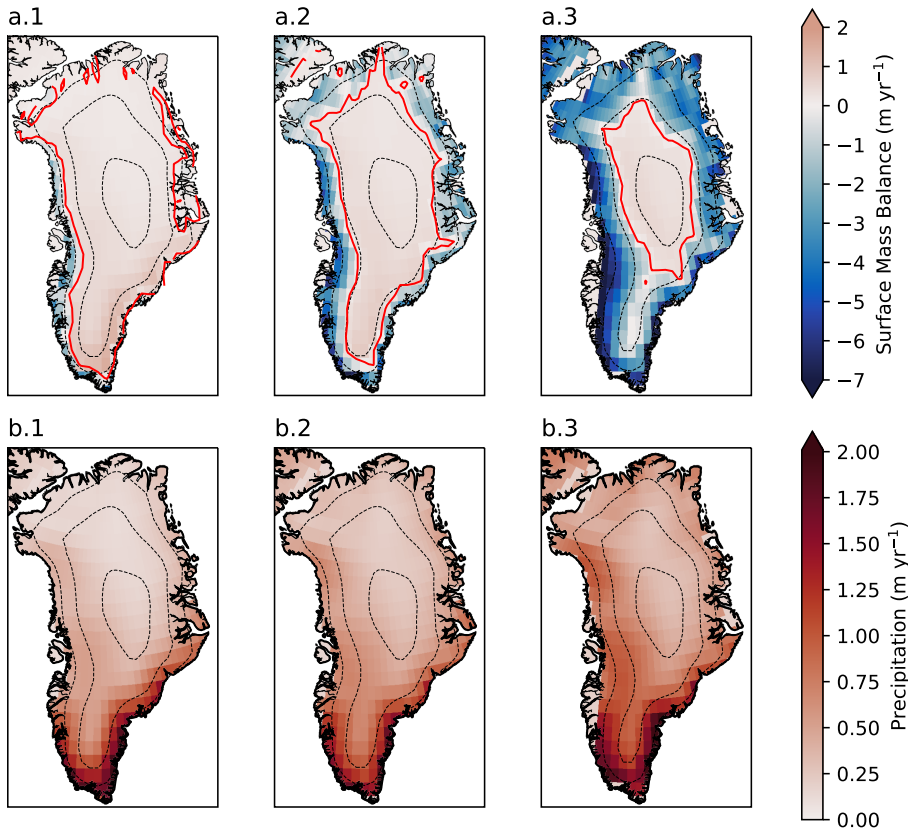
Figure 4.4: First row: Surface Mass Balance (m yr^{-1}) from the land model, second row: pre-cipitation (m yr^{-1}). Pre-industrial in the first column, CO$_2$-stabilization in the second column, and end-of-simulation in the third column. All fields are **ANN** averages. Contour lines for every 1000 m elevation. The red contour line denotes the ELA. Color coding: red adds mass to the surface, blue removes mass from the surface.

Precipitation: rain and snow

Annual mean GrIS-integrated snowfall rates decrease with the climatic warming (Table 4.3), but this downward trend does not emerge from the background variability in the GrIS-integrated timeseries. The snowfall trend in the two southern basins is downward, and in both basins the anthropogenic signal emerges near the end of the second century (Table 4.6). The snowfall increases in the three northern basins and in the CW basin, but only in the north basin does this upward trend emerge from the background variability.

Rain fall rates increase strongly, mainly along the western flank of the ice sheet (Table 4.3, Figures 4.6.a.2-3). The anthropogenic signal in the GrIS-integrated rain

Figure 4.5: For the pre-industrial average (first column), CO_2-stabilization (average of years 131–150; second column), and end-of-simulation (average of years 331–350; third column): the first row: runoff (m yr^{-1}), second row: sublimation (m yr^{-1}). All fields are **ANN** averages. Contour lines for every 1000 m elevation. The red contour line denotes the ELA. Color coding: red adds mass to the surface, blue removes mass from the surface.

emerges in year 56 (Table 4.6). This is much earlier than emergence for precipitation (year 184) and relatively close in time to the emergence of melt (year 40), refreezing (year 34) and runoff (year 41).

The emergence of the anthropogenic signal in rain fall in the SW and SE basins happens later than the GrIS-average, around the start of the first simulation century (years 92 and 113, resp). The three northern basins see the largest increases in rainfall relative to pre-industrial. The share of the GrIS total rainfall that falls in the three northern basins increases from 16% at pre-industrial to 39% at end-of-simulation.

Rain brings heat to the ice sheet. An increasingly larger fraction of precipitation falls as rain (from 9% in the pre-industrial to 39% at end-of-simulation on GrIS average). The three northern basins simulate the largest increases in rain fraction with respect to pre-industrial. Figures 4.6.b.1-3 show the fraction of the total summer (June - July - August (JJA)) precipitation that falls as rain. Most of the precipitation

Table 4.3: Annual ice-sheet-integrated surface mass balance and components mean [standard deviation] and anomalies of the mean with respect to pre-industrial (Gt yr^{-1}). SMB [1°] values are calculated as the sum of components in CLM5. SMB [4-km] values are in CISM2, after downscaling and remapping. SMB [1°] = snowfall + refreezing - melt - sublimation. Rain (%) = rain * 100 / (snowfall + rain). SMB [CLM5 basins] is the same as SMB [1°] but computed as the sum of all basins; the difference with SMB [1°] is due to interpolation. Refreezing (%) = refreezing * 100 / (rain + melt). All changes is the mean are significant (p < 0.05) except snowfall by 131–150. Differences with the downscaled SMB used by CISM2 (Table 4.2) are due to mass definition across components, for mass conservation purposes (see Chapter 2).

	Pre-industrial	Years 131–150	Years 331–350
SMB [4-km]	585 [85]	-367 [166]	-2,259 [357]
SMB [1°]	548 [94]	-510 [220]	-2575 [437]
SMB [CLM5 basins]	547 [94]	-508 [219]	-2569 [436]
Precipitation	847 [83]	995 [87]	1128 [99]
Snowfall	773 [74]	756 [68]	686 [72]
Rain	74 [16]	239 [38]	442 [58]
Refreezing	209 [46]	688 [72]	528 [41]
Melt	394 [91]	1910 [250]	3790 [438]
Runoff	254 [59]	1453 [223]	3697 [440]
Sublimation	45 [6]	55 [6]	16 [11]
Rain (%)	9	24	39
Refreezing (%)	45	32	12

in the ablation zones falls as rain, i.e., the rain fraction is > 0.5. This spatial feature is maintained as the ELA shifts up to higher elevations, meaning that moisture and heat reach higher up the ice sheet as the climate warming progresses.

Melt, refreezing, and the state of the snow pack

The simulated melt increases five-fold and ten-fold with respect to pre-industrial by CO_2-stabilization and by end-of-simulation, respectively (Table 4.3). The three northern basins see the largest increase with respect to the pre-industrial. Similar to runoff, the anthropogenic signal of melt emerges early for all basins (Table 4.7). Most of the pre-industrial melt takes place in the southern and western margins (Figure 4.7.a.1). As the climate warms, the melt rates intensify in the ablation areas all around (Figure 4.7.a.2-3).

Not all liquid water at the surface (i.e., rain and melt) runs off due to processes that take place in the snow pack. Liquid water may percolate into the snow where it can refreeze, or remain liquid in temperate firn. The snow pack can act as a barrier to runoff this way, preventing or delaying ice sheet mass loss (Vandecrux et al., 2020; Harper et al., 2012). Increasing amounts of liquid water in the snow pack, however, affect the firn's porosity, and, over time, deteriorate the capacity of the snow pack to buffer liquid water.

The simulated GrIS-integrated refreezing rate increase between pre-industrial and CO_2-stabilization from 209 to 688 Gt yr^{-1} (Table 4.3). The refreezing decreases to 528 Gt yr^{-1} between CO_2-stabilization and end-of-simulation. The snow pack
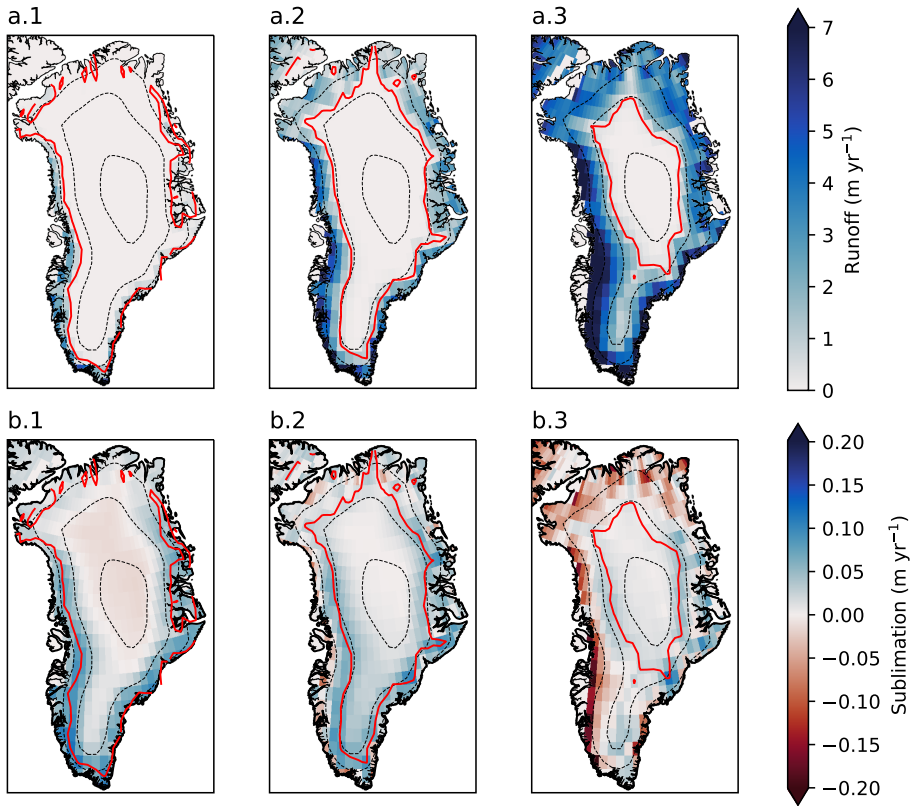
Figure 4.6: For the pre-industrial average (first column), CO_2-stabilization (average of years 131–150; second column), and end-of-simulation (average of years 331–350; third column): the first row: **ANN** rainfall (m yr^{-1}), second row: **JJA** fraction rainfall of total precipitation (rainfall + snowfall) (-). Contour lines for every 1000 m elevation. The red contour line denotes the ELA.

becomes less effective in retaining meltwater and preventing mass loss. The mean refreezing rate increases in the first part of the simulation, but the melt and rain increase more. At pre-industrial 45% of the rain and melt is refrozen, compared with 32% and 12% at CO_2-stabilization and end-of-simulation, respectively. This is a sign that the snow pack buffering capacity is being reduced, in connection with reduced snow depth and increased amount of liquid water in the snow pack (Figures 4.8.a.2-3 and Figures 4.8.b.2-3).

The ELA is the optimal altitude for refreezing because the amount of liquid water (melt water and rain) at the surface decreases with elevation, while the snow thickness increases with elevation. Paraphrasing Sellevold et al. (2019): the refreezing gradient is the sum of the opposing gradients of meltwater availability and refreezing capacity availability. The refreezing gradient is clearly reproduced in our simulation (Figure 4.7.b.2 and 4.7.b.3). The simulated pre-industrial refreezing (Figure 4.7.b.1)

agrees well with refreezing maps from present-day GrIS simulations with local snow and firn models with a detailed representation of meltwater retention processes (e.g., Steger et al. (2017b,a)). The enhanced refreezing decreases the refreezing capacity by warming the snow pack with the release of latent heat and by compaction from reduced pore space (Van Kampenhout et al., 2017). Further, the ice sheet elevation has lowered by end-of-simulation, with topography decreases of > 300m in the ablation zones (Figure 4.3f), contributing to enhanced melt via the SMB-elevation feedback.

Figure 4.7: For the pre-industrial average (first column), CO_2-stabilization (average of years 131–150; second column), and end-of-simulation (average of years 331–350; third column): the first row: melt (m yr^{-1}), second row: refreezing (m yr^{-1}). All fields are **ANN** averages. Contour lines for every 1000 m elevation. The red contour line denotes the ELA. Color coding: red adds mass to the surface, blue removes mass from the surface.

4.3.5 Evolution of the Surface Energy Balance components

This section discusses the surface energy balance and its components. The season of interest is are the summer months (June, July, and August, **JJA**), as this is the season with the most of surface melt. The sources of the additional melt energy (E_M)

Figure 4.8: For the pre-industrial average (first column), CO_2-stabilization (average of years 131–150; second column), and end-of-simulation (average of years 331–350; third column): the first row: fraction of liquid water in the snow pack (%), second row: snow depth (m). All fields are **ANN** averages. Contour lines for every 1000 m elevation. The red contour line denotes the ELA. Color coding: red adds mass to the surface, blue removes mass from the surface.

are quantified following the changes in the surface energy balance, as defined in equation 4.3: In the analysis we split the sources of net radiation at the surface into two categories: radiative fluxes (SW_{net} + LW_{net}) and non-radiative fluxes (LHF + SHF + GHF).

Melt energy and the relative contributions from the radiative and the non-radiative energy fluxes

The available melt energy increases quickly as the level of atmospheric CO_2 increases. In year 45, the anthropogenic signal of the GrIS melt energy emerges from the background variability. At CO_2-stabilization, the additional melt energy is 24 W m^{-2}, at end-of-simulation the change is +60 W m^{-2} (Table 4.4). Most of the additional melt

energy locates in the ablation zones (Figures 4.9.a.1-3). The basin that receives the largest increase in additional melt energy is the SW (+32 W m^{-2} at CO_2-stabilization and +88 W m^{-2} at end-of-simulation; Table 4.8).

Extra radiation at the surface supplies 74% of the GrIS average additional summer average melt energy by CO_2-stabilization. By end-of-simulation, this decreases to 61% (Table 4.4). The summer net radiation increases over the entire GrIS, with the greatest changes below the ELA (Figures 4.9.b.2 and 4.9.b.3). The sources of the additional melt energy per basin vary widely between extra net radiation and extra energy from the non-radiative fluxes (Table 4.8). In the SW basin, the additional net radiation is only responsible for 55% of the extra melt energy at CO_2-stabilization, and 52% at end-of-simulation. On the other extreme, in the NE basin, additional net radiation accounts for 97% of the extra melt energy at CO_2-stabilization, and 78% at end-of-simulation.

Table 4.4: Summer GrIS-averaged albedo (-), near-surface temperature and skin temperature (°C), incoming shortwave radiation at the surface, incoming longwave radiation at the surface, the surface energy balance components and the shortwave and long components of cloud radiative forcing SWCF and LWCF (W m^{-2}) (mean [standard deviation]). melt energy (E_M) = SW_{net} + LW_{net} + SHF + LHF + GHF. All changes in the mean are significant, except for LWCF (p < 0.05)

	Pre-industrial	Years 131–150	Years 331–350
Albedo	0.790 [0.005]	0.747 [0.011]	0.678 [0.015]
T_{2m}	-8.8 [0.4]	-3.5 [0.8]	-1.1 [0.6]
T_{skin}	-9.4 [0.4]	-4.2 [0.7]	-2.4 [0.5]
SW_{in}	319.8 [4.8]	297.7 [5.3]	287.3 [5.9]
LW_{in}	220.7 [4.7]	253.3 [3.4]	267.1 [4.3]
melt energy (E_M)	6.6 [1.6]	30.7 [5.1]	66.6 [8.1]
SW_{net}	65.8 [2.2]	72.8 [3.9]	87.5 [4.3]
LW_{net}	-53.4 [2.6]	-42.5 [2.5]	-37.0 [2.7]
SHF	5.4 [1.1]	9.1 [2.2]	18.1 [2.3]
LHF	-7.8 [0.4]	-7.1 [0.9]	-0.8 [1.6]
GHF	-3.4 [0.3]	-1.6 [0.5]	-1.2 [0.4]
SWCF	-9.5 [1.0]	-16.4 [1.5]	-22.3 [2.0]
LWCF	10.1 [1.0]	11.2 [0.9]	11.0 [1.1]

Longwave radiation

The initial primary heat source to the increase in melt energy is from changes in the longwave radiation, up to CO_2-stabilization time. At CO_2-stabilization, 45% of the GrIS average extra melt energy is from extra net longwave radiation (Table 4.4), which decreases to 27% by end-of-simulation. There is large spatial variation: in the SW basin the extra net longwave contributes only 26% to the extra melt energy at CO_2-stabilization, whereas in the northeast basin, this is 65% (Table 4.8).

Due to the increase in the atmospheric CO_2 concentration and atmospheric feedbacks of temperature and water vapour, more longwave radiation is emitted by the
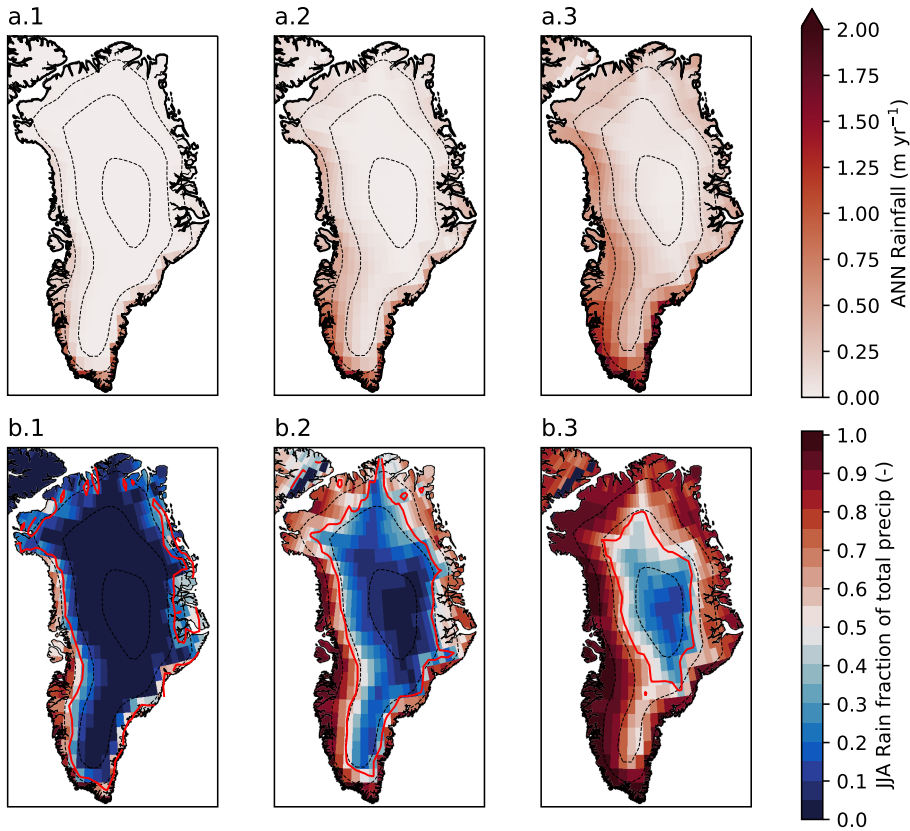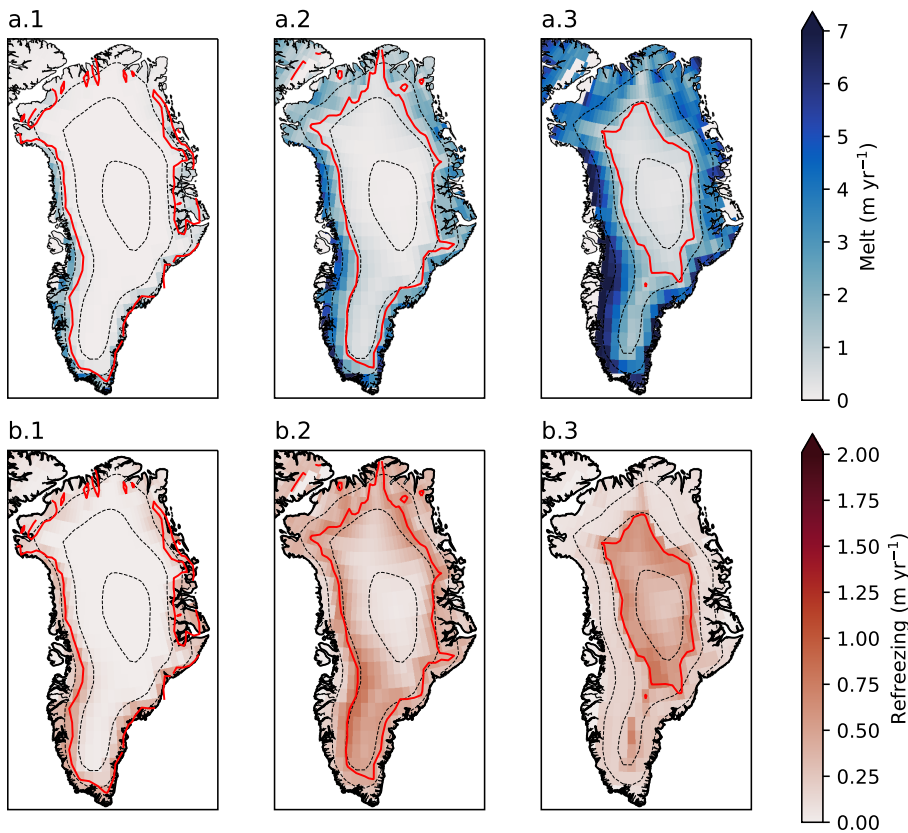
Figure 4.9: For the pre-industrial average (first column), CO_2-stabilization (average of years 131–150; second column), and end-of-simulation (average of years 331–350; third column): the first row: melt energy (E_M) at the surface (W m^{-2}), second row: net radiation at the surface (W m^{-2}), third row: net turbulent fluxes at the surface (sum of sensible heat flux, latent heat flux and ground heat flux) (W m^{-2}). All fields are **JJA** averages. Contour lines for every 1000 m elevation. The red contour line denotes the ELA. Color coding: red adds energy to the surface, blue removes energy from the surface.

atmosphere. Therefore, the amount of incoming longwave radiation at the surface increases (+32.6 W m^{-2} over the GrIS at CO_2-stabilization). The signal of the LW_{in} emerges early from the background variability, in year 45. The outgoing longwave radiation increases with increasing skin temperatures. For ice sheets, the emitted longwave radiation is limited because the skin temperature cannot exceed the melting point of ice. When assuming an ice surface radiates like a black body, the corresponding maximum emitted longwave radiation is approximately 315 W m^{-2}. When we look at the LW_{net}, we see in the simulation that the modelled atmospheric warming effect is stronger than the surface warming effect (+10.9 W m^{-2} over the GrIS at CO_2-stabilization). This results in a decrease of the summer longwave radiation deficit. Similar results are found in a study of a warming scenario with the regional climate model MAR (Franco et al., 2013), that show largest positive LW_{net} anomalies with respect to present-day near the GrIS margins.

The pre-industrial longwave deficit is largest in the north and northwest (Figure 4.10.a.1). With the climate warming, the net longwave increases mostly in the north and northeast basins, around +12 W m^{-2} (Table 4.8). The south-east and south-west basins receive relatively less additional net longwave radiation compared to the other basins of the GrIS, which is likely because the initial atmospheric temperatures and cloud thickness are higher here.

In addition to the atmospheric CO_2 concentration and the air temperature, the amount of precipitable water in the atmospheric column increases. Water in the atmosphere affects how much long wave radiation reaches the surface, via water vapour acting as a greenhouse gas, and via radiative behaviour of clouds (Schuenemann and Cassano, 2010). The simulated available column-integrated precipitable water in the pre-industrial summer over the GrIS is relatively small compared to over the surrounding seas, and proportional to the atmospheric column depth (Figure 4.10.b.1 and Figure 4.10.b.3). The warming atmosphere of the GrIS is more humid than in the pre-industrial, due to increased evaporation mainly over the nearby seas, and increased water-holding capacity of the warmer atmosphere.

Shortwave radiation

Shortwave radiation provides the secondary extra melt heat source at CO_2-stabilization, with 29% of the GrIS-average extra melt energy being from extra net shortwave radiation (Table 4.4). This percentage does not vary much across the basins, ranging between 25-32%. By the end-of-simulation, it has become the primary heat source to the additional melt energy for the GrIS-average and all basins alike, with contributions ranging between 35-41%. However, the absolute values of change in net shortwave radiation differ substantially among the basins, ranging between +17 W m^{-2} in the SE basin to +31 W m^{-2} in the SW basin (Table 4.8). The GrIS-average SW_{net} anthropogenic signal emerges from the background variability in year 121 (Table 4.8). It is at the same time the melt acceleration starts, indicating the onset of a widespread ice-albedo feedback.

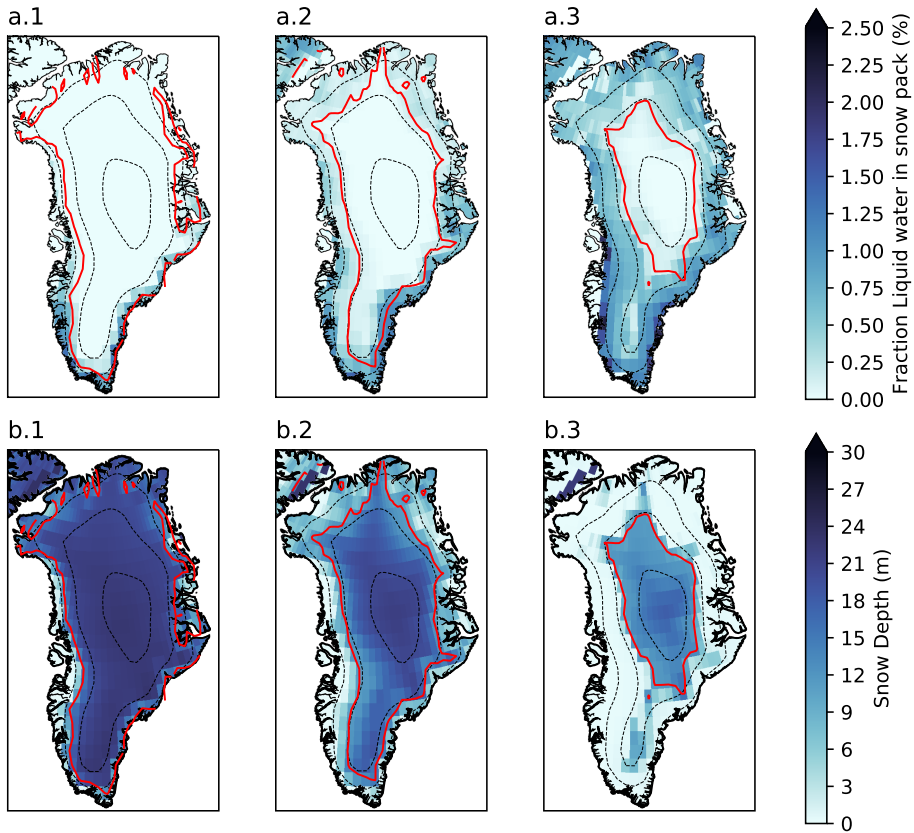The net shortwave radiation at the surface is the difference between the incoming
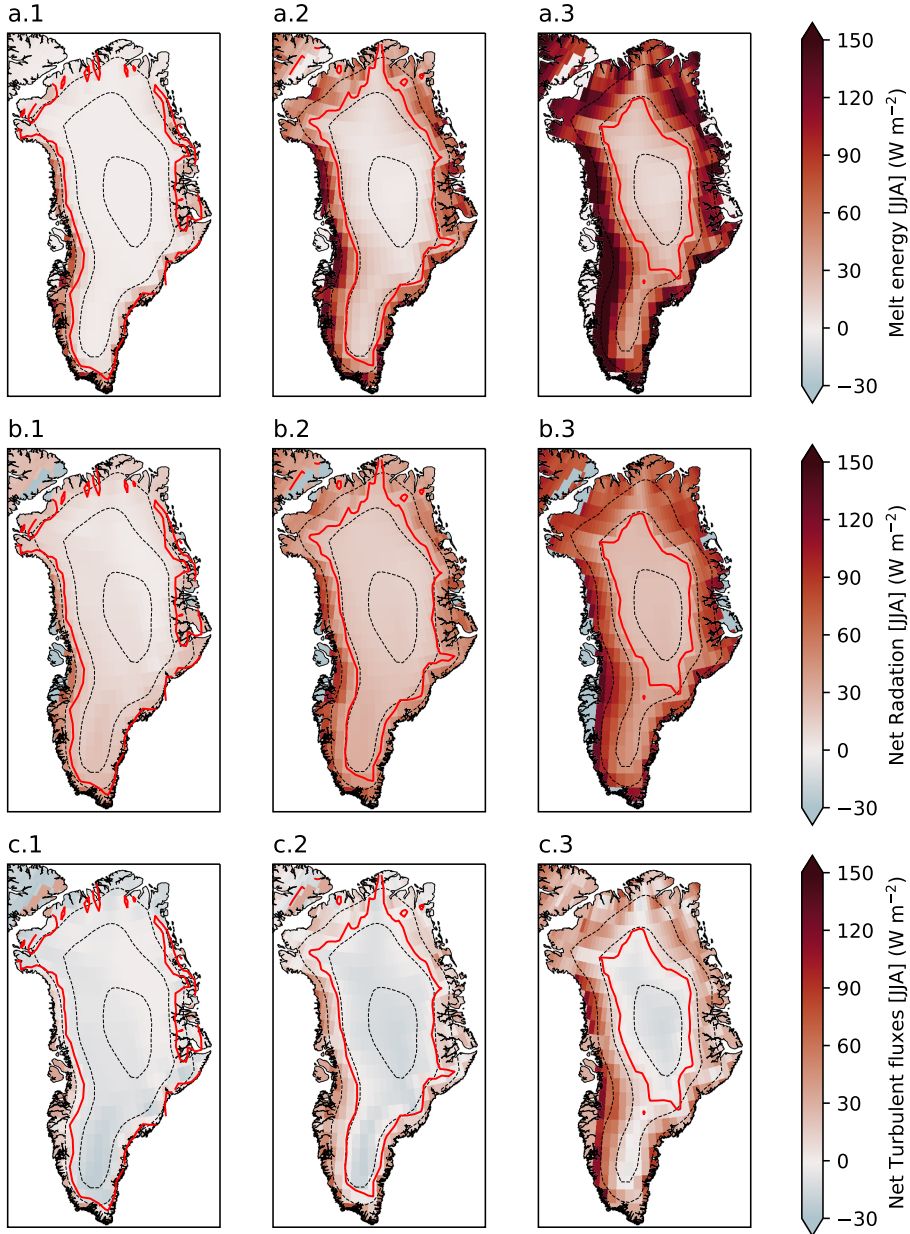
Figure 4.10: For the pre-industrial average (first column), CO_2-stabilization (average of years 131–150; second column), and end-of-simulation (average of years 331–350; third column): the first row: net longwave radiation at the surface (W m^{-2}), second row: total (vertically integrated) precipitable water (kg m^{-2}). All fields are **JJA** averages. Contour lines for every 1000 m elevation. Color coding: red adds energy to the surface, blue removes energy from the surface.

and the reflected shortwave radiation (SW_{net} = SW_{in} - SW_{out}). SW_{in} depends on the solar insolation, and on how transparent the atmosphere is for shortwave radiation. Solar insolation is the radiation received from the sun at the top of the atmosphere. It depends on the solar zenith angle, and can be considered constant on the centennial timescale. The transmissivity of the atmosphere for shortwave radiation is determined by the atmospheric composition (e.g., water vapor, clouds). We calculate the shortwave transmissivity as the ratio between incoming shortwave radiation at the surface and incoming shortwave radiation at the top of the atmosphere (TOA) (shortwave transmissivity = $SW_{in-surface}/SW_{in-TOA}$, following the definition by Ettema et al. (2010)). SW_{out} depends on surface properties and the amount of reflection. The ratio of reflected radiation and incoming radiation is the albedo (albedo = SW_{out}/SW_{in}).

The simulated shortwave transmissivity increases with elevation (Figure 4.11.b.1). The transmissivity over the GrIS is characterized by a longitudinal asymmetry, with larger transmissivity in the east. This is similar to the GrIS shortwave transmissivity field as modelled with the regional climate model RACMO for the years 1957–2008 (Ettema et al., 2010). The shortwave transmissivity decreases as our simulated climate warms (Figure 4.11.b.2 and 4.11.b.3). This indicates that the cloud water content and/or cloud cover is increasing.

Albedo decreases strongly with the simulated climate warming, from 0.790 in the pre-industrial, to 0.747 in the CO_2-stabilization climate, to 0.678 at end-of-simulation for the GrIS-average (Table 4.4). The SW basin sees the largest albedo decreases (Table 4.8), where wide areas of relatively dark ice are increasingly exposed. The albedo decreases the least in the SE basin, as the ablation zone does not gain area quickly due to the steep topographic gradient. The basin differences in albedo change align well with the differences in SW_{net} change noted above. The snow cover darkens due to increased temperatures and melt In the percolation zone that is immediately above the ELA (Figure 4.11.c.2 and 4.11.c.3).

The transmissivity of the atmosphere and the surface albedo have opposing effects on the SW_{net}. In sum, the decreased albedo has a larger effect on the SW_{net} than the increased cloudiness, resulting in an increase in GrIS-wide SW_{net} (Figure 4.11.a.2 and 4.11.a.3).

Cloud radiative forcing

Clouds influence the amount of radiation that reaches the surface. The effect clouds have on the amount of net shortwave radiation at the surface is called the Shortwave Cloud Forcing (SWCF) (SWCF). The SWCF here is defined as the net shortwave radiation at the top of the atmosphere (TOA) minus the net shortwave radiation at the top of the atmosphere in clear sky conditions (SWCF $= SW_{net-TOA} - SW_{net-TOA-clearsky}$). A negative value of SWCF has a cooling effect, as the net clear sky shortwave radiation at the top of the atmosphere is larger than the net cloudy shortwave radiation at the top of the atmosphere due to clouds reflecting incoming shortwave radiation. On the other hand, clouds can affect the amount of re-emitted longwave radiation. This effect is called the Longwave Cloud Forcing (LWCF), defined as the amount of outgoing longwave radiation in clear sky conditions minus the amount of outgoing longwave radiation in normal conditions (LWCF $= LW_{out-TOA-clearsky} - LW_{out-TOA}$). A positive LWCF has a warming effect where clouds act as a greenhouse that traps longwave radiation. The sum of the SWCF and the LWCF is the Total Cloud Radiative Forcing (TCRF), a metric for the net effects that clouds have on the net radiation balance.

The summer pre-industrial SWCF is slightly negative, meaning a cooling effect on Greenland (Figure 4.12.a.1). Largest shortwave cloud cooling takes place in the SW basin (Table 4.9). At CO_2-stabilization, the change in GrIS-average SWCF is -7 W m^{-2} (basin range -6 to -9 W m^{-2}). The anthropogenic signal of SWCF for the GrIS emerges in year 56. The simulated SWCF becomes gradually more negative over the
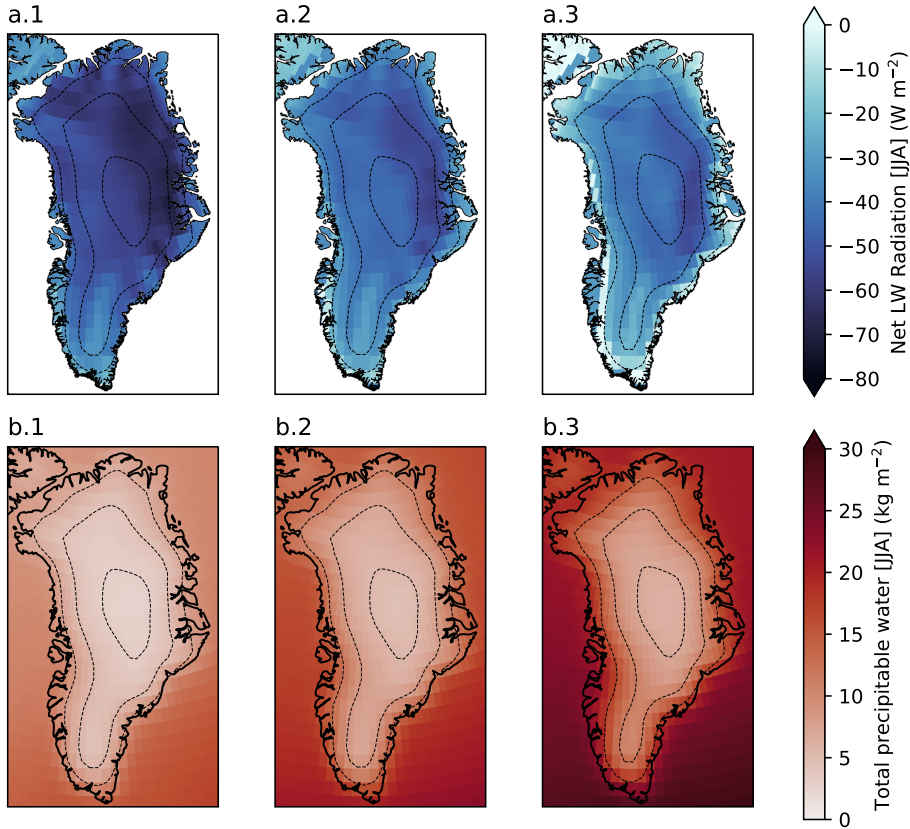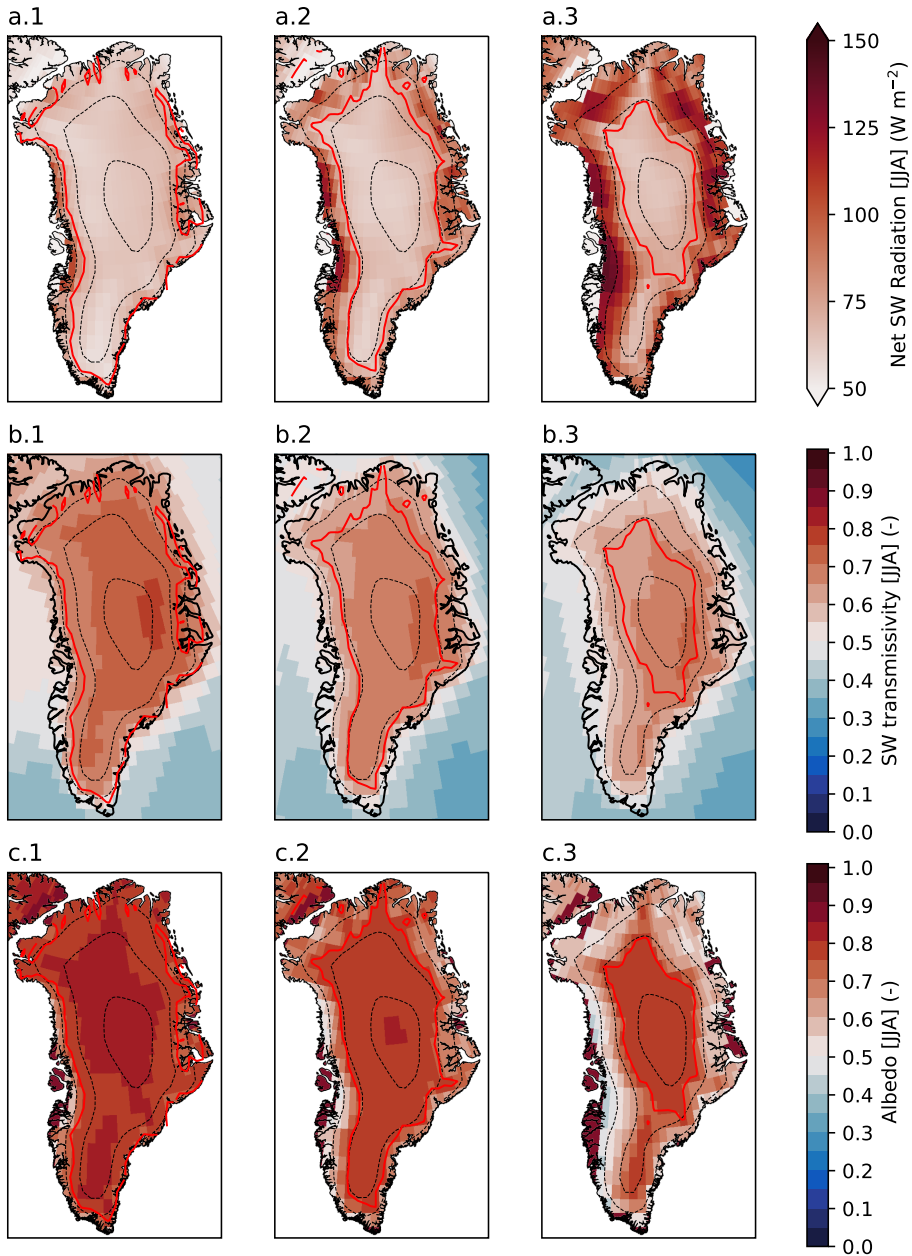
Figure 4.11: For the pre-industrial average (first column), CO_2-stabilization (average of years 131–150; second column), and end-of-simulation (average of years 331–350; third column): the first row: net shortwave radiation at the surface (W m^{-2}), second row: shortwave transmissivity (SW$_{in-surface}$/SW$_{in-TOA}$) (-), third row: albedo (-). All fields are **JJA** averages. Contour lines for every 1000 m elevation. The red contour line denotes the ELA. Color coding: red adds energy to the surface, blue removes energy from the surface.

entire GrIS with a downward linear trend from the start up to simulation year 250, after which the decrease levels off. The decrease is most strong so in the margins (Figure 4.12.a.2). This response is in line with feedback studies in warming scenarios; a negative Arctic shortwave cloud feedback is consistently found in CAM6 and its predecessors CAM4 and CAM5 (Lenaerts et al., 2020; Kay et al., 2012; Gettelman et al., 2012).

The change in SW_{in} is larger than the change due to the SWCF (Table 4.4). This is in part due to the SWCF definition not accounting for surface albedo change, because less radiation is reflected to the atmosphere and coming back to the TOA as reflected solar radiation. Holland and Landrum (2015) suggest other factors may further affect the SWCF metric in cases like this, that are indirectly related to the surface albedo change, such as reduced amount of scattering between the surface and clouds.

The simulated GrIS-average LWCF changes positively during the simulation but not significantly. Only in the NE basin a significant increase in LWCF is simulated and the anthropogenic signal in this basin emerges from the background variability in year 88 (Table 4.9). However, it is difficult to draw a robust conclusion given the positive biases in the LWP as noted by Van Kampenhout et al. (2019).

The TCRF in the summer as modelled for the pre-industrial is small but positive over the GrIS, except for low lying regions in the north (Figure 4.12.c.1). The TCRF decreases and switches sign as the modelled climate warms (Figures 4.12.c.2-3). Clouds have a net cooling effect at end-of-simulation on the GrIS, except for a small highly-elevated area in the east. Izeboud et al. (2020) assess the spatial heterogeneity of the cloud radiative effect and find that cloud cooling takes place in the ablation zones in the summer with an important a short-term impact on the SMB.

Non-radiative fluxes

The non-radiative fluxes are the sum of the sensible heat flux (SHF), the latent heat flux (LHF) and the ground heat flux (GHF). The sensible heat flux is the energy flux related to heating and cooling of a surface, and a function of the temperature gradient between the surface and the ambient air. The latent heat flux is the energy flux involved with phase changes, and is a function of the humidity gradient. Deposition of water vapour onto ice adds substantially to the available melt energy. Sublimation takes much energy to remove relatively little mass. That energy, subsequently, cannot be used for melt. Sublimation can be considered as a conserving mechanism of the ice sheet (Ettema et al., 2010). The ground heat flux is the heat transfer between surface and sub-surface, where surface is defined as the interface between the lowest atmosphere and the snow/ice/land surface. The positive change in ground heat flux can be considered a pre-conditioner to mass loss of glacial ice. The increase in the energy content in the snow pack prepares it for complete melt. The buffering of meltwater runoff, which preserves surface mass, is at the cost of heating the snow pack, as quantified for the period 1958 to 2015 in Van den Broeke et al. (2016).

The sum of the summer non-radiative fluxes is a heat sink in the pre-industrial simulation. The sensible heat flux provides energy for melt, but the latent heat flux

Figure 4.12: For the pre-industrial average (first column), CO_2-stabilization (average of years 131–150; second column), and end-of-simulation (average of years 331–350; third column): the first row: shortwave cloud forcing (W m^{-2}), second row: longwave cloud forcing (W m^{-2}), third row: total cloud radiative forcing (SWCF + LWCF) (W m^{-2}). All fields are **JJA** averages. Contour lines for every 1000 m elevation. The brown contour line denotes the zero-line of the total cloud radiative forcing. Color coding: red adds energy to the surface, blue removes energy from the surface.

and the ground heat flux withdraw energy from the surface (Table 4.4). However, at CO_2-stabilization, 26% of the additional melt energy is provided by the non-radiative fluxes with the largest share from changes in the sensible heat flux (15%). The ground heat flux contribution to the additional melt energy is the second largest (8%). Changes in the latent heat flux provide 3% of the additional melt energy. By end-of-simulation, 36% of the additional melt energy originates from the non-radiative fluxes. The change in the ground heat flux is smaller in the last half of the simulation compared with the first. Its contribution to the additional melt energy is (4%) at end-of-simulation. The sensible and latent heat fluxes contribute with 21% and 12%, respectively.

The pre-industrial summer sensible heat flux is generally positive over the GrIS, meaning heat transfer from the atmosphere to the surface, except for the south dome (Figure 4.13.a.1). The sensible heat flux increases as the simulated climate warms, and in the ablation zones the atmosphere heats faster than the ice sheet surface, which is limited to melting point. The anthropogenic signal of the GrIS-averaged SHF emerges in year 124 (Table 4.9). At CO_2-stabilization, the additional melt energy from the intensified sensible heat flux situates below the ELA, and the largest increase is modelled in the SW basin ($+7,7$ W m^{-2}, Table 4.9, Figure 4.13.a.2). The SW basin also experiences the largest SHF increase at end-of-simulation ($+23,7$ W m^{-2}). The SHF in the NE basin increases the least ($+6.2$ W m^{-2} at end-of-simulation).

The GrIS integrated latent heat flux in the pre-industrial summer is negative, meaning the surface loses energy due to sublimation in heated, non-melting regions. The largest negative latent heat flux values are simulated in the SE and SW basins, and in the percolation zone right above the ELA. The pre-industrial JJA latent heat flux map (Figure 4.13.b.1) agrees well with the reconstruction from Ettema et al. (2010) with the regional climate model RACMO during the period 1958-2008.

The anthropogenic signal of the GrIS-averaged LHF emerges from the natural variability in year 139 (Table 4.9). The sign of the latent heat flux on the ice sheet edge reverses at CO_2-stabilization (Figure 4.13.b.2 and 4.13.b.3). The near-surface air has become more humid. This leads to dry deposition, where moist air cools and saturates as it flows over the colder surface, such that the excess water vapour directly condensates (hoarfrost) and deposits on the ice. Deposition promotes large mass loss, as it provides additional melt energy to the surface energy balance but little additional mass. tThe GrIS integrated summer latent heat flux increase is $+7.0$ W m^{-2}) at end-of-simulation, resulting in a net value close to zero but still negative (Table 4.4). The largest increases occurs in the NO and SW basins ($+8.3$ and $+17.9$ W m^{-2}, respectively). In these two basins the integrated value of the LHF are now positive, i.e., summer deposition dominates (Table 4.9).

The GrIS integrated GHF is negative in the pre-industrial summer. This signal is mainly dominated by northern half of the GrIS and higher altitudes (Figure 4.13.c.1). The ground heat flux is positive in the percolation zone around the ELA. Energy from latent heat releases due to refreezing of meltwater in the snow pack is conducted upwards to the surface. The ground heat flux is negative in the western ablation zone because bare ice is exposed. The GrIS-integrated increase at CO_2-stabilization

is +1.8 W m^{-2}. The anthropogenic signal of the GrIS-averaged GHF emerges in year 86 from the natural variability (Table 4.9). It is interesting to note that the signal emerges much earlier than other non-radiative fluxes. The initial trend is upward in all the integrated timeseries, GrIS-average and basins alike. After CO_2-stabilization this upward trend slows down or levels off for most of the GrIS. For the SW basin the trend turns to downward from +2.6 W m^{-2} between start and CO_2-stabilization, to -2.2 W m^{-2} between CO_2-stabilization and end-of-simulation. The area where the ground heat flux is positive at CO_2-stabilization covers much of the southern half of the GrIS (Figure 4.13.c.2). The integrated GHF for the south-east and south-west basins is positive (Table 4.9). This corresponds with the decline of the refreezing capacity in these basins, linked to the decreased snow thickness and larger liquid water fraction of the snow pack. The three northern basins maintain negative area-integrated GHF values until end-of-simulation, likely because the north snow pack has sufficient cold content to buffer the latent heat releases.

4.4   Discussion and Conclusion

This study investigates the future multicentury evolution of the Greenland Ice Sheet (GrIS) with an Earth System Model (ESM) including an interactive ice sheet component (CESM2–CISM2). To this end, a 350-year simulation is used with forcing from an idealized 4xCO_2 scenario. By year 150 – one decade after CO_2-stabilization at 4x the pre-industrial concentration – the projected GrIS contribution to global mean SLR is 107 mm, with a global mean near-surface temperature increase of 5.3 K relative to pre-industrial. The AA factor (north of 60°N) is 1.6. The GrIS amplification factor is only 1.2. The NAMOC strongly declines, starting before a substantial increase in GrIS melting and runoff. After another 210 years of stable, elevated atmospheric CO_2, the total projected GrIS contribution to SLR is approximately 1,140 mm, and the global mean temperature increase is around 8.5 K.

In this simulation, the rate of SLR increases from 2 mm yr^{-1} in year 150 to almost 7 mm yr^{-1} in year 350. The SW basin provides the largest contribution to the total GrIS mass loss. The relative contribution of the northern basins to the total GrIS mass loss increases over the course of the simulation. The accelerated GrIS mass loss is caused by rapidly increasing surface mass loss. This is compensated by a reduction in ice discharge, as the GrIS margins thin and retreat, and many outlet glaciers become land terminating. The final GrIS area loss is around 20% of the spun-up initialization ice sheet state.

The SMB decreases slowly at the start of the simulation, and increased longwave radiation is the primary source of the extra melt as the atmospheric CO_2 concentration increases. Refreezing of meltwater that has percolated into the snow increases the energy content of the snow pack due to latent heat release. This prepares the snow pack for complete melt, and the ablation areas for expansion. Surface ablation and overall mass loss start accelerating after about 120 years of increasing CO_2, corresponding to a global warming of 4.2 K. This is when the rate of SLR starts to increase rapidly. At this time, the ablation areas have expanded enough to trigger
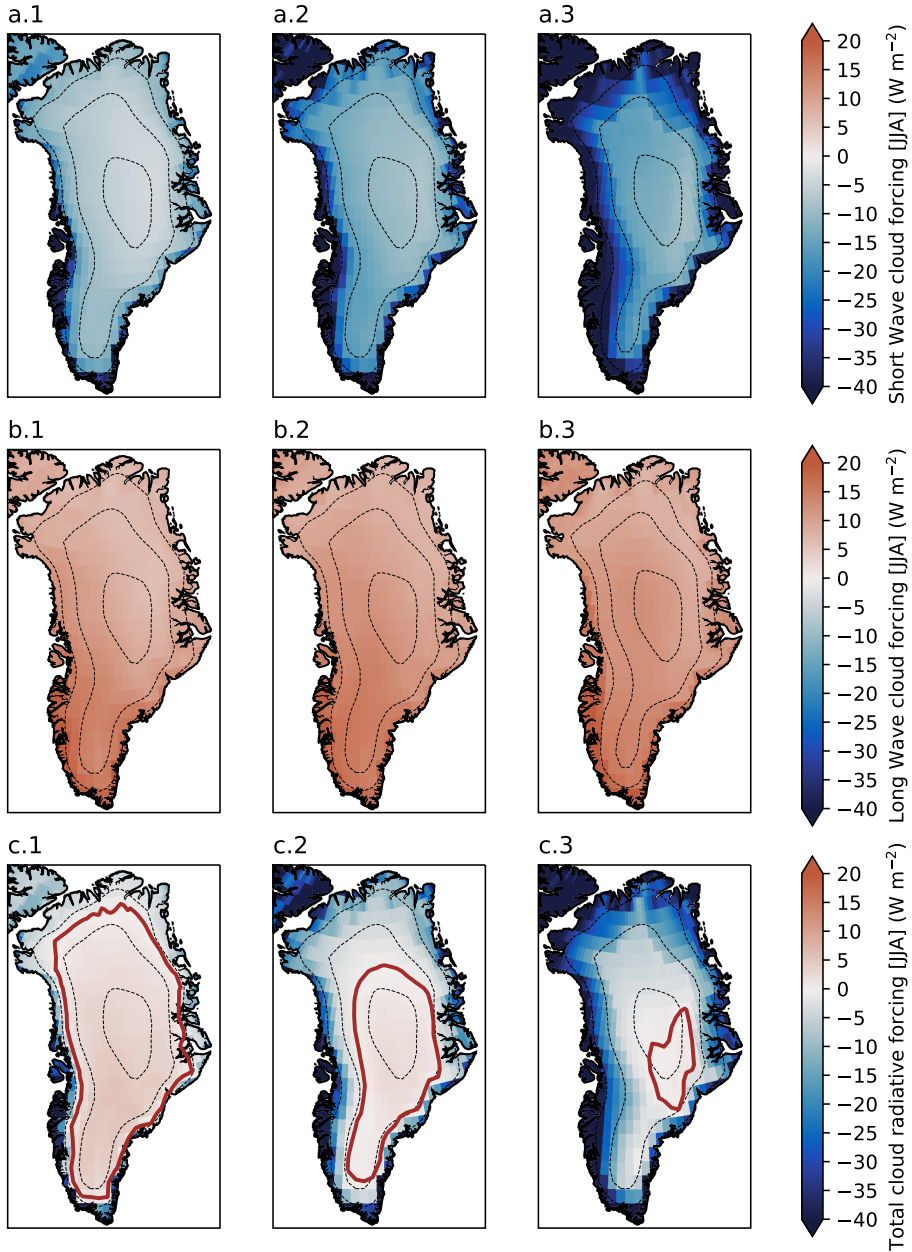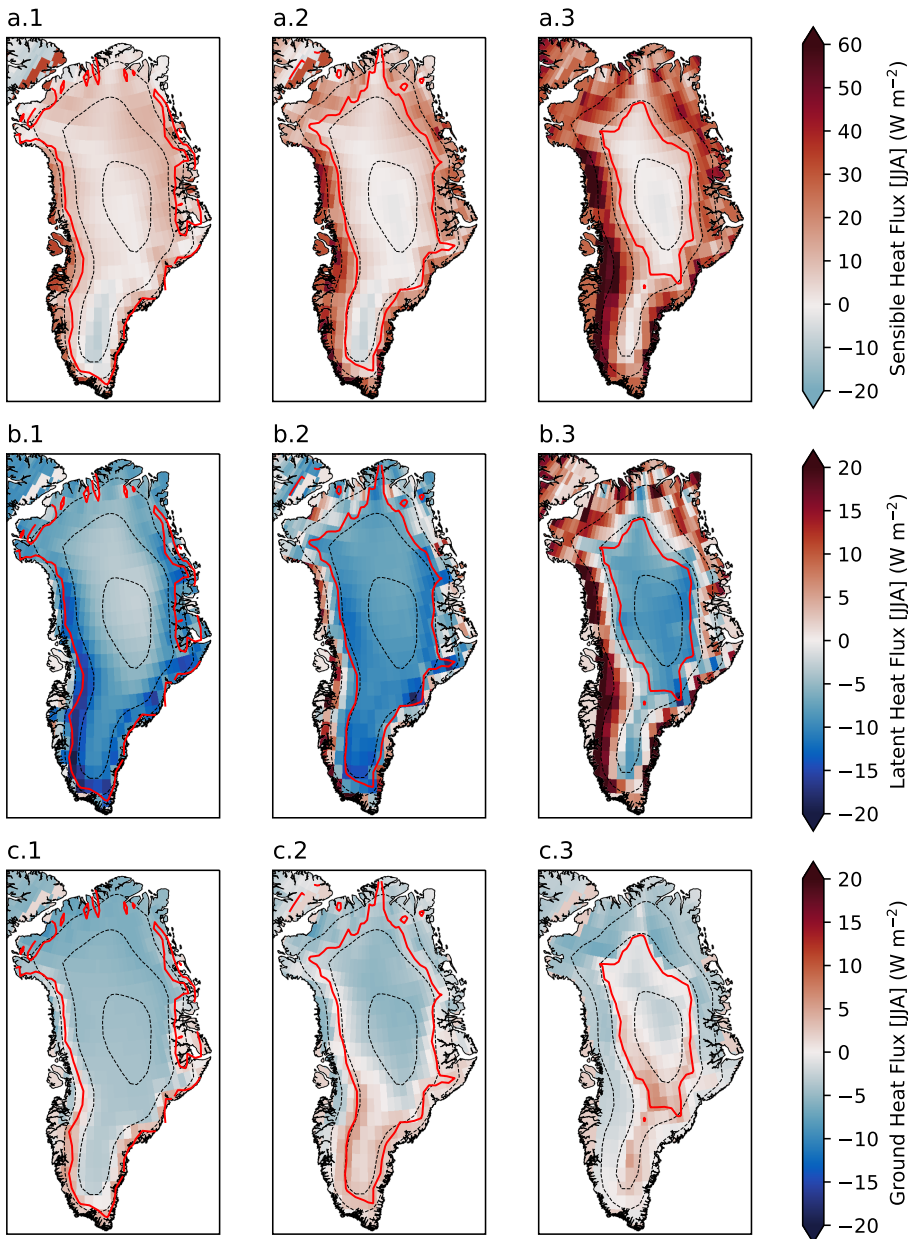
Figure 4.13: For the pre-industrial average (first column), CO_2-stabilization (average of years 131–150; second column), and end-of-simulation (average of years 331–350; third column): the first row: sensible heat flux (W m^{-2}), second row: latent heat flux (W m^{-2}), third row: ground heat flux (W m^{-2}). All fields are **JJA** averages. Contour lines for every 1000 m elevation. The red contour line denotes the ELA. Color coding: red adds energy to the surface, blue removes energy from the surface.

widespread impact of the ice-albedo feedback, and the net shortwave radiation at the surface increases. The total cloud radiative forcing in the summer has a small cooling effect, in contrast to the small warming effect in the pre-industrial era, for which we note that the decrease in incoming shortwave radiation over the GrIS are less effective due to the high surface albedo relative to other Earth regions. The summer sensible heat flux further amplifies GrIS melt due to a larger temperature gradient between the surface and the ambient air. Additionally, the latent heat flux adds to the melt energy via deposition that takes place in the ablation zones. By end-of-simulation, the additional net shortwave radiation is the primary source of the extra melt energy. The ablation region covers around 60% of the total GrIS area.

The main novelty of this study comes from the use of an advanced coupled Earth system/ice sheet model, CESM2–CISM2, to investigate future, multicentury, climate and GrIS evolution. The model has relatively high resolution (1°) in the ocean and atmospheric components, and an advanced SMB calculation with energy fluxes computed directly in the climate component. The study therefore bridges the gap between multicentury and multimillenia ice sheet model-only SLR projections (e.g., Aschwanden et al. (2019)) and century-scale SMB projections from global and regional climate models.

Centennial timescale comparisons of our projected GrIS SLR contribution can be made with previous estimates under the CMIP RCP8.5 and SSP8.5 scenarios, in which the CO_2 concentration is close to $4xCO_2$ by year 2100. Our model finds 107 mm SLE at $4xCO_2$. Using CESM1.0, Vizcaino et al. (2014) projects 55 mm by year 2100 from the SMB simulation alone, under a global warming of 3.7 K. When forcing a stand-alone ice sheet model (CISM1.0, a comparatively low complexity predecessor of CISM2) with the aforementioned CESM1.0 SMB field, the total mass loss – including both SMB and ice discharge – is 76 mm by year 2100 (Lipscomb et al., 2013). The coarse-resolution Earth system/ice sheet model study by Vizcaino et al. (2015) projects 2100 SLR and global warming of 67 mm and 4.3 K, respectively. Moreover, in an ice sheet model-only study with PISM, Aschwanden et al. (2019)) estimate a GrIS SLR contribution of 140–330 mm by year 2100, with a global mean temperature change of around 5 K. Finally as covered in Chapter 3, Muntjewerf et al. (2020a) project 109 mm from the GrIS under the SSP5-8.5 scenario with CESM2–CISM2.

GrIS behaviour on multicentury time scales with forcing from ESMs has been investigated by relatively few studies to date. It requires either an expensive simulation with a coupled Earth system/ice sheet model or an ice sheet-only simulation with appropriate SMB downscaling to account for the growing divergence between the static GrIS geometry in the climate model and the evolving geometry in the ice sheet model. An example of the former is the relatively coarse-resolution, coupled model in Vizcaino et al. (2015) that projects a GrIS SLR contribution of 536 mm by year 2300 under a simulated temperature anomaly of 9.4 K. In contrast, the RCP8.5 ice sheet model simulations by Aschwanden et al. (2019) estimate a GrIS SLR contribution of 940-3,740 mm under a 10-K warming in year 2300. Our projection lies at the lower end of this range.

The lack of direct ocean forcing of the GrIS is a limitation of this study. Fürst et al.

(2015) include temperature forcing at calving fronts along with surface forcing, and estimate 102 mm under the CMIP5 RCP8.5 scenario. Mass loss due to enhanced ice dynamics from ocean forcing is estimated to be an order of magnitude smaller: Price et al. (2011) find 6 mm of committed dynamic mass loss from ocean forcing by 2100. Nick et al. (2013) project a dynamic contribution between 11 and 18 mm by 2100 from four representative outlet glaciers. On the other hand, RCP8.5 simulations without ocean forcing give reduced ice discharge at 2100 relative to present day (Ruckamp et al., 2019; Vizcaino et al., 2015). Although ocean interactions are second order compared to SMB for overall GrIS mass loss (on the whole ice sheet scale), the above suggests that ocean forcing enhances solid ice discharge, which otherwise decreases. The question remains what the net effect is: answering this requires the development of models with GrIS-ocean interactions. The ISMIP6 stand-alone ice sheet model GrIS ice-ocean experiments is a study in progress that aims to better understand ocean terminus and ocean shelf processes. In this intercomparison project, ice sheet models are provided with scenario ocean boundary forcing (Slater et al., 2019) to accommodate experiments of marine terminus retreat and submarine melt parameterizations (e.g., Leguy et al. (2020)).

In agreement with previous work, our results show how sustained high CO_2 results in large, accelerating GrIS mass loss. We have shown how coupled climate and ice sheet modelling via advanced SMB calculations provides novel insights in both short- and long-term coupling of global and regional climate change and ice sheet melt change. Adequate modelling of global climate as well as snow and ice processes is key to capturing the interactions and feedbacks that will determine future changes.

4.A   Change in Mass Balance components per basin

Table 4.5: MB and components (mean)(Gt yr^{-1}) and cumulative mass loss (mm SLE) for the pre-industrial and the 1% simulation (years 131–150 and 331–350). Basins as in Figure 4.2.

		Pre-industrial	Years 131–150	Year 331–350
Surface Mass Balance (Gt yr^{-1})	GrIS	585	-367	-2,259
	NW	52	-82	-309
	CW	67	-7	-259
	SW	95	-132	-559
	SE	218	-10	-276
	NE	112	-59	-407
	NO	41	-77	-448
Ice Discharge (Gt yr^{-1})	GrIS	574	378	77
	NW	60	39	5
	CW	78	59	15
	SW	72	45	1
	SE	219	137	21
	NE	100	69	27
	NO	44	29	8
Mass Balance (Gt yr^{-1})	GrIS	-13	-764	-2,350
	NW	-10	-123	-316
	CW	-14	-70	-278
	SW	18	-180	-562
	SE	-11	-154	-301
	NE	8	-131	-436
	NO	-4	-107	-456
Cumulative contribution to SLR (mm SLE)	GrIS	-	107	1,140
	NW	-	15	166
	CW	-	9	111
	SW	-	32	279
	SE	-	27	164
	NE	-	13	211
	NO	-	11	210

4.B   Change in Surface Mass Balance components per basin

Table 4.6: SMB and components (mean [standard deviation]) (Gt yr^{-1}) for the pre-industrial and the 1% simulation (years 131–150 and 331–350). Last column: year of emergence of the anthropogenic signal with respect to the pre-industrial mean. Basins as in Figure 4.2.

		Pre-industrial (Gt yr^{-1})	Years 131–150 (Gt yr^{-1})	Year 331–350 (Gt yr^{-1})	Emergence (year)
SMB	GrIS	547 [94]	-508 [219]	-2569 [436]	73
	NW	50 [19]	-112 [36]	-362 [64]	90
	CW	62 [20]	-36 [25]	-329 [74]	112
	SW	88 [30]	-148 [56]	-544 [82]	72
	SE	199 [41]	-13 [54]	-303 [90]	78
	NE	108 [25]	-103 [67]	-511 [115]	97
	NO	41 [9]	-96 [36]	-520 [81]	99
Precipitation	GrIS	845 [83]	993 [87]	1126 [99]	184
	NW	89 [16]	129 [22]	169 [29]	135
	CW	104 [16]	131 [19]	178 [27]	147
	SW	197 [24]	211 [22]	212 [27]	-
	SE	267 [44]	241 [34]	235 [28]	-
	NE	137 [22]	190 [34]	203 [30]	110
	NO	51 [8]	92 [15]	129 [23]	73
Rainfall	GrIS	74 [16]	239 [38]	441 [57]	56
	NW	6 [3]	34 [11]	74 [19]	66
	CW	7 [3]	31 [7]	74 [15]	68
	SW	31 [7]	80 [16]	117 [17]	92
	SE	23 [7]	47 [8]	79 [13]	113
	NE	4 [2]	27 [6]	46 [10]	45
	NO	2 [1]	20 [7]	51 [16]	40
Snowfall	GrIS	772 [74]	754 [67]	685 [72]	-
	NW	83 [15]	94 [15]	95 [14]	-
	CW	97 [15]	100 [14]	104 [17]	-
	SW	166 [20]	131 [14]	95 [15]	179
	SE	244 [39]	194 [30]	155 [24]	195
	NE	133 [21]	163 [29]	157 [24]	-
	NO	49 [8]	71 [12]	78 [13]	121
Refreezing	GrIS	208 [46]	687 [72]	527 [41]	34
	NW	26 [8]	89 [13]	80 [9]	48
	CW	23 [7]	92 [12]	88 [6]	53
	SW	50 [9]	114 [8]	48 [4]	56
	SE	45 [7]	105 [8]	82 [4]	57
	NE	42 [11]	166 [25]	168 [28]	33
	NO	21 [10]	120 [14]	61 [4]	41

Table 4.7: Continuation of Table 4.6. Basins as in Figure 4.2.

		Pre-industrial (Gt yr^{-1})	Years 131–150 (Gt yr^{-1})	Year 331–350 (Gt yr^{-1})	Emergence (year)
Melt	GrIS	393 [91]	1905 [250]	3782 [437]	40
	NW	55 [16]	289 [40]	538 [69]	46
	CW	53 [14]	221 [32]	520 [71]	55
	SW	118 [25]	385 [58]	690 [72]	55
	SE	79 [17]	303 [44]	536 [72]	37
	NE	61 [17]	422 [65]	832 [125]	33
	NO	28 [12]	285 [39]	666 [80]	32
Runoff	GrIS	253 [59]	1449 [223]	3689 [439]	41
	NW	34 [10]	234 [36]	531 [70]	43
	CW	36 [9]	160 [27]	506 [73]	59
	SW	96 [22]	349 [66]	758 [75]	55
	SE	56 [16]	241 [42]	530 [77]	46
	NE	22 [7]	281 [46]	709 [104]	30
	NO	9 [3]	184 [30]	655 [84]	44
Sublimation	GrIS	45 [6]	55 [6]	16 [11]	87
	NW	5 [1]	7 [1]	2 [2]	86
	CW	6 [1]	7 [1]	2 [2]	267
	SW	13 [1]	12 [2]	0 [2]	151
	SE	12 [1]	14 [1]	9 [2]	279
	NE	7 [2]	13 [2]	7 [3]	63
	NO	2 [1]	3 [1]	-3 [2]	65

4.C Change in Surface Energy Balance components per basin

Table 4.8: SEB and components (mean [standard deviation])(W m^{-2}) for the pre-industrial and the 1% simulation (years 131–150 and 331–350). Last column: year of emergence of the anthropogenic signal with respect to the pre-industrial mean. Basins as in Figure 4.2.

		Pre-industrial (W m^{-2})	Years 131–150 (W m^{-2})	Year 331–350 (W m^{-2})	Emergence (year)
melt energy (E_M)	GrIS	6.6 [1.6]	30.7 [5.1]	66.6 [8.1]	45
	NW	5.6 [1.9]	30.6 [5.6]	67.2 [8.9]	54
	CW	6.3 [2.0]	28.0 [5.4]	66.4 [9.7]	59
	SW	12.8 [3.2]	45.1 [8.5]	100.8 [11.6]	59
	SE	7.9 [1.9]	30.7 [5.5]	60.2 [8.1]	53
	NE	3.2 [1.0]	21.8 [4.2]	50.0 [8.6]	35
	NO	2.9 [1.4]	28.3 [5.0]	75.0 [9.9]	44
SW_{in}	GrIS	319.8 [4.8]	297.7 [5.3]	287.3 [5.9]	67
	NW	315.3 [9.8]	292.2 [12.3]	280.9 [13.8]	183
	CW	319.0 [8.9]	296.7 [9.3]	289.0 [8.7]	97
	SW	300.2 [9.4]	281.6 [9.6]	271.4 [8.7]	162
	SE	313.6 [8.6]	296.2 [7.9]	294.3 [10.6]	192
	NE	335.7 [5.1]	313.0 [7.5]	302.0 [6.8]	59
	NO	323.2 [7.8]	295.9 [11.6]	272.4 [17.7]	88
LW_{in}	GrIS	220.7 [4.7]	253.3 [3.4]	267.1 [4.3]	45
	NW	221.3 [7.3]	253.8 [6.2]	267.1 [6.9]	78
	CW	219.1 [7.7]	252.0 [5.8]	264.6 [5.0]	78
	SW	244.0 [6.3]	268.8 [5.3]	283.7 [4.6]	82
	SE	228.4 [6.9]	257.0 [5.0]	269.1 [6.5]	83
	NE	204.0 [5.0]	241.8 [4.1]	256.3 [5.2]	42
	NO	221.0 [5.7]	255.7 [5.1]	274.2 [7.4]	56
SW_{net}	GrIS	65.8 [2.2]	72.8 [3.9]	87.5 [4.3]	121
	NW	63.9 [4.0]	71.3 [6.3]	85.3 [7.5]	148
	CW	66.0 [4.1]	71.4 [5.2]	87.3 [6.4]	169
	SW	63.6 [4.4]	73.0 [5.4]	94.1 [9.5]	138
	SE	64.6 [3.7]	70.3 [4.0]	81.8 [6.7]	146
	NE	67.7 [2.3]	73.6 [4.6]	86.8 [5.3]	123
	NO	64.7 [3.2]	72.1 [5.8]	89.8 [10.0]	129
LW_{net}	GrIS	-53.4 [2.6]	-42.5 [2.5]	-37.0 [2.7]	72
	NW	-52.2 [5.3]	-42.0 [5.2]	-36.7 [5.4]	148
	CW	-52.9 [5.3]	-42.6 [4.7]	-39.2 [3.9]	145
	SW	-40.4 [4.8]	-32.0 [4.2]	-24.8 [4.4]	172
	SE	-49.0 [4.8]	-39.7 [3.4]	-35.8 [5.4]	203
	NE	-61.5 [3.0]	-49.4 [3.7]	-44.2 [3.1]	62
	NO	-55.3 [4.2]	-43.1 [5.0]	-32.8 [6.4]	119

Table 4.9: Continuation of Table 4.8. Basins as in Figure 4.2.

		Pre-industrial (W m^{-2})	Years 131–150 (W m^{-2})	Year 331–350 (W m^{-2})	Emergence (year)
Albedo	GrIS	0.790 [0.005]	0.747 [0.011]	0.678 [0.015]	71
	NW	0.791 [0.008]	0.745 [0.013]	0.678 [0.017]	98
	CW	0.786 [0.009]	0.750 [0.013]	0.688 [0.018]	112
	SW	0.770 [0.010]	0.716 [0.017]	0.629 [0.027]	98
	SE	0.790 [0.007]	0.748 [0.012]	0.699 [0.018]	89
	NE	0.796 [0.005]	0.757 [0.011]	0.698 [0.014]	88
	NO	0.799 [0.007]	0.752 [0.012]	0.647 [0.023]	93
SHF	GrIS	5.4 [1.1]	9.1 [2.2]	18.1 [2.3]	124
	NW	5.4 [2.2]	10.5 [2.7]	20.6 [3.2]	130
	CW	4.8 [2.0]	8.0 [2.7]	19.2 [3.2]	153
	SW	2.1 [1.7]	9.8 [3.5]	25.8 [3.3]	113
	SE	3.8 [1.8]	7.6 [2.9]	15.6 [2.5]	136
	NE	7.5 [1.4]	8.2 [2.3]	13.7 [2.3]	212
	NO	5.3 [1.6]	8.6 [2.2]	19.2 [3.4]	135
LHF	GrIS	-7.8 [0.4]	-7.1 [0.9]	-0.8 [1.6]	139
	NW	-7.4 [0.6]	-6.6 [1.0]	-0.2 [2.1]	149
	CW	-8.7 [0.9]	-8.1 [1.1]	-1.3 [2.1]	155
	SW	-12.3 [1.0]	-8.1 [2.2]	5.6 [2.9]	113
	SE	-10.3 [0.5]	-9.0 [1.3]	-3.2 [1.6]	127
	NE	-6.0 [0.5]	-7.3 [0.7]	-4.2 [1.5]	65
	NO	-5.8 [0.6]	-5.5 [1.2]	2.5 [2.3]	84
GHF	GrIS	-3.4 [0.3]	-1.6 [0.5]	-1.2 [0.4]	86
	NW	-4.0 [0.5]	-2.6 [0.7]	-1.8 [0.7]	111
	CW	-3.0 [0.5]	-0.7 [0.9]	0.5 [0.6]	101
	SW	-0.2 [0.5]	2.4 [1.0]	0.2 [0.9]	63
	SE	-1.2 [0.4]	1.6 [0.6]	1.8 [0.6]	58
	NE	-4.5 [0.4]	-3.4 [0.6]	-2.1 [0.6]	108
	NO	-6.0 [0.4]	-3.8 [0.7]	-3.7 [0.8]	89
SWCF	GrIS	-9.5 [1.0]	-16.4 [1.5]	-22.3 [2.0]	56
	NW	-10.2 [1.9]	-18.1 [3.5]	-24.9 [5.2]	98
	CW	-9.3 [1.7]	-16.2 [2.4]	-20.8 [3.2]	80
	SW	-16.3 [2.3]	-23.9 [3.0]	-29.4 [3.4]	90
	SE	-11.0 [1.8]	-17.1 [2.2]	-17.8 [3.1]	96
	NE	-6.3 [0.9]	-12.2 [2.2]	-17.3 [2.5]	55
	NO	-8.4 [1.5]	-17.1 [3.3]	-29.8 [6.8]	73
LWCF	GrIS	10.1 [1.0]	11.2 [0.9]	11.0 [1.1]	-
	NW	10.2 [1.9]	11.3 [1.7]	11.6 [2.1]	-
	CW	11.8 [2.1]	13.4 [1.7]	12.3 [1.9]	-
	SW	15.6 [2.0]	15.6 [1.5]	14.5 [1.9]	-
	SE	12.4 [1.8]	13.0 [1.2]	12.4 [1.7]	-
	NE	7.3 [1.0]	9.1 [1.2]	9.5 [1.4]	88
	NO	7.5 [1.3]	8.7 [1.5]	9.1 [2.2]	-

Chapter 5

Conclusions and recommendations

onze vragen beantwoordden we met kijken
naar de langzame wereld om ons heen
…
we gingen zitten kijken naar deze prachtige
onverschilligheid van de wereld

Rutger Kopland *Toen ik dit zag*

In Chapter 1 four research questions have been formulated. Here I discuss the extend to which these questions have been addressed in this dissertation. Furthermore, a list of recommendations is given on how to further advance the science related to this dissertation.

5.1   Conclusions

1. **What model developments are necessary to integrate the main interactions and feedback mechanisms between the Greenland Ice Sheet and the Earth system in a model that simulates Earth system dynamics?**

   Since the Greenland Ice Sheet (GrIS) is a land-based ice sheet, the primary interactions and feedback mechanisms between the ice sheet and the Earth System happen through the interface between the terrestrial ice sheet surface and the atmosphere. Although uncertainty exists about processes from ice-ocean interactions and the way they contribute is not known yet, the net effect of ocean processes on the GrIS seems considerably smaller than the surface processes. In the coupling steps presented and used in this dissertation, most of the focus has been directed towards making the surface-ice coupling bi-directionally interactive.

   The technical integration of the Community Ice Sheet Model version 2 (CISM2) into the Community Earth System Model version 2 (CESM2) has four aspects. They are addressed in Chapter 2.

   (a) Physics-based Surface Energy Balance (SEB) and Surface Mass Balance (SMB) calculations on elevation classes in the land model, and SMB downscaled to the higher-resolution ice sheet grid.
   The SMB is computed based on snowfall, refreezing, sublimation and melt. The melt energy is derived from the SEB of net radiation and the turbulent and ground heat fluxes. Snow albedo is calculated for the visible and near-infrared bands accounting for vertically-resolved solar absorption, snow grain size evolution and impurities. The snow pack compaction into firn is simulated with prognostic density and pore space, considering the effects of snow mass overburden, metamorphism and enhanced wind-driven compaction.
   The Elevation Class (EC) method accounts for the vertical variation that is not resolved natively in variables of the SMB and SEB. This allows the model 1) to navigate between the high spatial resolution of the ice sheet model and the relatively coarse grid of the land and atmosphere models, and 2) to interactively represent the dynamically changing ice sheet topography in the SMB and SEB calculations. The glaciated fraction of each land grid cell is split into ECs based on ice sheet elevation provided by the ice sheet model. Near-surface temperature is downscaled from the land model grid-mean elevation to the EC-mean elevation using a uniform lapse rate of $6 \, \mathrm{K \, km^{-1}}$. Potential temperature,

specific humidity, air density, and surface pressure are downscaled assuming vertically uniform relative humidity. Further, longwave radiation downscaling is an option, and the grid cell partitioning of precipitation between rain and snow can be near-surface temperature dependent.

Remapping the SMB from the land model grid to the ice sheet model grid is done every year for synchronous coupling set-ups. To go from the land model grid to the ice sheet model grid, the SMB is bilinearly interpolated in the horizontal directions, and linearly in the vertical. A normalization factor is applied to the result of the trilinear interpolation in order to conserve mass, total accumulation area and total ablation area.

(b) Dynamic surface types in the land model to simulate ice sheet advances or retreats.

Each grid cell in the land model may consist of different land unit types, such as vegetated, urban, and glacier. The advance and retreat of the ice sheet margin is dynamically updated in the land model based on the ice sheet geometry simulated in the ice sheet model. With the updated ice sheet model geometry, the coupler recomputes the total glacier area, as well as the mean topographic height for each EC of the land domain that overlaps with the ice sheet domain. When the ice sheet retreats, the vegetation types that regrow on deglaciated land are determined by the input map where vegetated land units have a Plant Functional Type (PFT). The PFT underneath the GrIS currently by default is prescribed as bare ground. Finally, since vegetated columns have soil layers while glacier columns have subsurface ice layers, adjustments of the subsurface state are made to conserve water, energy, carbon and nitrogen content.

(c) Evolution of the land–atmosphere boundary with changing ice-sheet surface topography.

Changes in ice sheet geometry are communicated to the atmosphere model. Fields of surface elevation and sub-grid scale standard deviations of orography are calculated with the NCAR global model topography generation software for unstructured grids. These changed surface elevation fields are regridded and inserted in the atmospheric model as lower boundary conditions. The frequency of the topography updating is at the user's choice. For all simulations in this dissertation, the topographic updating was done every 10 simulation years.

(d) Fresh water forcing from the ice sheet model to the ocean model.

Ocean-ice sheet coupling is implemented one-way: meltwater runoff and ice discharge at outlet glaciers to the ocean is represented. Ocean thermal forcing to the calving fronts is not included in the model, nor is sub-shelf melt and circulation in ice shelf cavities.

With interactively evolving ice sheets, the fresh water forcing consists of surface runoff generated from non-refrozen melt and rainfall in land model and basal melt water and ice discharge generated in the ice sheet model. Surface runoff is routed to the ocean by the river runoff model based on gradients of

topography. Basal melt and ice discharge are brought from the source point in the ice sheet model to the ocean via nearest neighbor interpolation. .

The freshwater influx is treated as a salinity anomaly in the ocean model. Thermal corrections accounting for temperature differences between discharged ice or meltwater, and the ocean waters are not accounted for. The salinity anomaly from surface runoff is distributed over the first few ocean layers (typically three layers, or 30 m) with an estuary box model. Ice discharge is melted instantaneously, taking the energy for the phase change from the ocean surface heat flux. In order to avoid excess frazil growth from this heat extraction, the ice discharge flux is spread out horizontally over multiple ocean surface grid cells using a Gaussian distribution with a radius of 300 km. The calving flux is not distributed vertically within the ocean water column.

2. **Which processes are captured through the new ice sheet/climate model coupling?**

In other words, what is the gain from including the couplings indicated in 1)?

Ice sheet modelling is used to make projections of the ice sheet contributions to sea level rise. Earth system modelling is used to make climate change projections. Simulating ice sheet dynamics within an Earth system model requires accounting for ice sheet-climate interactions and feedbacks. The gains from implementing the coupling features as described in question (1) are: the ability to simultaneously simulate the ice-albedo feedback and the SMB-temperature feedback, and the ability to simulate the impacts of GrIS changes on the global climate. This is necessary in multi-century transient simulations where ice sheets are subject to mass change and the implicit assumption of ice sheet equilibrium (MB=0) does not hold.

Chapter 2 addresses this question with a demonstration that shows the functioning of the coupling features. We conclude that CESM2–CISM2 coupled over Greenland is able to simulate a transient climate between the pre-industrial steady-state state and a state with high levels of atmospheric CO_2 that includes the main interactions and feedback mechanisms between the GrIS and the Earth system. The method is to examine the flux exchanges and state updates that are made by the coupler between the different model components. The implemented coupling features can be demonstrated by comparing two different climate states. Alternatively, it is possible to demonstrate the coupling by comparing a simulation of CESM2–CISM2 to a simulation of CESM2 without interactive GrIS model (that is, without dynamic CISM2). However, some coupling features are incorporated in CESM2 and are difficult to completely switch off. Additionally, parts of the implemented coupling features that are explicitly solved in CESM2–CISM2 are parameterized in CESM2, such as the fresh water fluxes to the ocean. This would make the comparison un-

clear if we chose the second option. Therefore, we have chosen the first option.

We compare the mean climate state of the pre-industrial control simulation with a 20-year climatology from a transient simulation of an elevated atmospheric CO_2 scenario. The SMB becomes strongly negative in the high-CO_2 climate, as expected. The land model, that operates at a high temporal resolution, simulates a larger amplitude in the seasonal cycles of SMB and runoff. The ablation zones expand and the average Equilibrium Line Altitude (ELA) rises above 2000 m. Melt processes affect the surface albedo of the snow pack. This modifies the net shortwave radiation at the surface. The melt increases strongly at lower elevations. The ice sheet margin loses mass and thins, and retreats in some areas. Due to marginal thinning, the horizontal gradient of topography increases. In the ice sheet model, we see enhanced ice velocities from the accumulation zone to the ablation zone around the equilibrium line altitude. Regarding the fresh water flux to the ocean: the surface runoff from the land model increases due to increased surface melt. On the other hand, the retreat and thinning of the ice sheet margin reduces ice discharge that is produced in the ice sheet model.

Combining modelling of the global climate with snow and ice processes is key to capturing the governing interactions and feedback mechanisms, that allow for model studies into interactions of global and regional climate change and ice sheet mass loss rates, such as the studies in Chapter 3 and Chapter 4, that are addressed in questions (3) and (4).

3. **What estimates for 21st century GrIS mass loss does the coupled model provide for the SSP5-8.5 scenario?**

This question is discussed in Chapter 3.

The simulation with the coupled CESM2–CISM2 model ran for the historical period (1850-2014) and with the high-end SSP5-8.5 scenario (2015-2100). The simulated cumulative GrIS contribution to global mean sea level rise is 23 mm by 2050 and 109 mm by 2100. The global mean surface temperature is projected to increase with 5.4 K by 2100 w.r.t. the pre-industrial era, and the North Atlantic Meridional Overturning Circulation (NAMOC) strongly weakens. The mean GrIS mass loss rate in the last two decades of the 21st century is 2.7 mm sea level equivalent (SLE) year^{-1}. In the mass budget, the increased surface mass loss is partly offset by reduced ice discharge from margin thinning and the retreat of outlet glaciers. The relative contribution of the northern basins in the GrIS to sea level rise becomes larger during the second half of the 21st century, as surface runoff strongly increases.

There are several sources of uncertainty in this projection. Uncertainties include scenario uncertainty, model uncertainty and internal variability. Explicit

uncertainty quantification is not possible given that the study is based on one production simulation. Therefore, here we reflect qualitatively on the model uncertainty and biases as well as comparisons with other simulations as discussed in the thesis.

First, I assess the uncertainty in connection with the parameters in the SMB downscaling from the climate to the ice sheet model. The key parameters to consider when reflecting on uncertainty of the strength of the feedbacks are the temperature lapse rate, the longwave radiation lapse rate and the rain-snow repartitioning in the elevation class scheme of land model. The lapse rates redistribute the respective quantity within the grid cell's elevation classes. Additionally, the temperature lapse rate is a determining factor for the elevation classes' potential temperature, specific humidity, air density, and surface pressure. The rain-snow repartitioning regulates where in an ice sheet grid cell (i.e., at what elevations) precipitation falls as snow, and where it falls as rain.

The sensitivity of the SMB simulation to the temperature lapse rate has been studied for CESM1 by Sellevold et al. (2019). Adjustments to the rain-snow repartitioning and the longwave lapse rate where needed to constrain bias propagation into the ice sheet model from a wet bias in the atmosphere model. Partially coupled simulations were conducted to test and limit ice sheet expansion due to this excess precipitation. Following these test results, the rain-snow repartitioning parameter and the longwave radiation lapse rate have been modified in the coupled CESM2-CISM2 with respect to the out-of-the-box CESM2.

The albedo and the SMB are explicitly calculated in the land model as described in Chapter 2. The simulation of these has largely benefited from the introduction of the new firn/snow model. The parameter freedom in the firn/snow model, e.g., snow density of fresh fallen snow, wind-dependency of density, has been extensively tested by Van Kampenhout et al. (2017).

Second, a major limitation of our CESM2-CISM2 estimate is that the model does not include ocean forcing. The observed increase of ice discharge (Wood et al., 2018; Choi et al., 2021) is not simulated by CESM2-CISM2. However, the simulated decrease in ice discharge in response to SMB decline agrees with previous modelling work (Ruckamp et al., 2019; Vizcaino et al., 2015).

Third, the simulation starts with a spun-up GrIS that is too large by 12% in volume and 15% in area. The initialization bias originates from the coupled model spin-up to an equilibrium state. The advantage of a coupled model spin-up with respect to data assimilation methods is that spurious trends are reduced. The disadvantage in coupled spin-ups is a less realistic initial state than with data assimilation techniques. In our case it is an overestimation of the initial GrIS area and volume. Biases in the initial state impact the sensitivity of the model to climate change, as assessed in previous work for stand-alone

ice sheet models (Goelzer et al., 2018, 2020).

Finally, uncertainties in the simulated climate have a large impact on the sea level rise (SLR) projection. Change in SMB is the largest factor of GrIS mass loss in the studies of this thesis. CESM2 without interactive GrIS simulates the Greenland climate reasonably well in terms of large-scale dynamics, cloud properties, SMB and SEB (van Kampenhout et al., 2020). CESM2 SMB is overestimated when compared to the regional climate model RACMO (+ 60 Gt yr^{-1}), which is mainly due to the overestimation of precipitation in CESM2 over Greenland (van Kampenhout et al., 2020). In Chapter 3 we find CESM2-CISM2 has a higher present-day SMB (+ 181 Gt yr^{-1}) when compared to the CESM2-without interactive GrIS. This implies that the projected timing of GrIS response to warming may be delayed in this model due to biases of the initial topography.

4. **How does the GrIS respond as an integral part of the Earth system to elevated atmospheric CO$_2$ on a multicentennial timescale?**

This question is addressed in Chapter 4.

To systematically analyze the GrIS and broader Earth system response to elevated levels of atmospheric CO$_2$, the coupled CESM2–CISM2 model is forced with an idealized scenario of elevated atmospheric CO$_2$. In the scenario the CO$_2$ concentration starting at pre-industrial levels is increased by 1% per year until quadrupling after 140 years, followed by 210 years of steady 4xCO$_2$ forcing.

The response time of the GrIS to elevated atmospheric CO$_2$ lags behind the global mean temperature increase. One decade after CO$_2$-stabilization at four times the pre-industrial concentration, the global mean surface temperature has risen with 5.3 K relative to pre-industrial, and the GrIS contribution to global mean sea level rise is 107 mm. About 200 years of steady 4xCO$_2$ forcing later, the global mean surface temperature increased to around 8.5 K, and the total projected GrIS contribution to sea level rise is approximately 1,140 mm. The South-West drainage basin contributes the most to the sea level rise. The relative share of the northern basins to the GrIS total mass loss increases over the course of the simulation.

The initial source of extra melt energy is the increase in longwave radiation. Meltwater refreezes in the snowpack, and the accompanying latent heat releases increases the snow pack's energy content. This prepares the snow pack for complete melt, and the ablation areas to expand. The ablation areas expand sufficiently to trigger a large ice-albedo feedback. The net shortwave radiation at the surface increases. In the ablation zone, the summer sensible

heat flux adds to the melt energy due to an increased temperature gradient between the surface and the (warmer) ambient air. The latent heat flux further contributes to the melt via deposition. The additional net shortwave radiation is the primary source of the additional melt energy by the end of the 350-year simulation.

5.2   Recommendations

Recommendations for further model development

- Antarctica holds the largest potential to contribute to sea-level rise, and there is a large uncertainty about its stability. The next step of integrating ice sheet dynamics in CESM is to further expand the ice sheet – ocean coupling to allow coupling with marine-based ice sheets such as the AIS. This means developing and implementing new parameterizations for sub-shelf circulation and the ocean thermal forcing to compute shelf basal melt rates. Second, there is ongoing debate on the attribution of recent GrIS mass loss to ocean-ice and surface-ice interactions. Scientific findings depend on the considered period, however, it is clear that the contribution from ocean forcing is not trivial. Including ocean thermal forcing to the GrIS marine-terminating outlet glaciers will improve the representation of ice sheet-ocean interactions and help to gain insight in the partitioning between surface and dynamical mass losses. These processes are missing in the current model.

- On multicentennial timescales, the retreat of terrestrial ice sheets will allow for regrowth of local vegetation. This influences the local albedo. Currently the vegetation types as represented in the land model are static. A more advanced approach is to change the vegetation to be consistent with the evolving climate. To simulate such vegetation shifts would require a dynamic vegetation model.

Recommendations for additional simulations

- Simulations of ESMs without interactive ice sheets implicitly assume that is ice sheet mass balance is in equilibrium. However, this assumption of MB=0 cannot reasonably hold beyond a century, particularly in scenarios of highly elevated levels of greenhouse gasses and large projected mass loss. The coupled CESM2–CISM2 explicitly calculates the MB and therefore, it is not bound by this assumption. The results of the SSP5-8.5 scenario simulation that are presented this dissertation show no sign that the GrIS will reach a new equilibrium state in the current century. Extending the SSP5-8.5 simulation beyond 2100 allows to study the long-term effect of anthropogenic emissions on the GrIS within the Earth system. These type of studies can be highly informative in developing international climate mitigation strategies.

- The studies in this thesis have each been done with one production simulation, therefore the sources of uncertainty (scenario uncertainty, model uncertainty

and internal variability) can not be disentangled and quantified. Executing ensemble runs is a common practice in climate modelling to quantify internal climate variability from model variability. It is recommended to expand the suit of simulations with the new CESM2–CISM2 as well, because this will add robustness to the results. An important constraint to do ensemble simulations is the computational and time demands of running the fully coupled ESM: this is in the order of 3000 processor-hours for one simulated year and 20 model years per wall-clock day. It would be good to expand on the number of ensemble members of the SSP5-8.5 scenario. With limited resources, however, it is recommended to give priority to expand the suite of simulations with different scenario's and quantify scenario uncertainty, for example with the overshoot scenario SSP5-3.4OS that follows the high-emission rate of the SSP5-8.5 scenario until 2040, after which emissions sharply decline.

- Feedback mechanisms are complex to quantify. In Chapters 3 and 4, we have looked at how the GrIS responds to warming scenarios integrally within the Earth system. We have not been able to isolate how the changing GrIS by itself impacts the Earth system. Open questions remain, amongst others: how do changes in atmospheric circulation patterns arise from changes in ice sheet geometry, and to what degree do changes in ocean circulation arise from changes in the GrIS fresh water forcing. Answering these types of questions requires sensitivity simulations of the GrIS impact on Earth System, where certain factors are kept constant while others are allowed to change and interact. Technically, one could think of a simulation where the Earth system is exposed to increasing radiative forcing, but the GrIS coupling to the other model components (area, topography, calving and runoff fluxes etc.) is maintained on pre-industrial level.

Other recommendations/long-term developments

- Spinning-up an ESM that includes ice sheet dynamics requires making choices to balance several competing interests. The main interests are: 1) reaching equilibrium with limited model component drift for all model components individually and particularly those operating on long timescales, e.g., deep soil, deep ocean, and internal ice sheet structure, 2) reaching equilibrium for the ESM as a whole, 3) limiting computational demand, and 4) matching the present-day observations of the GrIS geometry. The initial conditions of the coupled model simulations in this dissertation are the result of a spin-up procedure described by Lofverstrom et al. (2020). The spun-up pre-industrial state showed relatively little residual drift, which is important in perturbation simulations as to attribute the climate signal to the perturbation. However, a shortcoming is that the GrIS volume is overestimated with 12% and the area with 15%. It is possible that this delays the projected timing of the GrIS response to warming. Therefore, it is worthwhile to investigate ways to improve the spin-up, that is, to decrease the overestimation of the GrIS area and volume as initial condition, while maintaining little model drift.

- Ice sheet behaviour operates on large timescales. The era of Earth observation is relatively short, with data from satellite missions available since the last few decades. Ocean sediments and ice cores given insight in the global climate of other epochs and paleoclimatology provides valuable insights into potential future Earth system evolutions. The fully coupled model that includes ice sheet dynamics presents the opportunity to simulate full glacial cycles. The possibility to connect different paleo proxies of sea level and temperature to a model reality that can be extended to present-day and future climates, including the simulation of historical climate transitions, is particularly interesting.

Bibliography

Abe-Ouchi, A., Saito, F., Kageyama, M., Braconnot, P., Harrison, S. P., Lambeck, K., Otto-Bliesner, B. L., Peltier, W. R., Tarasov, L., Peterschmitt, J.-Y., and Takahashi, K. (2015). Ice-sheet configuration in the CMIP5/PMIP3 Last Glacial Maximum experiments. *Geoscientific Model Development*, 8(11):3621–3637.

Adcroft, A., Anderson, W., Balaji, V., Blanton, C., Bushuk, M., Dufour, C. O., Dunne, J. P., Griffies, S. M., Hallberg, R., Harrison, M. J., Held, I. M., Jansen, M. F., John, J. G., Krasting, J. P., Langenhorst, A. R., Legg, S., Liang, Z., McHugh, C., Radhakrishnan, A., Reichl, B. G., Rosati, T., Samuels, B. L., Shao, A., Stouffer, R., Winton, M., Wittenberg, A. T., Xiang, B., Zadeh, N., and Zhang, R. (2019). The GFDL Global Ocean and Sea Ice Model OM4.0: Model Description and Simulation Features. *Journal of Advances in Modeling Earth Systems*, 11(10):3167–3211.

Agassiz, L. (1840). *Études sur les glaciers*. Neuchatel.

Alexander, P. M., LeGrande, A. N., Fischer, E., Tedesco, M., Fettweis, X., Kelley, M., Nowicki, S. M. J., and Schmidt, G. A. (2019). Simulated Greenland Surface Mass Balance in the GISS ModelE2 GCM: Role of the Ice Sheet Surface. *Journal of Geophysical Research: Earth Surface*, 124(3):750–765.

Andre, B., Kluzek, E., and Sacks, W. (2020). CLM5.0 User's Guide.

Aschwanden, A., Fahnestock, M. A., and Truffer, M. (2016). Complex Greenland outlet glacier flow captured. *Nat. Commun.*, 7:10524.

Aschwanden, A., Fahnestock, M. A., Truffer, M., Brinkerhoff, D. J., Hock, R., Khroulev, C., Mottram, R., and Khan, S. A. (2019). Contribution of the Greenland Ice Sheet to sea level over the next millennium. *Science Advances*, 5(6).

Auger, J. D., Birkel, S. D., Maasch, K. A., Mayewski, P. A., and Schuenemann, K. C. (2017). Examination of precipitation variability in southern Greenland. *Journal of Geophysical Research: Atmospheres*, 122(12):6202–6216.

Augustin, L., Barbante, C., Barnes, P. R., Barnola, J. M., Bigler, M., Castellano, E., Cattani, O., Chappellaz, J., Dahl-Jensen, D., Delmonte, B., et al. (2004). Eight glacial cycles from an Antarctic ice core. *Nature*, 429:623–628.

Bakker, P., Schmittner, A., Lenaerts, J. T. M., Abe-Ouchi, A., Bi, D., van den Broeke, M. R., Chan, W.-L., Hu, A., Beadling, R. L., Marsland, S. J., Mernild, S. H., Saenko, O. A., Swingedouw, D., Sullivan, A., and Yin, J. (2016). Fate of the Atlantic Meridional Overturning Circulation: Strong decline under continued warming and Greenland melting. *Geophysical Research Letters*, 43(23):12,252–12,260.

Bamber, J. L., Griggs, J. A., Hurkmans, R. T. W. L., Dowdeswell, J. A., Gogineni, S. P., Howat, I., Mouginot, J., Paden, J., Palmer, S., Rignot, E., and Steinhage, D. (2013). A new bed elevation dataset for Greenland. *The Cryosphere*, 7(2):499–510.

Bamber, J. L., Oppenheimer, M., Kopp, R. E., Aspinall, W. P., and Cooke, R. M. (2019). Ice sheet contributions to future sea-level rise from structured expert judgment. *Proceedings of the National Academy of Sciences*, 116(23):11195–11200.

Bauer, E. and Ganopolski, A. (2017). Comparison of surface mass balance of ice sheets simulated by positive-degree-day method and energy balance approach. *Climate of the Past*, 13(7):819–832.

Beljaars, A. C. M., Brown, A. R., and Wood, N. (2004). A new parametrization of turbulent orographic form drag. *Quarterly Journal of the Royal Meteorological Society*, 130(599):1327–1347.

Benn, D. I., Cowton, T., Todd, J., and Luckman, A. (2017). Glacier Calving in Greenland. *Current Climate Change Reports*, 3(4):282–290.

Bevis, M., Harig, C., Khan, S. A., Brown, A., Simons, F. J., Willis, M., Fettweis, X., van den Broeke, M. R., Madsen, F. B., Kendrick, E., Caccamise, D. J., van Dam, T., Knudsen, P., and Nylen, T. (2019). Accel-

erating changes in ice mass within Greenland, and the ice sheet's sensitivity to atmospheric forcing. *Proceedings of the National Academy of Sciences*, 116(6):1934–1939.

Bindschadler, R. A., Nowicki, S., Abe-Ouchi, A., Aschwanden, A., Choi, H., Fastook, J., Granzow, G., Greve, R., Gutowski, G., Herzfeld, U., and et al. (2013). Ice-sheet model sensitivities to environmental forcing and their use in projecting future sea level (the SeaRISE project). *Journal of Glaciology*, 59(214):195–224.

Bintanja, R. and Selten, F. M. (2014). Future increases in Arctic precipitation linked to local evaporation and sea-ice retreat. *Nature*, 509(7501):479–482.

Bintanja, R., van de Wal, R. S. W., and Oerlemans, J. (2005). Modelled atmospheric temperatures and global sea levels over the past million years. *Nature*, 437(7055):125–128.

Bintanja, R., van der Wiel, K., van der Linden, E. C., Reusen, J., Bogerd, L., Krikken, F., and Selten, F. M. (2020). Strong future increases in Arctic precipitation variability linked to poleward moisture transport. *Science Advances*, 6(7).

Blatter, H. (1995). Velocity and stress fields in grounded glaciers: a simple algorithm for including deviatoric stress gradients. *Journal of Glaciology*, 41(138):333–344.

Bogenschutz, P. a., Gettelman, A., Morrison, H., Larson, V. E., Craig, C., and Schanen, D. P. (2013). Higher-order turbulence closure and its impact on climate simulations in the community atmosphere model. *J. Clim.*, 26(23):9655–9676.

Bolch, T., Sandberg SÃžrensen, L., Simonsen, S. B., Molg, N., Machguth, H., Rastner, P., and Paul, F. (2013). Mass loss of Greenland's glaciers and ice caps 2003–2008 revealed from ICESat laser altimetry data. *Geophysical Research Letters*, 40(5):875–881.

Bonan, G. B., Levis, S., Kergoat, L., and Oleson, K. W. (2002). Landscapes as patches of plant functional types: An integrating concept for climate and ecosystem models. *Global Biogeochemical Cycles*, 16(2):5–1–5–23.

Bondzio, J. H., Morlighem, M., Seroussi, H., Wood, M. H., and Mouginot, J. (2018). Control of Ocean Temperature on Jakobshavn Isbrae's Present and Future Mass Loss. *Geophysical Research Letters*, 45(23):12,912–12,921.

Born, A., Imhof, M. A., and Stocker, T. F. (2019). An efficient surface energy–mass balance model for snow and ice. *The Cryosphere*, 13(5):1529–1546.

Bougamont, M., Bamber, J. L., Ridley, J. K., Gladstone, R. M., Greuell, W., Hanna, E., Payne, A. J., and Rutt, I. (2007). Impact of model physics on estimating the surface mass balance of the Greenland ice sheet. *Geophysical Research Letters*, 34(17).

Box, J. E., Fettweis, X., Stroeve, J. C., Tedesco, M., Hall, D. K., and Steffen, K. (2012). Greenland ice sheet albedo feedback: thermodynamics and atmospheric drivers. *The Cryosphere*, 6(4):821–839.

Braconnot, P, Otto-Bliesner, B., Harrison, S., Joussaume, S., Peterchmitt, J.-Y., Abe-Ouchi, A., Crucifix, M., Driesschaert, E., Fichefet, T., Hewitt, C. D., Kageyama, M., Kitoh, A., Laîné, A., Loutre, M.-F., Marti, O., Merkel, U., Ramstein, G., Valdes, P, Weber, S. L., Yu, Y., and Zhao, Y. (2007). Results of PMIP2 coupled simulations of the Mid-Holocene and Last Glacial Maximum; Part 1: experiments and large-scale features. *Climate of the Past*, 3(2):261–277.

Bromwich, D., Chen, Q., Li, Y., and Cullather, R. (1999). Precipitation over Greenland and its relation to the North Atlantic Oscillation. *Journal of Geophysical Research: Atmospheres*, 104(D18):22103–22115.

Calov, R., Beyer, S., Greve, R., Beckmann, J., Willeit, M., Kleiner, T., Rückamp, M., Humbert, A., and Ganopolski, A. (2018). Simulation of the future sea level contribution of Greenland with a new glacial system model. *The Cryosphere*, 12(10):3097–3121.

Charbit, S., Paillard, D., and Ramstein, G. (2008). Amount of CO_2 emissions irreversibly leading to the total melting of Greenland. *Geophysical Research Letters*, 35(12).

Chen, X., Zhang, X., Church, J. A., Watson, C. S., King, M. A., Monselesan, D., Legresy, B., and Harig, C. (2017). The increasing rate of global mean sea-level rise during 1993–2014. *Nature Climate Change*, 7(7):492–495.

Choi, Y., Morlighem, M., Rignot, E., and Wood, M. (2021). Ice dynamics will remain a primary driver of Greenland ice sheet mass loss over the next century. *Communications Earth & Environment*, 2(1):26.

Church, J., Clark, P, Cazenave, A., Gregory, J., Jevrejeva, S., Levermann, A., Merrifield, M., Milne, G., Nerem, R., Nunn, P, Payne, A., Pfeffer, W., Stammer, D., and Unnikrishnan, A. (2013). *Sea Level*

Change, book section 13, pages 1137–1216. Cambridge University Press, Cambridge, United Kingdom and New York, NY, USA.

Clark, P. U., Shakun, J. D., Marcott, S. A., Mix, A. C., Eby, M., Kulp, S., Levermann, A., Milne, G. A., Pfister, P. L., Santer, B. D., Schrag, D. P, Solomon, S., Stocker, T. F., Strauss, B. H., Weaver, A. J., Winkelmann, R., Archer, D., Bard, E., Goldner, A., Lambeck, K., Pierrehumbert, R. T., and Plattner, G.-K. (2016). Consequences of twenty-first-century policy for multi-millennial climate and sea-level change. *Nature Climate Change*, 6(4):360–369.

Crutzen, P. J. (2006). *The "Anthropocene"*, pages 13–18. Springer Berlin Heidelberg, Berlin, Heidelberg.

Cuffey, K. M. and Paterson, W. S. B. (2010). *The physics of glaciers*. Academic Press.

Curtis, K. J. and Schneider, A. (2011). Understanding the demographic implications of climate change: estimates of localized population predictions under future scenarios of sea-level rise. *Population and Environment*, 33(1):28–54.

Dahl-Jensen, D., Albert, M. R., Aldahan, A., Azuma, N., Balslev-Clausen, D., Baumgartner, M., Berggren, A. M., Bigler, M., Binder, T., Blunier, T., Bourgeois, J. C., Brook, E. J., Buchardt, S. L., Buizert, C., Capron, E., Chappellaz, J., Chung, J., Clausen, H. B., Cvijanovic, I., Davies, S. M., Ditlevsen, P., Eicher, O., Fischer, H., Fisher, D. A., Fleet, L. G., Gfeller, G., Gkinis, V, Gogineni, S., Goto-Azuma, K., Grinsted, A., Gudlaugsdottir, H., Guillevic, M., Hansen, S. B., Hansson, M., Hirabayashi, M., Hong, S., Hur, S. D., Huybrechts, P., Hvidberg, C. S., Iizuka, Y., Jenk, T., Johnsen, S. J., Jones, T. R., Jouzel, J., Karlsson, N. B., Kawamura, K., Keegan, K., Kettner, E., Kipfstuhl, S., Kjær, H. A., Koutnik, M., Kuramoto, T., Köhler, P., Laepple, T., Landais, A., Langen, P. L., Larsen, L. B., Leuenberger, D., Leuenberger, M., Leuschen, C., Li, J., Lipenkov, V., Martinerie, P., Maselli, O. J., Masson-Delmotte, V, McConnell, J. R., Miller, H., Mini, O., Miyamoto, A., Montagnat-Rentier, M., Mulvaney, R., Muscheler, R., Orsi, A. J., Paden, J., Panton, C., Pattyn, F., Petit, J. R., Pol, K., Popp, T., Possnert, G., Prié, F., Prokopiou, M., Quiquet, A., Rasmussen, S. O., Raynaud, D., Ren, J., Reutenauer, C., Ritz, C., Röckmann, T., Rosen, J. L., Rubino, M., Rybak, O., Samyn, D., Sapart, C. J., Schilt, A., Schmidt, A. M. Z., Schwander, J., Schüpbach, S., Seierstad, I., Severinghaus, J. P., Sheldon, S., Simonsen, S. B., Sjolte, J., Solgaard, A. M., Sowers, T., Sperlich, P., Steen-Larsen, H. C., Steffen, K., Steffensen, J. P., Steinhage, D., Stocker, T. F., Stowasser, C., Sturevik, A. S., Sturges, W. T., Sveinbjörnsdottir, A., Svensson, A., Tison, J. L., Uetake, J., Vallelonga, P., van de Wal, R. S. W., van der Wel, G., Vaughn, B. H., Vinther, B., Waddington, E., Wegner, A., Weikusat, I., White, J. W. C., Wilhelms, F., Winstrup, M., Witrant, E., Wolff, E. W., Xiao, C., Zheng, J., and community members, N. (2013). Eemian interglacial reconstructed from a Greenland folded ice core. *Nature*, 493(7433):489–494.

Dai, A., Luo, D., Song, M., and Liu, J. (2019). Arctic amplification is caused by sea-ice loss under increasing CO_2. *Nature Communications*, 10(1):121.

Danabasoglu, G. (2019a). NCAR CESM2 model output prepared for CMIP6 ISMIP6 1pctCO2to4x-withism. Version 20191022.

Danabasoglu, G. (2019b). NCAR CESM2 model output prepared for CMIP6 ISMIP6 piControl-withism. Version 20191022.

Danabasoglu, G., Bates, S. C., Briegleb, B. P., Jayne, S. R., Jochum, M., Large, W. G., Peacock, S., and Yeager, S. G. (2012). The CCSM4 Ocean Component. *Journal of Climate*, 25(5):1361–1389.

Danabasoglu, G., Lamarque, J.-F., Bacmeister, J., Bailey, D. A., DuVivier, A. K., Edwards, J., Emmons, L. K., Fasullo, J., Garcia, R., Gettelman, A., Hannay, C., Holland, M. M., Large, W. G., Lauritzen, P. H., Lawrence, D. M., Lenaerts, J. T. M., Lindsay, K., Lipscomb, W. H., Mills, M. J., Neale, R., Oleson, K. W., Otto-Bliesner, B., Phillips, A. S., Sacks, W., Tilmes, S., Van Kampenhout, L., Vertenstein, M., Bertini, A., Dennis, J., Deser, C., Fischer, C., Fox-Kemper, B., Kay, J. E., Kinnison, D., Kushner, P. J., Larson, V. E., Long, M. C., Mickelson, S., Moore, J. K., Nienhouse, E., Polvani, L., Rasch, P. J., and Strand, W. G. (2020). The Community Earth System Model Version 2 (CESM2). *Journal of Advances in Modeling Earth Systems*, 12(2).

Danielson, J. J. and Gesch, D. B. (2011). Global multi-resolution terrain elevation data 2010 (GMTED2010). Open File Rep. 2011-1073, US Geological Survey.

Day, J. J., Bamber, J. L., and Valdes, P. J. (2013). The Greenland Ice Sheet's surface mass balance in a seasonally sea ice-free Arctic. *Journal of Geophysical Research: Earth Surface*, 118(3):1533–1544.

Delhasse, A., Fettweis, X., Kittel, C., Amory, C., and Agosta, C. (2018). Brief communication: Impact of the recent atmospheric circulation change in summer on the future surface mass balance of the Greenland

Ice Sheet. *The Cryosphere*, 12(11):3409–3418.

Edwards, P. N. (2011). History of climate modeling. *WIREs Climate Change*, 2(1):128–139.

Edwards, T. L., Fettweis, X., Gagliardini, O., Gillet-Chaulet, F., Goelzer, H., Gregory, J. M., Hoffman, M., Huybrechts, P., Payne, A. J., Perego, M., Price, S., Quiquet, A., and Ritz, C. (2014a). Effect of uncertainty in surface mass balance-elevation feedback on projections of the future sea level contribution of the Greenland ice sheet. *The Cryosphere*, 8:195–208.

Edwards, T. L., Fettweis, X., Gagliardini, O., Gillet-Chaulet, F., Goelzer, H., Gregory, J. M., Hoffman, M., Huybrechts, P., Payne, A. J., Perego, M., Price, S., Quiquet, A., and Ritz, C. (2014b). Probabilistic parameterisation of the surface mass balance elevation feedback in regional climate model simulations of the Greenland ice sheet. *The Cryosphere*, 8(1):181–194.

Enderlin, E. M., Howat, I. M., Jeong, S., Noh, M.-J., Van Angelen, J. H., and Van den Broeke, M. R. (2014). An improved mass budget for the Greenland ice sheet. *Geophysical Research Letters*, 41(3):866–872.

Ettema, J., Van den Broeke, M. R., Van Meijgaard, E., and Van de Berg, W. J. (2010). Climate of the Greenland ice sheet using a high-resolution climate model Part 2: Near-surface climate and energy balance. *The Cryosphere*, 4(4):529–544.

Eyring, V., Bony, S., Meehl, G. A., Senior, C. A., Stevens, B., Stouffer, R. J., and Taylor, K. E. (2016). Overview of the Coupled Model Intercomparison Project Phase 6 (CMIP6) experimental design and organization. *Geoscientific Model Development*, 9(5):1937–1958.

Fettweis, X., Hofer, S., Krebs-Kanzow, U., Amory, C., Aoki, T., Berends, C. J., Born, A., Box, J. E., Delhasse, A., Fujita, K., Gierz, P., Goelzer, H., Hanna, E., Hashimoto, A., Huybrechts, P., Kapsch, M.-L., King, M. D., Kittel, C., Lang, C., Langen, P. L., Lenaerts, J. T. M., Liston, G. E., Lohmann, G., Mernild, S. H., Mikolajewicz, U., Modali, K., Mottram, R. H., Niwano, M., Noël, B., Ryan, J. C., Smith, A., Streffing, J., Tedesco, M., van de Berg, W. J., van den Broeke, M., van de Wal, R. S. W., van Kampenhout, L., Wilton, D., Wouters, B., Ziemen, F., and Zolles, T. (2020). GrSMBMIP: intercomparison of the modelled 1980–2012 surface mass balance over the Greenland Ice Sheet. *The Cryosphere*, 14(11):3935–3958.

Fischer, R., Nowicki, S., Kelley, M., and Schmidt, G. A. (2014). A system of conservative regridding for ice-atmosphere coupling in a General Circulation Model (GCM). *Geoscientific Model Development*, 7(3):883–907.

Flanner, M. G. and Zender, C. S. (2006). Linking snowpack microphysics and albedo evolution. *Journal of Geophysical Research: Atmospheres*, 111(D12).

Flanner, M. G., Zender, C. S., Randerson, J. T., and Rasch, P. J. (2007). Present-day climate forcing and response from black carbon in snow. *Journal of Geophysical Research: Atmospheres*, 112(D11).

Frajka-Williams, E., Ansorge, I. J., Baehr, J., Bryden, H. L., Chidichimo, M. P., Cunningham, S. A., Danabasoglu, G., Dong, S., Donohue, K. A., Elipot, S., Heimbach, P., Holliday, N. P., Hummels, R., Jackson, L. C., Karstensen, J., Lankhorst, M., Le Bras, I. A., Lozier, M. S., McDonagh, E. L., Meinen, C. S., Mercier, H., Moat, B. I., Perez, R. C., Piecuch, C. G., Rhein, M., Srokosz, M. A., Trenberth, K. E., Bacon, S., Forget, G., Goni, G., Kieke, D., Koelling, J., Lamont, T., McCarthy, G. D., Mertens, C., Send, U., Smeed, D. A., Speich, S., Van den Berg, M., Volkov, D., and Wilson, C. (2019). Atlantic Meridional Overturning Circulation: Observed Transport and Variability. *Frontiers in Marine Science*, 6:260.

Franco, B., Fettweis, X., and Erpicum, M. (2013). Future projections of the Greenland ice sheet energy balance driving the surface melt. *The Cryosphere*, 7(1):1–18.

Fürst, J. J., Goelzer, H., and Huybrechts, P. (2015). Ice-dynamic projections of the Greenland ice sheet in response to atmospheric and oceanic warming. *The Cryosphere*, 9(3):1039–1062.

Fyke, J. G., Sacks, W. J., and Lipscomb, W. H. (2014a). A technique for generating consistent ice sheet initial conditions for coupled ice sheet/climate models. *Geoscientific Model Development*, 7(3):1183–1195.

Fyke, J. G., Sergienko, O., Lofverstrom, M., Price, S., and Lenaerts, J. T. M. (2018). An Overview of Interactions and Feedbacks Between Ice Sheets and the Earth System. *Reviews of Geophysics*, 56(2):361–408.

Fyke, J. G., Vizcaino, M., and Lipscomb, W. H. (2014b). The pattern of anthropogenic signal emergence in Greenland Ice Sheet surface mass balance. *Geophysical Research Letters*, 41(16):6002–6008.

Fyke, J. G., Weaver, A. J., Pollard, D., Eby, M., Carter, L., and Mackintosh, A. (2011). A new coupled ice sheet/climate model: description and sensitivity to model physics under Eemian, Last Glacial Maxi-

mum, late Holocene and modern climate conditions. *Geoscientific Model Development*, 4(1):117–136.

Gettelman, A., Hannay, C., Bacmeister, J. T., Neale, R. B., Pendergrass, A. G., Danabasoglu, G., Lamarque, J.-F., Fasullo, J. T., Bailey, D. A., Lawrence, D. M., and Mills, M. J. (2019). High Climate Sensitivity in the Community Earth System Model Version 2 (CESM2). *Geophysical Research Letters*, 46(14):8329–8337.

Gettelman, A., Kay, J., and Shell, K. (2012). The evolution of climate sensitivity and climate feedbacks in the Community Atmosphere Model. *Journal of Climate*, 25(5):1453–1469.

Gettelman, A., Morrison, H., Santos, S., Bogenschutz, P., and Caldwell, P. M. (2015). Advanced Two-Moment Bulk Microphysics for Global Models. Part II: Global Model Solutions and Aerosol–Cloud Interactions*. *J. Clim.*, 28(3):1288–1307.

Goelzer, H., Huybrechts, P., Furst, J., Nick, F., Andersen, M., Edwards, T., Fettweis, X., Payne, A., and Shannon, S. (2013). Sensitivity of Greenland ice sheet projections to model formulations. *Journal of Glaciology*, 59(216):733–749.

Goelzer, H., Nowicki, S., Edwards, T., Beckley, M., Abe-Ouchi, A., Aschwanden, A., Calov, R., Gagliardini, O., Gillet-Chaulet, F., Golledge, N. R., Gregory, J., Greve, R., Humbert, A., Huybrechts, P., Kennedy, J. H., Larour, E., Lipscomb, W. H., Le clec'h, S., Lee, V., Morlighem, M., Pattyn, F., Payne, A. J., Rodehacke, C., Rückamp, M., Saito, F., Schlegel, N., Seroussi, H., Shepherd, A., Sun, S., van de Wal, R., and Ziemen, F. A. (2018). Design and results of the ice sheet model initialisation experiments initMIP-Greenland: an ISMIP6 intercomparison. *The Cryosphere*, 12(4):1433–1460.

Goelzer, H., Nowicki, S., Payne, A., Larour, E., Seroussi, H., Lipscomb, W. H., Gregory, J., Abe-Ouchi, A., Shepherd, A., Simon, E., Agosta, C., Alexander, P., Aschwanden, A., Barthel, A., Calov, R., Chambers, C., Choi, Y., Cuzzone, J., Dumas, C., Edwards, T., Felikson, D., Fettweis, X., Golledge, N. R., Greve, R., Humbert, A., Huybrechts, P., Le clec'h, S., Lee, V., Leguy, G., Little, C., Lowry, D. P., Morlighem, M., Nias, I., Quiquet, A., Rückamp, M., Schlegel, N.-J., Slater, D. A., Smith, R. S., Straneo, F., Tarasov, L., van de Wal, R., and van den Broeke, M. (2020). The future sea-level contribution of the Greenland ice sheet: a multi-model ensemble study of ISMIP6. *The Cryosphere*, 14(9):3071–3096.

Goelzer, H., Robinson, A., Seroussi, H., and Van de Wal, R. S. (2017). Recent Progress in Greenland Ice Sheet Modelling. *Current Climate Change Reports*, 3(4):291–302.

Goldberg, D. N. (2011). A variationally derived, depth-integrated approximation to a higher-order glaciological flow model. *Journal of Glaciology*, 57(201):157–170.

Golledge, N. R., Keller, E. D., Gomez, N., Naughten, K. A., Bernales, J., Trusel, L. D., and Edwards, T. L. (2019). Global environmental consequences of twenty-first-century ice-sheet melt. *Nature*, 566(7742):65–72.

Graversen, R. G., Drijfhout, S., Hazeleger, W., Van de Wal, R., Bintanja, R., and Helsen, M. (2011). Greenland's contribution to global sea-level rise by the end of the 21st century. *Climate Dynamics*, 37(7):1427–1442.

Gregory, J., Browne, O., Payne, A., Ridley, J., and Rutt, I. (2012). Modelling large-scale ice-sheet–climate interactions following glacial inception. *Climate of the Past*, 8:1565–1580.

Gregory, J. and Huybrechts, P. (2006). Ice-sheet contributions to future sea-level change. *Philosophical Transactions of the Royal Society A: Mathematical, Physical and Engineering Sciences*, 364(1844):1709–1732.

Gregory, J. M., George, S. E., and Smith, R. S. (2020). Large and irreversible future decline of the Greenland ice sheet. *The Cryosphere*, 14(12):4299–4322.

Gregory, J. M., Griffies, S. M., Hughes, C. W., Lowe, J. A., Church, J. A., Fukimori, I., Gomez, N., Kopp, R. E., Landerer, F., Cozannet, G. L., Ponte, R. M., Stammer, D., Tamisiea, M. E., and van de Wal, R. S. W. (2019). Concepts and Terminology for Sea Level: Mean, Variability and Change, Both Local and Global. *Surveys in Geophysics*, 40(6):1251–1289.

Gregory, J. M., Huybrechts, P., and Raper, S. C. B. (2004). Threatened loss of the Greenland ice-sheet. *Nature*, 428(6983):616–616.

Hanna, E., Cropper, T. E., Hall, R. J., and Cappelen, J. (2016). Greenland Blocking Index 1851–2015: a regional climate change signal. *International Journal of Climatology*, 36(15):4847–4861.

Hanna, E., Fettweis, X., and Hall, R. J. (2018). Brief communication: Recent changes in summer Greenland blocking captured by none of the CMIP5 models. *The Cryosphere*, 12(10):3287–3292.

Hanna, E., Pattyn, F., Navarro, F., Favier, V., Goelzer, H., den Broeke, M. R. V., Vizcaino, M., Whitehouse,

P. L., Ritz, C., Bulthuis, K., and Smith, B. (2020). Mass balance of the ice sheets and glaciers: Progress since AR5 and challenges. *Earth-Science Reviews*, 201:102976.

Hansen, J. E. and Sato, M. (2012). Paleoclimate implications for human-made climate change. In *Climate change*, pages 21–47. Springer.

Harper, J., Humphrey, N., Pfeffer, W. T., Brown, J., and Fettweis, X. (2012). Greenland ice-sheet contribution to sea-level rise buffered by meltwater storage in firn. *Nature*, 491(7423):240–243.

Hauer, M. E., Evans, J. M., and Mishra, D. R. (2016). Millions projected to be at risk from sea-level rise in the continental United States. *Nature Climate Change*, 6(7):691–695.

Held, I. M. and Soden, B. J. (2006). Robust Responses of the Hydrological Cycle to Global Warming. *Journal of Climate*, 19(21):5686 – 5699.

Helsen, M. M., Van de Wal, R. S. W., Reerink, T. J., Bintanja, R., Madsen, M. S., Yang, S., Li, Q., and Zhang, Q. (2017). On the importance of the albedo parameterization for the mass balance of the Greenland ice sheet in EC-Earth. *The Cryosphere*, 11(4):1949–1965.

Hermann, M., Box, J. E., Fausto, R. S., Colgan, W. T., Langen, P. L., Mottram, R., Wuite, J., Noel, B., Van den Broeke, M. R., and Van As, D. (2018). Application of PROMICE Q-Transect in Situ Accumulation and Ablation Measurements (2000-2017) to Constrain Mass Balance at the Southern Tip of the Greenland Ice Sheet. *Journal of Geophysical Research: Earth Surface*, 123(6):1235–1256.

Holland, M. M. and Landrum, L. (2015). Factors affecting projected Arctic surface shortwave heating and albedo change in coupled climate models. *Philosophical Transactions of the Royal Society A: Mathematical, Physical and Engineering Sciences*, 373(2045):20140162.

Hu, A., Meehl, G. A., Han, W., and Yin, J. (2009). Transient response of the MOC and climate to potential melting of the Greenland Ice Sheet in the 21st century. *Geophysical Research Letters*, 36(10).

Hunke, E., Lipscomb, W., Jones, P., Turner, A., Jeffery, N., and Elliott, S. (2017). CICE, The Los Alamos Sea Ice Model, Version 00.

Huybrechts, P. (1992). The Antarctic ice sheet and environmental change: a three-dimensional modelling study. *Berichte zur Polarforschung*, 99.

Huybrechts, P., Goelzer, H., Janssens, I., Driesschaert, E., Fichefet, T., Goosse, H., and Loutre, M.-F. (2011). Response of the Greenland and Antarctic Ice Sheets to Multi-Millennial Greenhouse Warming in the Earth System Model of Intermediate Complexity LOVECLIM. *Surveys in Geophysics*, 32(4):397–416.

Izeboud, M., Lhermitte, S., Van Tricht, K., Lenaerts, J. T. M., Van Lipzig, N. P. M., and Wever, N. (2020). The Spatiotemporal Variability of Cloud Radiative Effects on the Greenland Ice Sheet Surface Mass Balance. *Geophysical Research Letters*, 47(12):e2020GL087315. e2020GL087315 10.1029/2020GL087315.

Joughin, I., Alley, R. B., and Holland, D. M. (2012). Ice-Sheet Response to Oceanic Forcing. *Science*, 338(6111):1172–1176.

Joughin, I., Smith, B., Howat, I., and Scambos, T. (2015). MEaSUREs Greenland Ice Sheet Velocity Map from InSAR Data, Version 2.

Joughin, I., Smith, B., Howat, I., Scambos, T., and Moon, T. (2010). Greenland flow variability from ice-sheet-wide velocity mapping. *Journal of Glaciology*, 56(197):415–430.

Kaplan, J. O., Bigelow, N. H., Prentice, I. C., Harrison, S. P., Bartlein, P. J., Christensen, T. R., Cramer, W., Matveyeva, N. V., McGuire, A. D., Murray, D. F., Razzhivin, V. Y., Smith, B., Walker, D. A., Anderson, P. M., Andreev, A. A., Brubaker, L. B., Edwards, M. E., and Lozhkin, A. V. (2003). Climate change and Arctic ecosystems: 2. Modeling, paleodata-model comparisons, and future projections. *Journal of Geophysical Research: Atmospheres*, 108(D19).

Kay, J. E., Holland, M. M., Bitz, C. M., Blanchard-Wrigglesworth, E., Gettelman, A., Conley, A., and Bailey, D. (2012). The influence of local feedbacks and northward heat transport on the equilibrium Arctic climate response to increased greenhouse gas forcing. *Journal of Climate*, 25(16):5433–5450.

Khazendar, A., Fenty, I. G., Carroll, D., Gardner, A., Lee, C. M., Fukumori, I., Wang, O., Zhang, H., Seroussi, H., Moller, D., Noël, B. P. Y., Van den Broeke, M. R., Dinardo, S., and Willis, J. (2019). Interruption of two decades of Jakobshavn Isbrae acceleration and thinning as regional ocean cools. *Nature Geoscience*, 12(4):277–283.

King, M. D., Howat, I. M., Candela, S. G., Noh, M. J., Jeong, S., Noël, B. P. Y., van den Broeke, M. R., Wouters, B., and Negrete, A. (2020). Dynamic ice loss from the Greenland Ice Sheet driven by sustained glacier retreat. *Communications Earth & Environment*, 1(1):1.

Krapp, M., Robinson, A., and Ganopolski, A. (2017). SEMIC: an efficient surface energy and mass balance model applied to the Greenland ice sheet. *The Cryosphere*, 11(4):1519–1535.

Lauritzen, P. H., Bacmeister, J. T., Callaghan, P. F., and Taylor, M. A. (2015). NCAR_Topo (v1.0): NCAR global model topography generation software for unstructured grids. *Geoscientific Model Development*, 8(12):3975–3986.

Lawrence, D., Fisher, R., Koven, C., Oleson, K., Swenson, S., Vertenstein, M., Andre, B., Bonan, G., Ghimire, B., Van Kampenhout, L., Kennedy, D., Kluzek, E., Knox, R., Lawrence, P., Li, F., Li, H., Lombardozzi, D., Lu, Y., Perket, J., Riley, W., Sacks, W., Shi, M., Wieder, W., Xu, C., Ali, A., Badger, A., Bisht, G., Broxton, P., Brunke, M., Buzan, J., Clark, M., Craig, T., Dahlin, K., Drewniak, B., Emmons, L., Fisher, J., Flanner, M., Gentine, P., Lenaerts, J., Levis, S., Leung, L. R., Lipscomb, W., Pelletier, J., Ricciuto, D. M., Sanderson, B., Shuman, J., Slater, A., Subin, Z., Tang, J., Tawfik, A., Thomas, Q., Tilmes, S., Vitt, F., and Zeng, X. (2020). CLM5 Documentation.

Lawrence, D. M., Fisher, R. A., Koven, C. D., Oleson, K. W., Swenson, S. C., Bonan, G., Collier, N., Ghimire, B., Van Kampenhout, L., Kennedy, D., Kluzek, E., Lawrence, P. J., Li, F., Li, H., Lombardozzi, D., Riley, W. J., Sacks, W. J., Shi, M., Vertenstein, M., Wieder, W. R., Xu, C., Ali, A. A., Badger, A. M., Bisht, G., Van den Broeke, M., Brunke, M. A., Burns, S. P., Buzan, J., Clark, M., Craig, A., Dahlin, K., Drewniak, B., Fisher, J. B., Flanner, M., Fox, A. M., Gentine, P., Hoffman, F., Keppel-Aleks, G., Knox, R., Kumar, S., Lenaerts, J., Leung, L. R., Lipscomb, W. H., Lu, Y., Pandey, A., Pelletier, J. D., Perket, J., Randerson, J. T., Ricciuto, D. M., Sanderson, B. M., Slater, A., Subin, Z. M., Tang, J., Thomas, R. Q., Val Martin, M., and Zeng, X. (2019). The Community Land Model version 5: Description of new features, benchmarking, and impact of forcing uncertainty. *Journal of Advances in Modeling Earth Systems*, n/a(n/a).

Le clec'h, S., Charbit, S., Quiquet, A., Fettweis, X., Dumas, C., Kageyama, M., Wyard, C., and Ritz, C. (2019). Assessment of the Greenland ice sheet–atmosphere feedbacks for the next century with a regional atmospheric model coupled to an ice sheet model. *The Cryosphere*, 13(1):373–395.

Leguy, G., Lipscomb, W., and Sacks, W. (2018). *CESM Land Ice Documentation and User Guide*.

Leguy, G. R., Lipscomb, W. H., and Asay-Davis, X. S. (2020). Marine ice-sheet experiments with the Community Ice Sheet Model. *The Cryosphere Discussions*, 2020:1–33.

Lenaerts, J. T. M., Gettelman, A., Van Tricht, K., van Kampenhout, L., and Miller, N. B. (2020). Impact of Cloud Physics on the Greenland Ice Sheet Near-Surface Climate: A Study With the Community Atmosphere Model. *Journal of Geophysical Research: Atmospheres*, 125(7).

Lenaerts, J. T. M., Le Bars, D., Van Kampenhout, L., Vizcaino, M., Enderlin, E. M., and Van den Broeke, M. R. (2015). Representing Greenland ice sheet freshwater fluxes in climate models. *Geophysical Research Letters*, 42(15):6373–6381.

Lenaerts, J. T. M., van den Broeke, M. R., van Angelen, J. H., van Meijgaard, E., and Déry, S. J. (2012). Drifting snow climate of the Greenland ice sheet: a study with a regional climate model. *The Cryosphere*, 6(4):891–899.

Levermann, A., Clark, P. U., Marzeion, B., Milne, G. A., Pollard, D., Radic, V., and Robinson, A. (2013). The multimillennial sea-level commitment of global warming. *Proceedings of the National Academy of Sciences*, 110(34):13745–13750.

Lewis, G., Osterberg, E., Hawley, R., Whitmore, B., Marshall, H. P., and Box, J. (2017). Regional Greenland accumulation variability from Operation IceBridge airborne accumulation radar. *The Cryosphere*, 11(2):773–788.

Li, H.-Y., Leung, L. R., Getirana, A., Huang, M., Wu, H., Xu, Y., Guo, J., and Voisin, N. (2015). Evaluating Global Streamflow Simulations by a Physically Based Routing Model Coupled with the Community Land Model. *Journal of Hydrometeorology*, 16(2):948–971.

Li, Y. and Flanner, M. (2018). Investigating the impact of aerosol deposition on snowmelt over the Greenland Ice Sheet using a large-ensemble kernel. *Atmospheric Chemistry and Physics*, 18(21):16005–16018.

Liakka, J., Nilsson, J., and Löfverström, M. (2012). Interactions between stationary waves and ice sheets: linear versus nonlinear atmospheric response. *Climate Dynamics*, 38(5):1249–1262.

Lin, S.-J. and Rood, R. B. (1997). An explicit flux-form semi-lagrangian shallow-water model on the sphere. *Quarterly Journal of the Royal Meteorological Society*, 123(544):2477–2498.

Lipscomb, W. H., Fyke, J. G., Vizcaino, M., Sacks, W. J., Wolfe, J., Vertenstein, M., Craig, A., Kluzek, E., and Lawrence, D. M. (2013). Implementation and Initial Evaluation of the Glimmer Community Ice

Sheet Model in the Community Earth System Model. *Journal of Climate*, 26(19):7352–7371.

Lipscomb, W. H., Price, S. F., Hoffman, M. J., Leguy, G. R., Bennett, A. R., Bradley, S. L., Evans, K. J., Fyke, J. G., Kennedy, J. H., Perego, M., Ranken, D. M., Sacks, W. J., Salinger, A. G., Vargo, L. J., and Worley, P. H. (2019). Description and evaluation of the Community Ice Sheet Model (CISM) v2.1. *Geoscientific Model Development*, 12(1):387–424.

Liu, X., Ma, P.-L., Wang, H., Tilmes, S., Singh, B., Easter, R. C., Ghan, S. J., and Rasch, P. J. (2015). Description and evaluation of a new 4-mode version of Modal Aerosol Module (MAM4) within version 5.3 of the Community Atmosphere Model. *Geosci. Model Dev. Discuss.*, 8(9):8341–8386.

Lofverstrom, M., Fyke, J. G., Thayer-Calder, K., Muntjewerf, L., Vizcaino, M., Sacks, W. J., Lipscomb, W. H., Otto-Bliesner, B. L., and Bradley, S. L. (2020). An Efficient Ice Sheet/Earth System Model Spin-up Procedure for CESM2-CISM2: Description, Evaluation, and Broader Applicability. *Journal of Advances in Modeling Earth Systems*, 12(8).

Lofverstrom, M. and Liakka, J. (2018). The influence of atmospheric grid resolution in a climate model-forced ice sheet simulation. *The Cryosphere*, 12(4):1499–1510.

Lofverstrom, M., Liakka, J., and Kleman, J. (2015). The North American Cordilleraâ - An Impediment to Growing the Continent-Wide Laurentide Ice Sheet. *Journal of Climate*, 28(23):9433–9450.

Lüthi, D., Le Floch, M., Bereiter, B., Blunier, T., Barnola, J.-M., Siegenthaler, U., Raynaud, D., Jouzel, J., Fischer, H., Kawamura, K., and Stocker, T. F. (2008). High-resolution carbon dioxide concentration record 650,000–800,000 years before present. *Nature*, 453(7193):379–382.

MacAyeal, D. R. (1989). Large-scale ice flow over a viscous basal sediment: Theory and application to ice stream B, Antarctica. *Journal of Geophysical Research: Solid Earth*, 94(B4):4071–4087.

Masson-Delmotte, V., Zhai, P., Pirani, A., Connors, S., Péan, C., Berger, S., Caud, N., Chen, Y., Goldfarb, L., Gomis, M., Huang, M., Leitzell, K., Lonnoy, E., Matthews, J., Maycock, T., Waterfield, T., Yelekçi, O., Yu, R., and Zhou, B., editors (2021). *Climate Change 2021: The Physical Science Basis. Contribution of Working Group I to the Sixth Assessment Report of the Intergovernmental Panel on Climate Change*. Cambridge University Press.

Masson-Delmotte, V., Zhai, P., Pörtner, H. O., Roberts, D., Skea, J., Shukla, P., Pirani, A., Moufouma-Okia, W., Péan, C., Pidcock, R., Connors, S., Matthews, J. B. R., Chen, Y., Zhou, X., Gomis, M., Lonnoy, E., Maycock, T., Tignor, M., and Waterfield, T. (2018). *Summary for Policymakers*, book section Summary for Policymakers. World Meteorological Organization.

McLeod, J. T. and Mote, T. L. (2016). Linking interannual variability in extreme Greenland blocking episodes to the recent increase in summer melting across the Greenland ice sheet. *International Journal of Climatology*, 36(3):1484–1499.

Meccia, V. L. and Mikolajewicz, U. (2018). Interactive ocean bathymetry and coastlines for simulating the last deglaciation with the Max Planck Institute Earth System Model (MPI-ESM-v1.2). *Geoscientific Model Development*, 11(11):4677–4692.

Meehl, G. A., Boer, G. J., Covey, C., Latif, M., and Stouffer, R. J. (2000). The Coupled Model Intercomparison Project (CMIP). *Bulletin of the American Meteorological Society*, 81(2):313–318.

Mernild, S. H., Hanna, E., McConnell, J. R., Sigl, M., Beckerman, A. P., Yde, J. C., Cappelen, J., Malmros, J. K., and Steffen, K. (2015). Greenland precipitation trends in a long-term instrumental climate context (1890-2012): evaluation of coastal and ice core records. *International Journal of Climatology*, 35(2):303–320.

Mikolajewicz, U., Vizcaino, M., Jungclaus, J., and Schurgers, G. (2007). Effect of ice sheet interactions in anthropogenic climate change simulations. *Geophysical Research Letters*, 34(18).

Moon, T., Ahlstrøm, A., Goelzer, H., Lipscomb, W., and Nowicki, S. (2018). Rising Oceans Guaranteed: Arctic Land Ice Loss and Sea Level Rise. *Current Climate Change Reports*, 4(3):211–222.

Morland, L. (1987). Unconfined ice-shelf flow. In *Dynamics of the West Antarctic Ice Sheet*, pages 99–116. Springer.

Morland, L. and Johnson, I. (1980). Steady motion of ice sheets. *Journal of Glaciology*, 25(92):229–246.

Morland, L. and Smith, G. (1984). Influence of non-uniform temperature distribution on the steady motion of ice sheets. *Journal of Fluid Mechanics*, 140:113–133.

Morlighem, M., Rignot, E., Mouginot, J., Seroussi, H., and E., L. (2014). Deeply incised submarine glacial valleys beneath the Greenland Ice Sheet. *Nature Geoscience*, 7:418–422.

Morlighem, M., Williams, C. N., Rignot, E., An, L., Arndt, J. E., Bamber, J. L., Catania, G., Chauche, N., Dowdeswell, J. A., Dorschel, B., Fenty, I., Hogan, K., Howat, I., Hubbard, A., Jakobsson, M., Jordan, T. M., Kjeldsen, K. K., Millan, R., Mayer, L., Mouginot, J., Noël, B. P. Y., O'Cofaigh, C., Palmer, S., Rysgaard, S., Seroussi, H., Siegert, M. J., Slabon, P., Straneo, F., Van den Broeke, M. R., Weinrebe, W., Wood, M., and Zinglersen, K. B. (2017). BedMachine v3: Complete Bed Topography and Ocean Bathymetry Mapping of Greenland From Multibeam Echo Sounding Combined With Mass Conservation. *Geophysical Research Letters*, 44(21):11,051–11,061.

Muntjewerf, L., Petrini, M., Vizcaino, M., Ernani da Silva, C., Sellevold, R., Scherrenberg, M. D. W., Thayer-Calder, K., Bradley, S. L., Lenaerts, J. T. M., Lipscomb, W. H., and Lofverstrom, M. (2020a). Greenland Ice Sheet Contribution to 21st Century Sea Level Rise as Simulated by the Coupled CESM2.1–CISM2.1. *Geophysical Research Letters*, 47(9).

Muntjewerf, L., Sacks, W. J., Lofverstrom, M., Fyke, J., Lipscomb, W. H., Ernani da Silva, C., Vizcaino, M., Thayer-Calder, K., Lenaerts, J. T. M., and Sellevold, R. (2021). Description and Demonstration of the Coupled Community Earth System Model v2 - Community Ice Sheet Model v2 (CESM2-CISM2). *Journal of Advances in Modeling Earth Systems*, 13(6).

Muntjewerf, L., Sellevold, R., Vizcaino, M., Ernani da Silva, C., Petrini, M., Thayer-Calder, K., Scherrenberg, M. D. W., Bradley, S. L., Fyke, J., Lipscomb, W. H., Lofverstrom, M., and Sacks, W. J. (2020b). Accelerated Greenland ice sheet mass loss under high greenhouse gas forcing as simulated by the coupled CESM2.1–CISM2.1. *Journal of Advances in Modeling Earth Systems*, 12(10).

Neumann, B., Vafeidis, A. T., Zimmermann, J., and Nicholls, R. J. (2015). Future Coastal Population Growth and Exposure to Sea-Level Rise and Coastal Flooding - A Global Assessment. *PLOS ONE*, 10(3):1–34.

Nicholls, R. J., Marinova, N., Lowe, J. A., Brown, S., Vellinga, P., de Gusmao, D., Hinkel, J., and Tol, R. S. J. (2011). Sea-level rise and its possible impacts given a "beyond 4°C world" in the twenty-first century. *Philosophical Transactions of the Royal Society A: Mathematical, Physical and Engineering Sciences*, 369(1934):161–181.

Nick, F. M., Vieli, A., Andersen, M. L., Joughin, I., Payne, A., Edwards, T. L., Pattyn, F., and Van de Wal, R. S. W. (2013). Future sea-level rise from Greenland's main outlet glaciers in a warming climate. *Nature*, 497(7448):235–238.

Noël, B., Van de Berg, W. J., Lhermitte, S., and Van den Broeke, M. R. (2019). Rapid ablation zone expansion amplifies north Greenland mass loss. *Science Advances*, 5(9).

Noël, B., Van de Berg, W. J., Lhermitte, S., Wouters, B., Machguth, H., Howat, I., Citterio, M., Moholdt, G., Lenaerts, J. T. M., and Van den Broeke, M. R. (2017). A tipping point in refreezing accelerates mass loss of Greenland's glaciers and ice caps. *Nature Communications*, 8(1):14730.

Noël, B., Van de Berg, W. J., Van Wessem, J. M., Van Meijgaard, E., Van As, D., Lenaerts, J. T. M., Lhermitte, S., Kuipers Munneke, P., Smeets, C. J. P. P., Van Ulft, L. H., Van de Wal, R. S. W., and Van den Broeke, M. R. (2018). Modelling the climate and surface mass balance of polar ice sheets using RACMO2 – Part 1: Greenland (1958–2016). *The Cryosphere*, 12(3):811–831.

Noël, B., Van Kampenhout, L., Van de Berg, W. J., Lenaerts, J. T. M., Wouters, B., and Van den Broeke, M. R. (2019). Brief communication: CESM2 climate forcing (1950–2014) yields realistic Greenland ice sheet surface mass balance. *The Cryosphere Discussions*, 2019:1–17.

Nowicki, S. M. J., Payne, A., Larour, E., Seroussi, H., Goelzer, H., Lipscomb, W., Gregory, J., Abe-Ouchi, A., and Shepherd, A. (2016). Ice Sheet Model Intercomparison Project (ISMIP6) contribution to CMIP6. *Geoscientific Model Development*, 9(12):4521–4545.

Nye, J. F. (1963). On the Theory of the Advance and Retreat of Glaciers. *Geophysical Journal of the Royal Astronomical Society*, 7(4):431–456.

Oerlemans, J. (1981). Some basic experiments with a vertically-integrated ice sheet model. *Tellus*, 33:1–11.

O'Neill, B. C., Tebaldi, C., Van Vuuren, D. P., Eyring, V., Friedlingstein, P., Hurtt, G., Knutti, R., Kriegler, E., Lamarque, J.-F., Lowe, J., Meehl, G. A., Moss, R., Riahi, K., and Sanderson, B. M. (2016). The Scenario Model Intercomparison Project (ScenarioMIP) for CMIP6. *Geoscientific Model Development*, 9(9):3461–3482.

Pattyn, F. (2003). A new three-dimensional higher-order thermomechanical ice sheet model: Basic sen-

sitivity, ice stream development, and ice flow across subglacial lakes. *Journal of Geophysical Research: Solid Earth*, 108(B8).

Pollard, D. (2010). A retrospective look at coupled ice sheet–climate modeling. *Climatic Change*, 100(1):173–194.

Pollard, D., Muszynski, I., Schneider, S. H., and Thompson, S. L. (1990). Asynchronous Coupling of Ice-Sheet and Atmospheric Forcing Models. *Annals of Glaciology*, 14:247–251.

Price, S. F., Payne, A. J., Howat, I. M., and Smith, B. E. (2011). Committed sea-level rise for the next century from Greenland ice sheet dynamics during the past decade. *Proceedings of the National Academy of Sciences*, 108(22):8978–8983.

Rae, J. G. L., Adalgeirsdottirr, G., Edwards, T. L., Fettweis, X., Gregory, J. M., Hewitt, H. T., Lowe, J. A., Lucas-Picher, P., Mottram, R. H., Payne, A. J., Ridley, J. K., Shannon, S. R., Van de Berg, W. J., Van de Wal, R. S. W., and Van den Broeke, M. R. (2012). Greenland ice sheet surface mass balance: evaluating simulations and making projections with regional climate models. *The Cryosphere*, 6(6):1275–1294.

Ran, J., Vizcaino, M., Ditmar, P., Van den Broeke, M. R., Moon, T., Steger, C. R., Enderlin, E. M., Wouters, B., Noël, B., Reijmer, C. H., Klees, R., Zhong, M., Liu, L., and Fettweis, X. (2018). Seasonal mass variations show timing and magnitude of meltwater storage in the Greenland Ice Sheet. *The Cryosphere*, 12(9):2981–2999.

Ridley, J., Gregory, J. M., Huybrechts, P., and Lowe, J. (2010). Thresholds for irreversible decline of the Greenland ice sheet. *Climate Dynamics*, 35(6):1049–1057.

Ridley, J. K., Huybrechts, P., Gregory, J. M., and Lowe, J. A. (2005). Elimination of the Greenland Ice Sheet in a High CO_2 Climate. *Journal of Climate*, 18(17):3409–3427.

Rignot, E. and Mouginot, J. (2012). Ice flow in Greenland for the international polar year 2008–2009. *Geophysical Research Letters*, 39(11).

Robinson, A., Calov, R., and Ganopolski, A. (2012). Multistability and critical thresholds of the Greenland ice sheet. *Nature Climate Change*, 2(6):429–432.

Rombouts, J. and Ghil, M. (2015). Oscillations in a simple climate-vegetation model. *Nonlinear Processes in Geophysics*, 22(3):275–288.

Ruckamp, M., Greve, R., and Humbert, A. (2019). Comparative simulations of the evolution of the Greenland ice sheet under simplified Paris Agreement scenarios with the models SICOPOLIS and ISSM. *Polar Science*, 21:14 – 25. ISAR-5/ Fifth International Symposium on Arctic Research.

Rugenstein, M., Bloch-Johnson, J., Abe-Ouchi, A., Andrews, T., Beyerle, U., Cao, L., Chadha, T., Danabasoglu, G., Dufresne, J.-L., Duan, L., Foujols, M.-A., Frölicher, T., Geoffroy, O., Gregory, J., Knutti, R., Li, C., Marzocchi, A., Mauritsen, T., Menary, M., Moyer, E., Nazarenko, L., Paynter, D., Saint-Martin, D., Schmidt, G. A., Yamamoto, A., and Yang, S. (2020). LongRunMIP: Motivation and Design for a Large Collection of Millennial-Length AOGCM Simulations. *Bulletin of the American Meteorological Society*, 100(12):2551–2570.

Rutt, I., Hagdorn, M., Hulton, N., and Payne, A. (2009). The Glimmer community ice sheet model. *J. Geophys. Res.*, 114:F02004.

Rybak, O., Volodin, E., Morozova, P., and Nevecherja, A. (2018). Incorporation of ice sheet models into an Earth system model: Focus on methodology of coupling. *Journal of Earth System Science*, 127(2):28.

Schrama, E. J. O., Wouters, B., and Rietbroek, R. (2014). A mascon approach to assess ice sheet and glacier mass balances and their uncertainties from GRACE data. *Journal of Geophysical Research: Solid Earth*, 119(7):6048–6066.

Schuenemann, K. C. and Cassano, J. J. (2010). Changes in synoptic weather patterns and Greenland precipitation in the 20th and 21st centuries: 2. Analysis of 21st century atmospheric changes using self-organizing maps. *Journal of Geophysical Research: Atmospheres*, 115(D5).

Scinocca, J. F. and McFarlane, N. A. (2000). The parametrization of drag induced by stratified flow over anisotropic orography. *Quarterly Journal of the Royal Meteorological Society*, 126(568):2353–2393.

Sellevold, R., Van Kampenhout, L., Lenaerts, J. T. M., Noël, B., Lipscomb, W. H., and Vizcaino, M. (2019). Surface mass balance downscaling through elevation classes in an Earth System Model: analysis, evaluation and impacts on the simulated climate. *The Cryosphere Discussions*, 2019:1–25.

Sellevold, R. and Vizcaino, M. (2020). Global Warming Threshold and Mechanisms for Accelerated Greenland Ice Sheet Surface Mass Loss. *Journal of Advances in Modeling Earth Systems*, 12(9).

Shepherd, A., Ivins, E., Rignot, E., Smith, B., Van den Broeke, M., Velicogna, I., Whitehouse, P., Briggs, K., Joughin, I., Krinner, G., Nowicki, S., Payne, T., Scambos, T., Schlegel, N., Geruo, A., Agosta, C., Ahlstrøm, A., Babonis, G., Barletta, V. R., Bjørk, A. A., Blazquez, A., Bonin, J., Colgan, W., Csatho, B., Cullather, R., Engdahl, M. E., Felikson, D., Fettweis, X., Forsberg, R., Hogg, A. E., Gallee, H., Gardner, A., Gilbert, L., Gourmelen, N., Groh, A., Gunter, B., Hanna, E., Harig, C., Helm, V, Horvath, A., Horwath, M., Khan, S., Kjeldsen, K. K., Konrad, H., Langen, P. L., Lecavalier, B., Loomis, B., Luthcke, S., McMillan, M., Melini, D., Mernild, S., Mohajerani, Y., Moore, P., Mottram, R., Mouginot, J., Moyano, G., Muir, A., Nagler, T., Nield, G., Nilsson, J., Noël, B., Otosaka, I., Pattle, M. E., Peltier, W. R., Pie, N., Rietbroek, R., Rott, H., Sørensen, L. S., Sasgen, I., Save, H., Scheuchl, B., Schrama, E., Schröder, L., Seo, K.-W., Simonsen, S. B., Slater, T., Spada, G., Sutterley, T., Talpe, M., Tarasov, L., Jan Van de Berg, W., Van der Wal, W., Van Wessem, M., Vishwakarma, B. D., Wiese, D., Wilton, D., Wagner, T., Wouters, B., Wuite, J., and Team, T. I. (2019). Mass balance of the Greenland Ice Sheet from 1992 to 2018. *Nature*.

Slater, D. A., Felikson, D., Straneo, F., Goelzer, H., Little, C. M., Morlighem, M., Fettweis, X., and Nowicki, S. (2019). 21st century ocean forcing of the Greenland Ice Sheet for modeling of sea level contribution. *The Cryosphere Discussions*, 2019:1–34.

Slater, D. A., Felikson, D., Straneo, F., Goelzer, H., Little, C. M., Morlighem, M., Fettweis, X., and Nowicki, S. (2020). Twenty-first century ocean forcing of the Greenland ice sheet for modelling of sea level contribution. *The Cryosphere*, 14(3):985–1008.

Smith, R., Jones, P., Briegleb, B., Bryan, F., Danabasoglu, G., Dennis, J., Dukowicz, J., Eden, C., Fox-Kemper, B., Gent, P., Hecht, M., Jayne, S., Jochum, M., Large, W., Lindsay, K., Maltrud, M., Norton, N., Peacock, S., Vertenstein, M., and Yeager, S. (2010). The parallel ocean program (POP) reference manual: Ocean component of the community climate system model (CCSM). *LANL, Tech. Report, LAUR-10-01853*.

Smith, R. S., George, S., and Gregory, J. M. (2020). FAMOUS version xotzb (FAMOUS-ice): a GCM capable of energy- and water- conserving coupling to an ice sheet model. *Geoscientific Model Development Discussions*, 2020:1–25.

Steger, C. R., Reijmer, C. H., and van den Broeke, M. R. (2017a). The modelled liquid water balance of the Greenland Ice Sheet. *The Cryosphere*, 11(6):2507–2526.

Steger, C. R., Reijmer, C. H., van den Broeke, M. R., Wever, N., Forster, R. R., Koenig, L. S., Kuipers Munneke, P., Lehning, M., Lhermitte, S., Ligtenberg, S. R. M., Miege, C., and Noel, B. P. Y. (2017b). Firn Meltwater Retention on the Greenland Ice Sheet: A Model Comparison. *Frontiers in Earth Science*, 5:3.

Stone, E. J. and Lunt, D. J. (2013). The role of vegetation feedbacks on Greenland glaciation. *Climate Dynamics*, 40(11):2671–2686.

Straneo, F., Heimbach, P., Sergienko, O., Hamilton, G., Catania, G., Griffies, S., Hallberg, R., Jenkins, A., Joughin, I., Motyka, R., Pfeffer, W. T., Price, S. F., Rignot, E., Scambos, T., Truffer, M., and Vieli, A. (2013). Challenges to Understanding the Dynamic Response of Greenland's Marine Terminating Glaciers to Oceanic and Atmospheric Forcing. *Bulletin of the American Meteorological Society*, 94(8):1131–1144.

Sturm, M., Douglas, T., Racine, C., and Liston, G. E. (2005). Changing snow and shrub conditions affect albedo with global implications. *Journal of Geophysical Research: Biogeosciences*, 110(G1).

Sun, Q., Whitney, M. M., Bryan, F. O., and heng Tseng, Y. (2017). A box model for representing estuarine physical processes in Earth system models. *Ocean Modelling*, 112:139 – 153.

Tapley, B. D., Watkins, M. M., Flechtner, F., Reigber, C., Bettadpur, S., Rodell, M., Sasgen, I., Famiglietti, J. S., Landerer, F. W., Chambers, D. P., Reager, J. T., Gardner, A. S., Save, H., Ivins, E. R., Swenson, S. C., Boening, C., Dahle, C., Wiese, D. N., Dobslaw, H., Tamisiea, M. E., and Velicogna, I. (2019). Contributions of GRACE to understanding climate change. *Nature Climate Change*, 9(5):358–369.

Tedesco, M. and Fettweis, X. (2012). 21st century projections of surface mass balance changes for major drainage systems of the Greenland ice sheet. *Environmental Research Letters*, 7(4):045405.

Tedesco, M., Fettweis, X., Mote, T., Wahr, J., Alexander, P., Box, J. E., and Wouters, B. (2013). Evidence and analysis of 2012 Greenland records from spaceborne observations, a regional climate model and reanalysis data. *The Cryosphere*, 7(2):615–630.

Thompson, J. A. and Koenig, L. S. (2018). Vegetation phenology in Greenland and links to cryospheric change. *Annals of Glaciology*, 59(77):59–68.

Tilmes, S., MacMartin, D. G., Lenaerts, J. T. M., van Kampenhout, L., Muntjewerf, L., Xia, L., Harrison, C. S., Krumhardt, K. M., Mills, M. J., Kravitz, B., and Robock, A. (2020). Reaching 1.5 and 2.0°C global surface temperature targets using stratospheric aerosol geoengineering. *Earth System Dynamics*, 11(3):579–601.

Van de Wal, R. S. W., Boot, W., Smeets, C. J. P. P, Snellen, H., Van den Broeke, M. R., and Oerlemans, J. (2012). Twenty-one years of mass balance observations along the K-transect, West Greenland. *Earth System Science Data*, 4(1):31–35.

van de Wal, R. S. W., Zhang, X., Minobe, S., Jevrejeva, S., Riva, R. E. M., Little, C., Richter, K., and Palmer, M. D. (2019). Uncertainties in Long-Term Twenty-First Century Process-Based Coastal Sea-Level Projections. *Surveys in Geophysics*, 40(6):1655–1671.

Van Den Berg, J., Van De Wal, R., and Oerlemans, J. (2006). Effects of spatial discretization in ice-sheet modelling using the shallow-ice approximation. *Journal of Glaciology*, 52(176):89–98.

Van den Broeke, M., Smeets, P., Ettema, J., and Munneke, P. K. (2008). Surface radiation balance in the ablation zone of the west Greenland ice sheet. *Journal of Geophysical Research: Atmospheres*, 113(D13).

Van den Broeke, M. R., Enderlin, E. M., Howat, I. M., Kuipers Munneke, P, Noël, B. P. Y., Van de Berg, W. J., Van Meijgaard, E., and Wouters, B. (2016). On the recent contribution of the Greenland ice sheet to sea level change. *The Cryosphere*, 10(5):1933–1946.

van Kampenhout, L., Lenaerts, J. T. M., Lipscomb, W. H., Lhermitte, S., NoÃ«l, B., Vizcaino, M., Sacks, W. J., and van den Broeke, M. R. (2020). Present-Day Greenland Ice Sheet Climate and Surface Mass Balance in CESM2. *Journal of Geophysical Research: Earth Surface*, 125(2):e2019JF005318. e2019JF005318 10.1029/2019JF005318.

Van Kampenhout, L., Lenaerts, J. T. M., Lipscomb, W. H., Sacks, W. J., Lawrence, D. M., Slater, A. G., and Van den Broeke, M. R. (2017). Improving the Representation of Polar Snow and Firn in the Community Earth System Model. *Journal of Advances in Modeling Earth Systems*, 9(7):2583–2600.

Van Kampenhout, L., Rhoades, A. M., Herrington, A. R., Zarzycki, C. M., Lenaerts, J. T. M., Sacks, W. J., and Van den Broeke, M. R. (2019). Regional grid refinement in an Earth system model: impacts on the simulated Greenland surface mass balance. *The Cryosphere*, 13(6):1547–1564.

Van Tricht, K., Lhermitte, S., Gorodetskaya, I. V., and Van Lipzig, N. P. M. (2016). Improving satellite-retrieved surface radiative fluxes in polar regions using a smart sampling approach. *The Cryosphere*, 10(5):2379–2397.

van Vuuren, D. P., Edmonds, J., Kainuma, M., Riahi, K., Thomson, A., Hibbard, K., Hurtt, G. C., Kram, T., Krey, V., Lamarque, J.-F., Masui, T., Meinshausen, M., Nakicenovic, N., Smith, S. J., and Rose, S. K. (2011). The representative concentration pathways: an overview. *Climatic Change*, 109(1):5.

Vandecrux, B., Mottram, R., Langen, P. L., Fausto, R. S., Olesen, M., Stevens, C. M., Verjans, V., Leeson, A., Ligtenberg, S., Kuipers Munneke, P., Marchenko, S., van Pelt, W., Meyer, C. R., Simonsen, S. B., Heilig, A., Samimi, S., Marshall, S., Machguth, H., MacFerrin, M., Niwano, M., Miller, O., Voss, C. I., and Box, J. E. (2020). The firn meltwater Retention Model Intercomparison Project (RetMIP): evaluation of nine firn models at four weather station sites on the Greenland ice sheet. *The Cryosphere*, 14(11):3785–3810.

Velicogna, I., Mohajerani, Y., A, G., Landerer, F., Mouginot, J., Noel, B., Rignot, E., Sutterley, T., van den Broeke, M., van Wessem, M., and Wiese, D. (2020). Continuity of Ice Sheet Mass Loss in Greenland and Antarctica From the GRACE and GRACE Follow-On Missions. *Geophysical Research Letters*, 47(8).

Velicogna, I., Sutterley, T. C., and Van den Broeke, M. R. (2014). Regional acceleration in ice mass loss from Greenland and Antarctica using GRACE time-variable gravity data. *Geophysical Research Letters*, 41(22):8130–8137.

Vizcaino, M. (2014). Ice sheets as interactive components of Earth System Models: progress and challenges. *Wiley Interdisciplinary Reviews: Climate Change*, 5(4):557–568.

Vizcaino, M., Lipscomb, W., Sacks, W., Angelen, J. V., Wouters, B., and den Broeke, M. V. (2013). Greenland surface mass balance as simulated by the Community Earth System Model. Part I: model evaluation and 1850-2005 results. *Journal of Climate*, 26:7793–7812.

Vizcaino, M., Lipscomb, W., Sacks, W., and den Broeke, M. V. (2014). Greenland surface mass balance as simulated by the Community Earth System Model. Part II: 21st century changes. *Journal of Climate*, 27:215–226.

Vizcaino, M., Mikolajewicz, U., Gröger, M., Maier-Reimer, E., Schurgers, G., and Winguth, A. M. E. (2008).

Long-term ice sheet–climate interactions under anthropogenic greenhouse forcing simulated with a complex Earth System Model. *Climate Dynamics*, 31(6):665–690.

Vizcaino, M., Mikolajewicz, U., Ziemen, F., Rodehacke, C. B., Greve, R., and Van den Broeke, M. R. (2015). Coupled simulations of Greenland Ice Sheet and climate change up to A.D. 2300. *Geophysical Research Letters*, 42(10):3927–3935.

Wang, L., Khan, S. A., Bevis, M., van den Broeke, M. R., Kaban, M. K., Thomas, M., and Chen, C. (2019). Downscaling GRACE Predictions of the Crustal Response to the Present-Day Mass Changes in Greenland. *Journal of Geophysical Research: Solid Earth*, 124(5):5134–5152.

Weijer, W., Cheng, W., Garuba, O. A., Hu, A., and Nadiga, B. T. (2020). CMIP6 Models Predict Significant 21st Century Decline of the Atlantic Meridional Overturning Circulation. *Geophysical Research Letters*, 47(12).

Wong, G. J., Osterberg, E. C., Hawley, R. L., Courville, Z. R., Ferris, D. G., and Howley, J. A. (2015). Coast-to-interior gradient in recent northwest Greenland precipitation trends (1952–2012). *Environmental Research Letters*, 10(11):114008.

Wood, M., Rignot, E., Fenty, I., Menemenlis, D., Millan, R., Morlighem, M., Mouginot, J., and Seroussi, H. (2018). Ocean-Induced Melt Triggers Glacier Retreat in Northwest Greenland. *Geophysical Research Letters*, 45(16):8334–8342.

Zachos, J., Pagani, M., Sloan, L., Thomas, E., and Billups, K. (2001). Trends, Rhythms, and Aberrations in Global Climate 65 Ma to Present. *Science*, 292(5517):686–693.

Zeebe, R. E., Ridgwell, A., and Zachos, J. C. (2016). Anthropogenic carbon release rate unprecedented during the past 66 million years. *Nature Geoscience*, 9(4):325–329.

Ziemen, F. A., Rodehacke, C. B., and Mikolajewicz, U. (2014). Coupled ice sheet/climate modeling under glacial and pre-industrial boundary conditions. *Climate of the Past*, 10(5):1817–1836.

Acknowledgements

Ik wil graag iedereen bedanken die op de één of andere manier heeft bijgedragen om dit boekje te kunnen schrijven. Mijn vrienden en familie bedank ik voor de steun, afleiding, liefde, luisterende oren en brede schouders die ze mij steeds hebben geboden. Ik ben erg dankbaar dat jullie er voor mij zijn.

Verschillende wetenschappelijke samenwerkingen zijn belangrijk geweest in hoe dit promotieonderzoek vorm heeft gekregen. In het volgende richt ik me graag tot degenen die direct hebben bijgedragen aan de totstandkoming ervan.

Miren, I would like to express my gratitude for your guidance and your support. As my daily supervisor you have guided me in maturing as a researcher. Your energy and scientific curiosity have impressed me greatly. I have learned a lot from you in the broadest sense and I am proud to have been one of your first PhD students.

Roland, ik bedank je graag voor je betrokkenheid. Je hebt veel betekend, met name in het laatste deel van mijn PhD. Ik heb je ervaren als een empathische promotor met gevoel voor de frustraties en moeilijkheden die een promotietraject naar boven kan halen. Je heldere en pragmatische instelling is erg waardevol geweest.

Many thanks are due to the TU Delft CoupledIceClim project group in its various configurations: Raymond, Sarah, Michele, Carol, Meike, Sotiria, Miren. The variety in our research backgrounds and interests made for a group with a wide knowledge base. We have had many fruitful and sometimes loud discussions. There were exciting results to share, graphs to frown at, computational problems to tackle, and celebratory cakes to eat. The project has been crazy at times, in particular with the IPCC submission deadline. With Miren steering the wheel I think we did very well. I have greatly enjoyed working with you and I doubt I would have gotten this far without you.

For the substantial research we have done together, and the advice, input, and answers to queries you have given, I am grateful to the members of the CESM Land Ice Working Group (LIWG): Bill L., Bill S., Carol, Jan, Jeremy, Kate, Leo, Marcus, Michele, Miren, Raymond, Sarah, and others. I have very much enjoyed working with you. A special acknowledgement to Kate: I will not easily forget those weeks over Christmas when we did the production runs for the spin-up. That was madness. You were a great force then, and in the later production simulations too. Also, I would like to explicitly mention Bill L.; thank you so much for your critical reading and thorough, meticulous and elegant input on my English writing. The following phrase I have heard more than once: *Bill writes like an angel*, and I wholeheartedly agree.

The department of GRS has been a warm and welcoming workplace from my first

day onward. The PhD coffee breaks have been a source of many silly, light-hearted laughs and discussions that work so well to momentarily take your mind off your research. To the helpful and knowledgeable staff of the GRS department: Debbie, Dian, Josine, Lidwien Suzanne and the late Erwin, I am grateful for your assistance of many kinds.

Marlo, I am truly over the moon that you agreed to take on the Greenland art project for my thesis cover. The results are beautiful. Many thanks to the people that kindly shared their Greenland photographs as reference material: Benjamin, Christiaan, Maurice en Nanna.

Ik bedank graag Arjen, Jaap, Julia, Marjolein en Roderick voor het grondige lezen van de samenvattingen. Jullie opmerkingen hebben geholpen om ze aanzienlijk te verhelderen. Jaap en Liz, bedankt voor de hulp en het meedenken in de printfase. Jullie gedachten over opmaak, uitlijning en proefdrukcorrecties hebben me erg geholpen met de laatste details.

Aan hen die ik hier niet nader heb genoemd, die kennis, kunde en ervaring hebben gedeeld en me vooruit hebben geholpen de afgelopen jaren, mijn dankbaarheid is even groot.

Tot slot, aan mijn paranimfen Mariska en Roel: wat ben ik blij dat jullie vandaag naast me staan tijdens mijn verdediging.

List of Publications

First Author

Muntjewerf, L., Petrini, M., Vizcaino, M., Ernani da Silva, C., Sellevold, R., Scherrenberg, M. D. W., Thayer-Calder, K., Bradley, S. L., Lenaerts, J. T. M., Lipscomb, W. H., and Lofverstrom, M. (2020a). Greenland Ice Sheet Contribution to 21st Century Sea Level Rise as Simulated by the Coupled CESM2.1–CISM2.1. *Geophysical Research Letters*, 47(9)

Muntjewerf, L., Sellevold, R., Vizcaino, M., Ernani da Silva, C., Petrini, M., Thayer-Calder, K., Scherrenberg, M. D. W., Bradley, S. L., Fyke, J., Lipscomb, W. H., Lofverstrom, M., and Sacks, W. J. (2020b). Accelerated Greenland ice sheet mass loss under high greenhouse gas forcing as simulated by the coupled CESM2.1–CISM2.1. *Journal of Advances in Modeling Earth Systems*, 12(10)

Muntjewerf, L., Sacks, W. J., Lofverstrom, M., Fyke, J., Lipscomb, W. H., Ernani da Silva, C., Vizcaino, M., Thayer-Calder, K., Lenaerts, J. T. M., and Sellevold, R. (2021). Description and Demonstration of the Coupled Community Earth System Model v2 - Community Ice Sheet Model v2 (CESM2-CISM2). *Journal of Advances in Modeling Earth Systems*, 13(6)

Co-author

Lofverstrom, M., Fyke, J. G., Thayer-Calder, K., Muntjewerf, L., Vizcaino, M., Sacks, W. J., Lipscomb, W. H., Otto-Bliesner, B. L., and Bradley, S. L. (2020). An Efficient Ice Sheet/Earth System Model Spin-up Procedure for CESM2-CISM2: Description, Evaluation, and Broader Applicability. *Journal of Advances in Modeling Earth Systems*, 12(8)

Tilmes, S., MacMartin, D. G., Lenaerts, J. T. M., van Kampenhout, L., Muntjewerf, L., Xia, L., Harrison, C. S., Krumhardt, K. M., Mills, M. J., Kravitz, B., and Robock, A. (2020). Reaching 1.5 and 2.0°C global surface temperature targets using stratospheric aerosol geoengineering. *Earth System Dynamics*, 11(3):579–601

Curriculum Vitae

<div align="center">

L<small>AURA</small> M<small>UNTJEWERF</small>

</div>

14-12-1988	Born in Heemskerk, The Netherlands
2001–2007	**Pre-university Education (VWO)**
	Kennemer College Beverwijk, The Netherlands

2009–2012   **Bachelor of Science in Environmental Studies**
Utrecht University, The Netherlands.
Thesis: *Economic measures to reduce CO_2 emissions in the EU – taxing or cap-and-trade?*"

2013–2016   **Master of Science in Climate Studies**
Wageningen University & Research, The Netherlands.
Thesis: *Surface temperature biases in EC-Earth: attribution to vegetation and soil types of the land-surface parameterization*
Internship: *Seiches in het IJsselmeergebied: Verkennende studie WAQUA - HARMONIE*

2017–2021   **PhD. Candidate**
Delft University of Technology, The Netherlands.